Deformation microsensors on flexible substrate for health applications

Fatima Garcia-Castro

UNIVERSITE BRETAGNE LOIRE MATHSTIC

UNIVERSITÉ DE RENNES 1

THESE DE DOCTORAT DE

L'UNIVERSITE DE RENNES 1
COMUE UNIVERSITE BRETAGNE LOIRE

ECOLE DOCTORALE N° 601
Mathématiques et Sciences et Technologies de l'Information et de la Communication
Spécialité : *ELECTRONIQUE*

Par

Fatima GARCIA CASTRO

Deformation microsensors on flexible substrate for health applications

Thèse présentée et soutenue à RENNES, le 12 décembre 2019
Unité de recherche : Institut d'Electronique et Télécommunications de Rennes (IETR)

Rapporteurs avant soutenance :

Gaël GAUTIER	Professeur, Université de Tours
Claudine GEHIN	Maitre de conférences HDR, Ecole Centrale de Lyon

Composition du Jury :

Président :

Examinateurs :	Nathalie COULON	Ingénieur de recherche CNRS, IETR, Université de Rennes1
	Gaël GAUTIER	Professeur, GREMAN, Université de Tours
	Claudine GEHIN	Maitre de conférences HDR, INL, Ecole Centrale de Lyon
	Henri HAPPY	Professeur, IEMN, Université de Lille
	Claude SIMON	Maitre de conférences, IETR, Université de Rennes1
Dir. de thèse :	France LE BIHAN	Professeur, IETR, Université de Rennes1

General introduction

The new requirements of society have stimulated the electronics market, especially that of flexible electronics. This technology changes the way to use electronics, because it offers the possibility of having devices capable of adapting to any surface, being able to be bent, contorted or stretched without them ceasing to work. This makes them especially useful in different sectors such as automotive, biosensors, healthcare, mobile devices or wearable technology and increases customers interest.

Despite being widely researched, these devices still have some limitations if they are compared to rigid electronics technology.

Polymer substrates are ideal because of their properties such as lightness, low cost, flexibility, extensibility and conformability to uneven surfaces with negligible losses on sensor data. But the development of sensors on polymer substrates requires a compatible manufacturing process that respects the chemical and thermal properties of the substrates, while allowing economical manufacturing on large surfaces. The temperature range for its fabrication depends on the nature of the flexible substrate, moreover, the rigidity of traditional semiconductor materials is a limitation to their fabrication. This fact forces the industry to find alternatives to try to compensate its weakness in their manufacturing process.

New research focuses on different areas to try to improve flexibility and extensibility, such as the research and synthesis of new materials such as carbon nanotubes (CNTs) or graphene, which have a higher sensitivity, or by reducing the thickness of traditional semiconductors or by seeking a specific design that promotes their mechanical behavior. Moreover, flexible electronics can be fabricated using two different approaches top-down or bottom-up fabrication.

This thesis work is realized in the Microelectronics and Microsensors department of the Institute of Electronics and Telecommunications of Rennes (IETR) and its main goal is to investigate the piezoresistive properties of microcrystalline silicone (µc-Si) deposited by two different techniques (PECVD and ICP-CVD). This material will be used to fabricate a sensor able to react to dynamic deformations.

The technology used to perform the devices is based on the piezoresistive effect and the sensors are fabricated directly on the flexible substrate. Despite the fact that the substrate chosen is Kapton and can support relative high temperature process, around 350°C, during our fabrication

process we did not use temperatures higher than 180°C. This corresponds to the annealing process, to improve the junction between metal-semiconductor and enhance the electrical conductivity. Microcrystalline silicon is deposited at low temperature, 165°C. The reason to choose this material is that it was widely used and investigated in the laboratory, especially for applications in TFT devices. Moreover, it was also used in some works to perform static deformations on thicker plastic substrate. Hence the innovation of this thesis which uses µc-Si in pressure sensor devices to detect weak dynamic deformations; moreover, to increase their flexibility, as the thickness of the substrate used is extremely low.

The most relevant theoretical aspects, processes, problems and results obtained throughout this thesis are presented. To this end, this manuscript is structured in four chapters.

The first chapter presents a general overview of the state of the art of pressure sensors. A classification of these sensors in function of the detection range is presented, characterization parameters and applications are also described. Moreover, the basic working principle and the most popular transduction mechanisms, which are piezoresistivity, piezoelectric or capacitive effects, are described. This chapter contains also the explanation of the fabrication technology for flexible electronics with both top-down and bottom-up approaches, with a comparison between the two technologies and their main advantages and disadvantages. Finally, this chapter describes the different materials used in flexible electronics fabrication, from the substrate till the electrodes.
The choice of the appropriate substrate is one of the important factors to determine the degree of flexibility of the structure. This is one of the main limitations in the fabrication, as it will determine the maximum temperature process and, in function of its nature, the pattern design to be dedicated to stretch or strain deformations. Different flexible substrates such as metal foil, flexible thin glass or plastic substrate are presented and discussed. Another part of the structural materials is semiconductor and dielectric materials. A short description of them is done, with particular emphasis on the synthesis and study of silicon. The last point of this chapter is devoted to the metal electrodes, their shape and dimension, as this can strongly influence the mechanical behavior of the sensor.

The second chapter is dedicated to the investigation of N-type µC-Si in pressure sensor. The deposition techniques used throughout this thesis, namely PECVD (Plasma Enhanced Chemical Vapor Deposition) and ICP-CVD (Inductively-Coupled-Plasma Chemical Vapor Deposition),

are described here. The chapter presents their main characteristics as well as their operating principles, their advantages and disadvantages. Moreover, the previous works carried out in the laboratory with µc-Si on flexible substrates and the main piezoresistive properties of this material are reviewed.

During the fabrication of our devices, the thin thickness of the substrate used caused many problems. In an attempt to find a solution and better understand the mechanical behavior of thin films, some concepts are introduced to explain and describe them. Thin-film flexible devices technology fabrication is complicated not only by factors such as temperature limitation of the substrate, but also by other problems such as the sources of stress during film deposition. The mechanical behavior of substrate/film will depend on the Young's modulus and thickness of the substrate. The low thickness of our substrate has created some stress problems that induce cracks and affect the performance or our devices after µc-Si deposition. To reduce them, different approaches were investigated, and used all along the fabrication process developed during this thesis.

In chapter 3 the method of Transmission Line Measurements (TLM) for µc-Si deposited by PECVD and ICPCVD techniques is studied. This chapter can be divided in two sections. In the first section, we describe the mask used for TLM devices and the theory of this method with the interesting parameters that can be extracted. In the second section, this mask is used to make a study on the uniformity of the deposition, and also to calculate the sensitivity of µc-Si under different strain deformations.

To finalize this thesis, Chapter 4 present the study of the mechanical behavior of µc-Si under dynamic deformations. Here we describe the steps followed to create our own home-made characterization system, and we investigate the effect of the design and geometry on the sensor performance. To do that, two different masks are elaborated and the devices are submitted to different test such as continuous loading - offloading cycles.

The general conclusion brings together the main results of this thesis and presents some perspectives.

CHAPTER 1- Pressure sensors and flexible technologies

1 Introduction

Flexible electronics applications appeared around the 1950s. One objective of the solar cell research was to work on the thickness of silicon cell, which was considerably reduced until the point of being flexible. The flexible electronics field was born. Its development and applications have then grown up over until nowadays. This technology changes the way we use electronics through its ability to be bent, stretched or rolled up or be conformably shaped without working failure. For this reason, this flexible technology is a good candidate for several applications in different area such as automotive, biosensors, healthcare, mobile devices or wearable technology and increases the customer interest.

In general, flexible materials need to present some advantages, compared to the rigid electronic technology, as good bendable, twisting and stretchable properties, while keeping their high performance and characteristics, as light weighting and easy portability. Some limitations exist in the manufacturing processes and materials. Research is dedicated to the synthesis of materials, or to a specific design that contributes to their flexibility and stretchability.

As previously mentioned, many applications arise from these specific materials, especially sensors that involve bendable or stretchable properties, for example those measuring deformation or pressure. We develop flexible technology especially for this specific goal.

This chapter presents then first a general overview of the pressure sensor, describing its working principle, parameters and their different applications according to its transduction mechanism. It is then focused on the different techniques used to fabricate such devices.

2 Pressure sensor: principle and classification

A sensor is a device that is able to transform a physical or chemical stimulus into an electrical signal that can be read by an instrument. There are many types of sensors that detect different parameters such as distance, acceleration, displacement, pressure, force, humidity, movement, pH, etc. However, this section focuses on pressure sensor devices. We briefly introduce their classification, the transduction mechanism, the most relevant parameters and some applications.

2.1 Classification according to the detection range

When a sensor needs to be selected, one of the first considerations to be taken into account is the detection range. This is the working range in which the sensor is able to detect a pressure and transform it. Based on this requirement, pressure sensors can be classified into different categories, as shown in Figure 1-1.

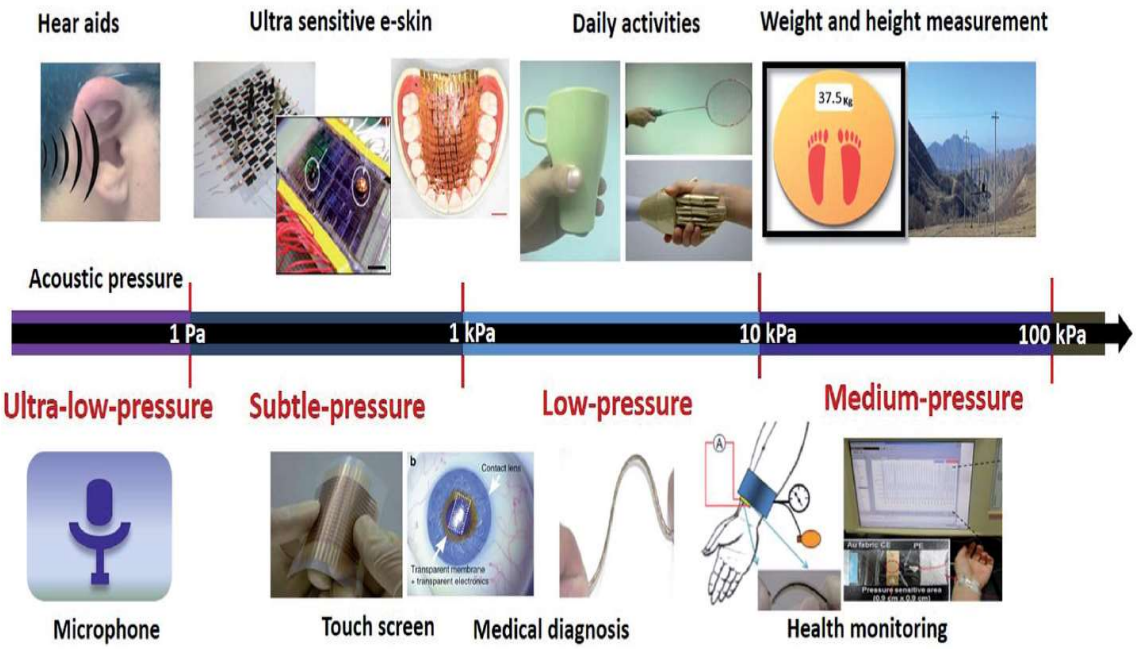

Figure 1-1. Pressure sensor classification according to the detection range and related applications [1].

Ultra-low pressures:

For a pressure range below 1 Pa, typically, the sensors are dedicated to sound pressure applications or other kinds of activities for which signals are weak and difficult to perceive, i.e. as microphones or hearing aids. Some examples of these sensors are presented in [2, 3]. Based on the piezoelectric effect, this sensor is able to detect pressure

less than 0,1 Pa [2]. Sensor using piezoresistive effect [3] can present a limit of detection of 0.8 Pa.

Subtle pressure:

For 1 Pa to1 kPa, sensors are used to develop high sensitive applications such as e-skin [4] or touchscreen devices for mobiles or tablets [5], [6] and for optical applications [7].

Low-pressure:

The pressure range between 1 to 10 kPa is widely investigated especially in daily activities or such as items application in [8], and [9]. There is also extensive research for medical diagnosis [10] or wireless or wearable epidermal sensor [11], [12].

Medium-pressure range:

Sensors in the 10 to 100 kPa range focus especially on the development of wearable blood pressure or pulse monitor application [13] or active matrix based on piezoelectric effect [14].

2.2 Parameters for pressure sensor characterization

Once the detection range of the sensor is selected, some parameters need to be considered to evaluate the performance and the accuracy of a detection device.

Limit of detection (LOD) or threshold pressure

This parameter corresponds to the lowest pressure and the maximum pressure that produce a distinguishable change in the signal. This is a relevant parameter to determine the working limits of the sensor and it help to classify it into the different regimes shown on Figure 1-1.

Linearity

This parameter expresses if the output signal can be graphically represented as approximately such a straight line. This is important to obtain more accurate and reliable sensors. Moreover, a good linearity helps for the post-treatment signal. Typically, strain sensors based on the piezoresistive effect exhibit good linearity when they are submitted

to low strain. However, for high deformation levels, the response is not always linear due to the significant change in morphology during stretching which can generate cracks in the structure. [12], [15].

Response time, recovery time and hysteresis

These characteristics are defined together because there is a relationship between them and they are all relevant for dynamic and real-time applications.
Hysteresis can be defined as the ability of the sensor to obtain the same output signal when, under the same conditions, it is submitted to loading-unloading cycle.
The recovery time is defined as the time that the sensor needs to come back to its electrical characteristics when the load is removed.
The response time shows the time the sensor needs to respond to the next input step. All have a relationship with the viscoelastic property of the active material and the contact conditions between the material and the electrodes. [3]

Sensitivity or Gauge factor

During the characterization of our devices, this is one of the parameters that need to be further explored. In chapter 3, it is explained in more details. But we can summarize in few words that the gauge factor is the slope of the relative change of a resistance or a capacitance versus the deformation stress applied.

2.3 Transduction mechanism and application

A pressure sensor is based on different physical mechanisms that can convert the physical deformation or stimulus into an electrical signal. The most commonly used effects are piezoresistivity, capacitance changes, and piezoelectricity. Each different mechanism is presented below and its main principle is described.

2.3.1 Piezoresistivity

This method is based on the variation of the electrical resistance of a semiconductor or a metal when a mechanical strain is applied. Sensors based on this phenomenon have usually simple structure and working principle, and have been widely studied. Moreover they are suitable to be used in a large range of pressures or deformations.

The effect can be explained with the follow equations. First of all, the resistance is expressed by the following equation:

$$R=\rho\frac{L}{S} \tag{1-1}$$

With ρthe resistivity of the material L, the length and S the section of the resistance. As shown in Figure 1-2, when a strain is applied a variation in the structure is produced and consequently, a change in the resistance.

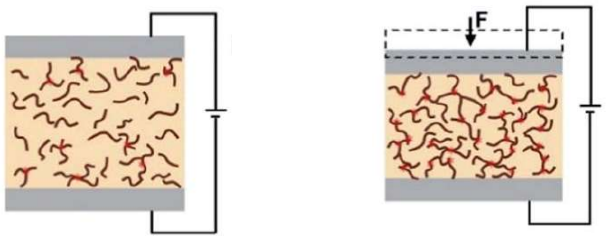

Figure 1-2. Schematic of piezoresistive effect.

The gauge factor (GF), defined in equation (2), is used to express the sensibility of the material to the deformation ε. All the theoretical aspects of this effect will be explained deeper in Chapter 2 and the electrical measurements in Chapter 3. The gauge factor is expressed as:

$$GF = \frac{\frac{\Delta R}{R}}{\varepsilon} \tag{1-2}$$

First gauges used to measure the pressure consists on metal foil on a flexible substrate. The pressure induces strain and a chance in the resistance value is observed. This change depends on the metal line geometry. The typical gauge factor obtained in this case vary between 2 and 5, [16]. However, due to this quite low value of the gauge factor, research has begun on materials with higher values. In 1960, the first high -performance silicon devices appeared. The devices, fabricated with n-doped silicon, present a GF near 135, and reach 170 if silicon is p type [16]. The theory of how doping silicon affects the gauge factor will be explained in Chapter 2.

Because of their simple structure and low cost, there are several examples in the literature of applications using this principle. One example is presented by R. Ramalingame [17].

A highly flexible matrix based on a carbon nanotube (CNT) polymer composite is processed on a Kapton substrate and linked to an acquisition system. Haniff [18] proposed a flexible pressure sensor also based on piezoresistive effect made with graphene deposited though hot- filament thermal chemical vapour deposition (HFTCVD) at different temperatures. .

In the piezoresistive effect, the change occurs only in the electrical resistance, while the variation of the electrical potential is due to the piezoelectric effect, described below.

2.3.2 Piezoelectric effect

It refers to the electrical change produced in particular materials as crystals or ceramics. When those materials are submitted to mechanical stress, an electric polarization occurs on their volume ~~and~~ as shown in Figure 1-3. Then electrical charges and a difference of potential appear.

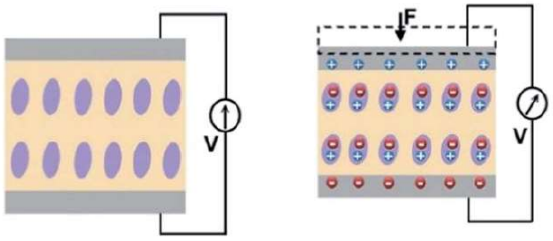

Figure 1-3. Schematic of piezoelectric effect.

This kind of sensor is widely used in dynamic applications, especially because it shows good performances as high sensitivity, fast time response, easy electrical signal acquisition, easy material preparation, and low power consumption or even self-power [19], [20]. In the past, traditional piezoelectric materials were ceramics and quartz. They have been replaced by new materials, more robust, such as poly-vinylidene fluoride-trifluoroethylene (P(VDF-TrFE), barium titanate ($BaTiO_3$), lead zirconate-titanate (PZT), and zinc oxide (ZnO).

Between all of them, the most popular is P(VDF-TrFE) due to simple manufacturing and high piezoelectric coefficient.

Chunyan [21] has developed a tactile sensor using dome and bump shapes of PVDF-TrFE films over a polymer substrate. Using a new fabrication method provides a flexible

way to pattern the polymer with different shapes and dimensions. The sensor developed in this paper can be used in minimally invasive biomedical devices.

C. Chang [22] has also developed devices with this piezoelectric material that provide a high-performance and a fast response for wearable applications. To do that, using the electrospinning method, P(VDF-TrFE) nanofibers are directly written on a grounded substrate as shown in Figure 1-4. Under mechanical stretching, it shows repeatable and consistent electrical outputs with efficient energy conversion.

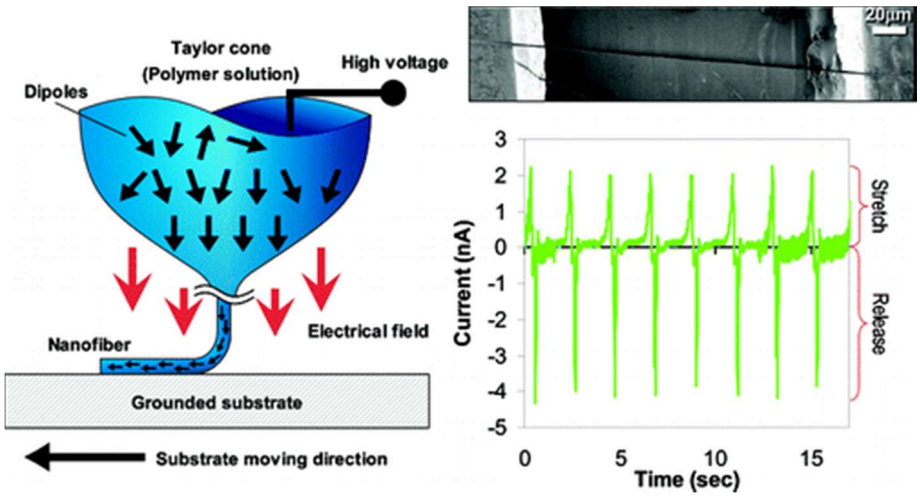

Figure 1-4. P(VDF-TrFE) nanofibers deposited by electroshock and output characteristics under stretch and release [22].

2.3.3 Capacitance

Capacitance devices can be formed by two metallic electrodes around a dielectric material. The capacitance value (C) is given by the equation (3) where ε_0 and ε_r are the vacuum permittivity and the relative static permittivity of the material between the electrodes, A is the surface between the electrodes and d, the distance between them. The value of the capacitance is inversely proportional to the distance between the electrodes and proportional to the dielectric contact and the area.

$$C = \frac{\varepsilon_0 \varepsilon_r A}{d} \tag{1-3}$$

As shown in Figure 1-5, when a deformation is applied, the distance between the two electrodes (d) and the area (A) are modified. So the value of the capacitance changes.

When an external force is applied, it can change: *i)* the displacement of elastic materials due to the shear force, then the area A changes, *ii)* forward force that change the distance d, *iii)* or torsion that change the two parameters A and d.

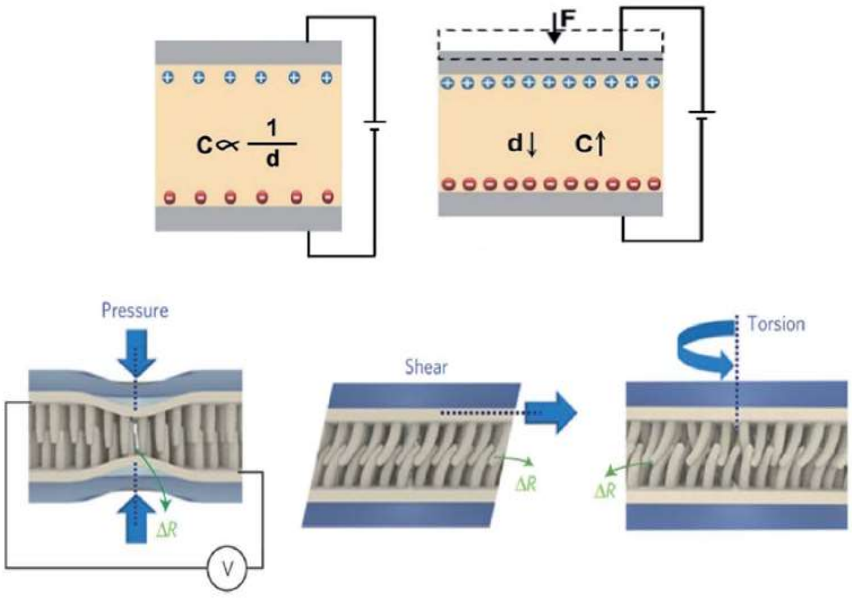

Figure 1-5. Schematic of capacitive effect.

There are several fields where this technology is commonly used, for example in the robotic market where, in 1997, a fingerprint array with capacitive sensitive cells on silicon was proposed. However, this sensor present a low resolution and could only measure the normal force [23]. Technological improvement were achieved with capacitive sensors over polymer. Those are able to measure normal and shear forces [24]. High sensitive capacitance sensors able to analyze the direction and value of three dimensional (3D) forces are mentioned by Huang [25], Dobrzynska [26] or Surapaneni [27].

2.3.4 Other transduction methods

Other methods exist for pressure sensor applications, but are not so widely used. This is the case of the optical methods, based on the measurement of the light intensity variation. They can be used for touch screen applications like smartphones or tablets. The inductive effect is another transduction method that measures the variation of an inductance between two magnetic fields or resonant sensors generally dedicated to acoustic applications.

Table 1-1 sums up the advantages and disadvantages of the three main transduction methods.

Type	Advantage	Disadvantage
Piezoresistive	Low cost Good sensitivity Low noise Simple electronics	Stiff and frail Nonlinear response Hysteresis Temperature sensitive Signal drift
Capacitive	Sensitive Low cost Availability commercial A/D chips	Cross-talk Hysteresis Complex electronics
Piezoelectric	Dynamic response High bandwidth	Temperature sensitive Not so robust electrical connection

Table 1-1. Comparative of transduction methods for pressure sensor [28].

3 Techniques to perform flexible devices

The continuous evolution and improvement of thin-film materials and devices have impulse the development of flexible electronics. Their fabrication is one of the great challenges of this technology, and their manufacturing processes have been deeply studied [29], [30] leading to a wide variety of applications in different fields such as displays, storage devices, or wearable devices for medical area.

Despite of the growing research on flexible electronics, this technique needs to be improved to present good electrical and mechanical properties, in any case lower than those obtained with traditional electronics manufactured made of rigid and planar semiconductor wafers.

Currently, the electronic structure of flexible devices is formed by a substrate, a semiconductor material and the electrodes. It should present good performances after ~~be~~ bending, stretching, twisting or deformation into complex shapes. The entire structure should be created with a compromise between the design, the thickness of the materials and their mechanical properties. One of the main drawbacks during flexible devices fabrication is that the required substrates present a temperature limitation that involves

the industrial development of new methods of processing. Nowadays, there are mainly two different strategies to fabricate devices on a plastic substrate, as further described.

3.1 Top-down fabrication

Some deposition processes require high temperatures, which are not compatible with some flexible substrates that could be damaged or deformed [31]. This is why some manufacturing companies use the top-down approach to perform flexible devices.

This method has the advantage that the whole structure is done by a standard fabrication process on a rigid substrate (generally glass plate or Si wafer) which allows the use of conventional photolithographic processes [32], [33] and has no temperature limitation for deposition layers. Once the structure is completed, it is transferred to a flexible plastic substrate though various methods such as the transfer-printing process or the release of the rigid substrate [34]. Thus, with this technique, it is possible to fabricate devices at high temperature providing high performance devices on flexible substrate, but the major drawbacks are the high cost, the small surface coverage (only for low dimension structures) and the use of expensive and specific equipment. These transfer and bond techniques could be performed by different methods and two examples of these are shown next.

Figure 1-6 [35] shows the different steps of a fabrication process, which consists in spin-coating Cytop (amorphous fluoropolymer) film onto patterned Si wafer to design a mold. Then, a graphene ink is deposited. After annealing, the structure is ready to be transferred onto a flexible polyethylene terephthalate (PET) substrate. To do this, a liquid Optical Adhesive is used between graphene and PET. The backside of the PET substrate is treated by O_2 plasma generating the peeled-off from the Cytop/Si mold by the UV-cured NOA73 adhesive layer.

Figure 1-7 is based on the EPLAR (Electronics on Plastic by Laser Release) technique developed by Philips Research. It consists of spinning and curing a layer of polyimide (PI) on top of a glass substrate using a sacrificial layer in between. At the end of the process, the polyimide layer is separated from the rigid substrate by removing the sacrificial layer by pulses of an excimer laser in the backside of the sample, causing its delaminating. [36]

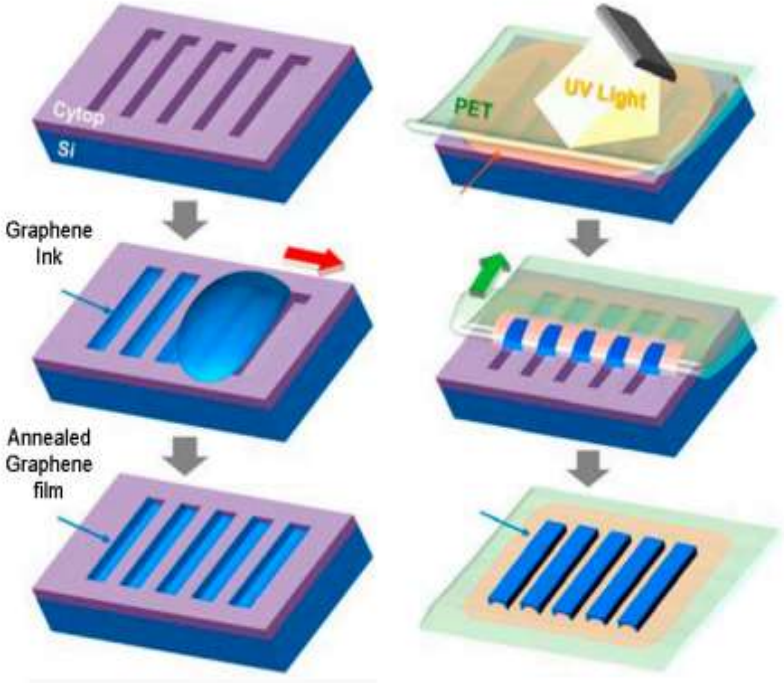

Figure 1-6. : Example of top-down techniques [35].

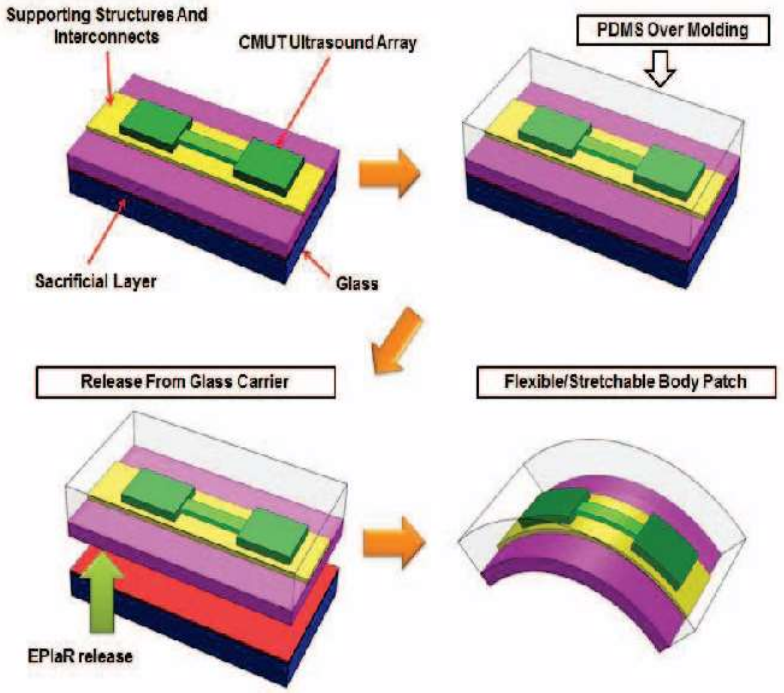

Figure 1-7 : EPLAR technique illustration [36].

This technique allows to add the substrate at the end of the fabrication process. It is then possible to use bio organic substrates. This makes it a great option to fabricate devices

that are compatible with biomedical applications. KJ. Yu [37] explains that by depositing the final structure on bio-resorbable poly-(lactic-co-glycolic) acid, the technology becomes compatible with applications on the skin.

3.2 Bottom-up fabrication

This technique is the most common because direct fabrication on flexible substrates reduces the price. However, the main disadvantage is that, depending on the plastic substrate selected, a specific process at low temperature will be required.

During the deposition steps, reducing the temperature affects the electrical and mechanical performance of the device. For this reason, in order to achieve a good quality sensor, research focused on bottom-up techniques deals with new materials such as carbon or graphene, or with the development of new growth methods. Figure 1-8 shows an example of a bottom-up fabrication technique [38]. It illustrates the fabrication process of a tactile sensor using PDMS as a substrate. To do this, it is first necessary to pattern some microstructures on silicon which will be used as a mold to fabricate PDMS. A rGo (reduced graphene oxide) film is then deposited on this PDMS mold and coated with ITO/PET.

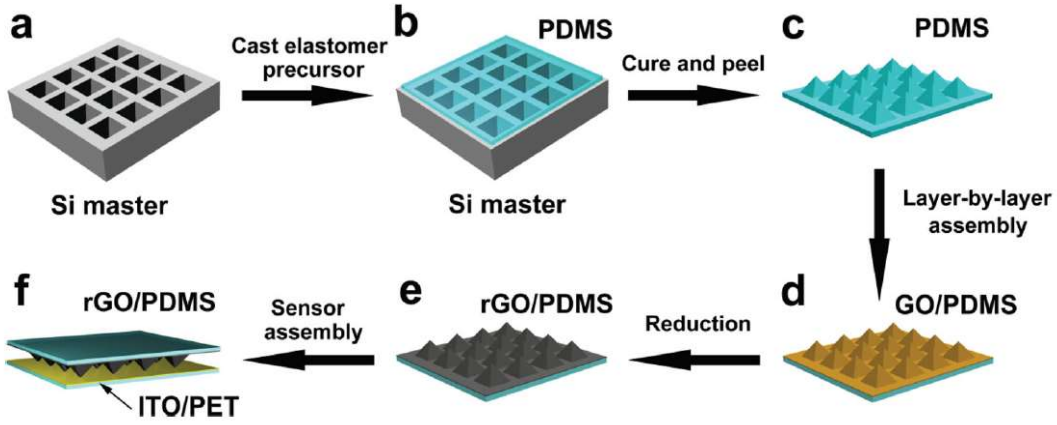

Figure 1-8. Schematic illustration of the tactile sensor device fabrication by using bottom-up approach.

In our case, we decided to fabricate our devices on the basis of bottom-up technique, because it is the historical technique of the laboratory, [39] and the required equipment are available in the laboratory. It was also a good option due to the approach to the manufacturing large area surfaces and the low cost.

In the following sections, we will present the different kind of materials than can be used in flexible electronic devices depending on the application. It is important to select the adequate material, to explain the properties that the substrate, the semiconductor materials and the electrodes must have.

4 Substrates

The main limitations of traditional rigid electronics are intrinsic rigidity, fragility and inability to interface with curvilinear morphological surfaces. Flexible electronic substrates offer a solution to these limitations, but their handling is more delicate, given their sensitivity to cracking and delamination due to the limited failure stress during bending deformation. These problems are discussed in detail in Chapter 2.

Depending of on the nature of the application, there are different kinds of substrates may be used in flexible device applications. Figure 1-9 shows the degree of flexibility or mechanical properties that can be classified into the following categories: i) these devices can be deformed in tension or compression, permanently deformed. ii) These materials are not able to return to their original state, which makes their deformation and elasticity permanent.. iii) These materials have the ability to be deformed in the vertical plane.

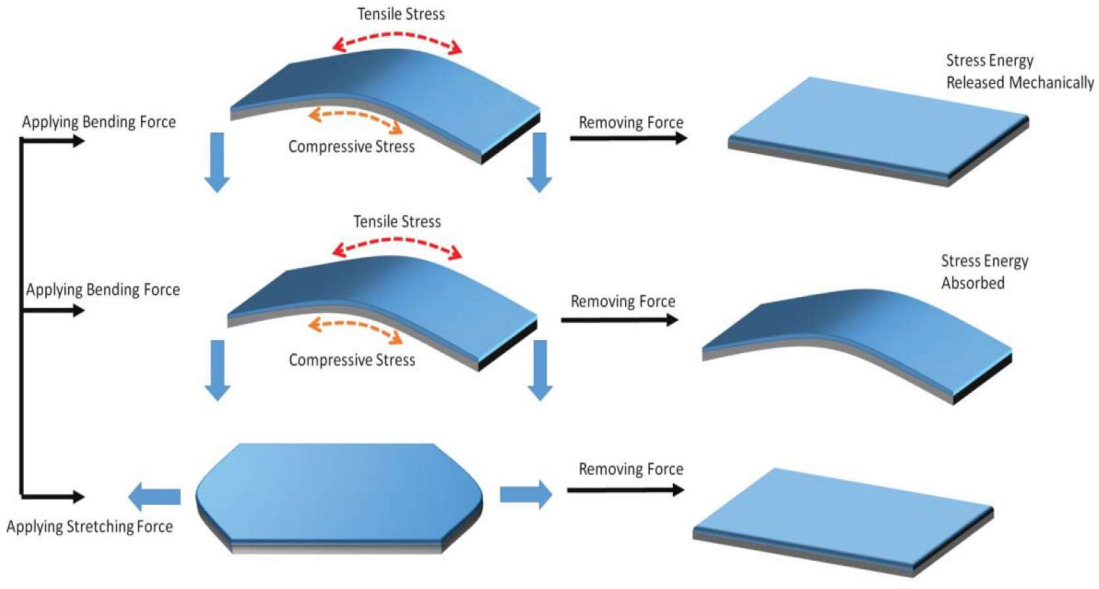

Figure 1-9. Flexibility degree of substrates.

The choice of the appropriate substrate will define the behavior of the compound structure. For this reason, in addition to the degree of flexibility, there are other

requirements and properties that are important to consider when selecting this layer; some of them will be explained below.

Optical properties: According to the application, this optical parameter could be extremely relevant. For example, LCDs must have low birefringence and some displays require an optically clear substrate.

Roughness: For thin film devices, electrical properties have a direct link with the surface roughness. For this reason, for a short length, this parameter should be avoided, but for long length, a low value might be acceptable.

Thermal and thermomechanical properties: The substrate should be compatible with the temperature during the fabrication process. The main important parameters are:

- The compatibility between the maximum temperature of the fabrication process (Tmax) and the transition temperature (T_g) of the substrate. A mismatch between these two parameters could create some cracks in the device's films.
- The coefficient of thermal expansion, CTE, is defined as the dimensional deformation of the substrate during the temperature process. This is defined in the equation 4 where ε represents the deformation of the material and ΔT represents the variation between the initial temperature of the substrate and the process at high (or low) temperature. Depending on this, the substrate undergoes compression ($\Delta T < 0$) or expansion ($\Delta T > 0$).

$$\varepsilon = \Delta(\text{CTE})(\text{substrate-film}).\ \Delta T(\text{deposition-ambient}) \quad (1\text{-}4)$$

The variation of the CTE produces thermal mismatch between substrate/film and therefore some cracks; this will be discussed in more detail in Chapter 2.

Chemical properties: The substrate should be compatible with chemistry products used during the fabrication process, such as acetone or acids or other corrosive chemicals [40].

Mechanical properties: This is given mainly for the degree of flexibility and should present a compromise between elastic modulus or Young's modulus (GF) of each material, the structure and thickness of the compound of each layer and the design.

Generally, there are three types of substrate material, presented below, for flexible applications.

4.1. Metal foil of stainless steel

It is one of the most used due to its resistance to chemical processes, its high temperature range, up to 1000°C, its dimensional stability and its long durability. However, it presents a high surface roughness (approximately 100 nm) compared with glass or some plastic substrates (less than 1nm). For this reason, in order to have good electrical behavior, the surface of these steel foil substrates should be pre-treated with a polished or planearized film.

4.2. Thin flexible glass

Glass becomes flexible when its thickness is less than 100 μm but the biggest drawback is the fragility and the handling.

4.3. Plastic substrates

These types of substrates offer great flexibility, low cost and the possibility of being on a roll. However, their dimensional stability is lower than glass. To find more stable dimensions, they should be submitted to a large annealing. Flexible plastic substrates include semicrystalline polymers, noncrystalline polymers and high T_g materials like polyimide (PI). For our application, metal foil and glass were not a good option due to the high rigidity and low degree of flexibility. The most used plastic substrates for developing flexible electronic components are polyesters such as PEN (polyethylene naphthalene), PET (polyethylene terephthalate) and PI (polyimide) due to relatively high elastic moduli and their good resistance to chemicals. The substrates of PEN and PET are characterized by a high level of transparence, more than 80%, and a low roughness surface (datasheet on appendix 1). However, the maximum temperature process is up to around 200°C for PEN [see datasheet on appendix 1] and around 150°C for PET [see datasheet on appendix 1]. On the other hand, the temperature range for some PI such as Kapton can goes up to around 350°C (see table 1-2, that shows a summary of the different kind of plastic substrates). For plastic substrates, it is important to control the maximum process temperature and not to exceed the glass transition temperature, which would involve substrate deformation. An example of that is shown in Figure 1-10 [31]. PET has been submitted to different thermal treatments to the point of complete destruction.

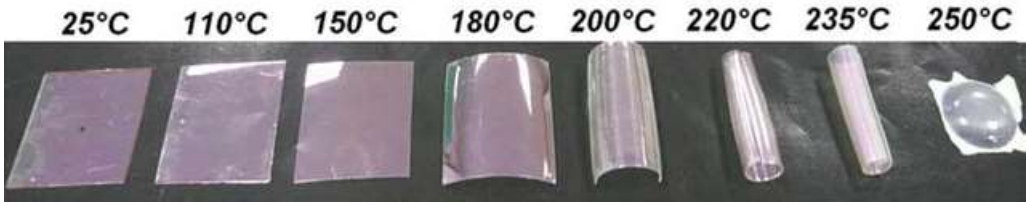

Figure 1-10. PET/ITO substrates deformation after thermal treatment [31].

Max. Dep. Temp. (°C)	Material	Properties
250	Polyimide (Kapton)	Orange color, high thermal expansion coefficient, good chemical resistance, expensive, high moisture absorption
240	Polyetheretherktone (PEEK)	Amber, good chemical resistance, expensive, low moisture absorption
190	Polyethersulphone (PES)	Clear, good dimensional stability, poor solvent resistance, expensive, moderate moisture absorption
180	Polyetherimide (PEI)	Strong, brittle, hazy color, expensive
160	Polyethylene Naphthalate (PEN)	Clear, moderate CTE, good chemical resistance, inexpensive, moderate moisture absorption
120	Polyethylene terephthalate (PET)	Clear, moderate CTE, good chemical resistance, inexpensive, moderate moisture absorption

Table 1-2: Properties of main plastic substrates.

5 Semiconductor and dielectric materials

One of the greatest challenges in flexible electronics is obtaining high performance semiconductor and dielectric materials.
We present below the two types of organic and inorganic semiconductors.

5.1 Organic semiconductor in flexible electronics

Organic semiconductors are attractive because they can be processed at low or at room temperature and they have a good mechanical flexibility. However, these materials have some disadvantages like poor crystallinity, low mobility, and possible degradation in the air which requires encapsulation with an thin inorganic film [41].

Generally, the price of these materials and their fabrication process is higher compare to inorganic semiconductors. Moreover, there are some organic semiconductors such as pentacene that require a special preparation procedure due to their high sensitivity to e contamination [42]. The most popular process to fabricate organics electronic are the followings:

Spin coating consists in spreading the semiconductor material by centrifugal force on the substrate when this rotates at high speed. With this technique, it is complicated to control the thickness and the uniformity of the material.

Thermal evaporation, the organic semiconductor is evaporated under vacuum. Generally, a shadow mask is used to define the structure, as this avoids the photolithography step, knowing that many organic semiconductors are sensitive to solvents [43].

Inkjet printing consists of printing the organic solution. This could be done by different techniques such as serigraphy, flexography or roll to roll technique [44].

Organic materials have some disadvantages when compared to inorganic semiconductors, such as free carrier mobility which is several orders of magnitude lower [40].
For industry, the need for low-cost manufacturing processes for large-scale flexible electronics and the low deposit uniformity for large substrate surfaces make inorganic technology the most popular technology on the electronics market.
Nevertheless, organic semiconductors have significant advantages, they have good intrinsic flexibility, making them a good choice to fabricate flexible electronic devices. Moreover, this technology has a promising future especially in fields such as healthcare, biosensors or wearable applications that need to be compatible with the body.

5.2 Inorganic semiconductor flexible electronics

Traditional electronic products are developed with this kind of semiconductor because of their excellent physical and chemical properties such as high electrical and thermal conductivity. Silicon is one of the most widely used products in the semiconductor

industry. Some generalities of silicon and its use in flexible electronic technology will be presented.

Advances in flexible electronic technology have required the study of other inorganic nanomaterials such as Graphene Oxide (GO) [45], [46] or GaAS [47] with the goal of decreasing the rigidity and fragility of inorganic materials. Another alternative is to increase their flexibility, for example by reducing their thickness.

Silicon technology is one of the most developed technologies on the market. In the laboratory, we chose silicon as the main material for the implementation of our sensors. Silicon can exist in many allotropic forms (Fig. 1-11). Its conductivity depends on the elaboration parameters such as gas dilution, pressure, deposition temperature, layer thickness, doping levels and doping materials... All these conditions will also determine the quality of the material, the resistance of contact between the different layers and therefore the performance of devices.

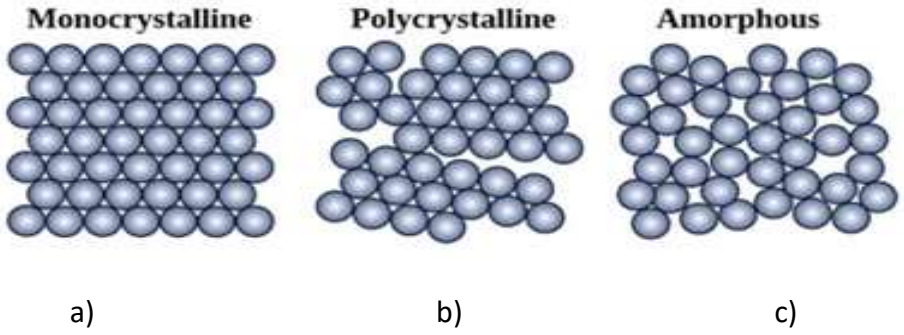

Figure 1-11. Allotropic states of silicon.

Single crystalline silicon (sc-Si) also called monocrystalline silicon:

It presents a "diamond" crystalline lattice as shown in Figure 1-11 (a). The temperature required for the growth is higher than 900°C, which is very high for flexible substrates; only few of them can support this range in the form of flexible stainless steel foil. Moreover, because of this uniform structure the behavior of the crystal is a bad option for using it in the high deformation measurement. However, silicon in this state is widely used in industry in the form of wafers whose dimensions can vary.

Amorphous Silicon (a-Si):

The atomic structure of amorphous silicon (Fig. 1-11 c) is characterized by the fact that it does not present a crystalline structure or order, making it a good candidate for flexible

electronic [48]. Generally, it is deposited at a temperature lower than 250°C [49] making it compatible with a large number of flexible substrates such as PEN, Kapton or biodegradable substrates. Thanks to its lattice, it presents good flexibility but a lot of electrical instability and poor performance.

Polycrystalline, microcrystalline and nanocrystalline silicon:

It is a particular form of silicon. This is an intermediate state between amorphous and single crystalline silicon. Figure 1-11 (b) presents well-ordered zones of crystalline grains and non-crystallized (amorphous) zones. Depending on the grain size, it can be known as microcrystalline silicon (µc-Si) if the grain size is between 1 nm and 1 µm or nanocrystalline (nc-Si) when the grain size is less than 10 nm. Figure 1-12 shows the classification of silicon according to the grain size and the temperature deposition range. The approximate grain size of µc-Si, 70 nm, is obtained in the IETR.

Compared to amorphous silicon, it offers a better stability [50], and a higher mobility [51]. It is widely used in thin film transistor fabrication [52] [53]. There are different techniques to deposit this material, such as sputtering or different chemical vapor deposition (CVD) techniques. The deposition techniques used in the IETR will be widely described in Chapter 2.

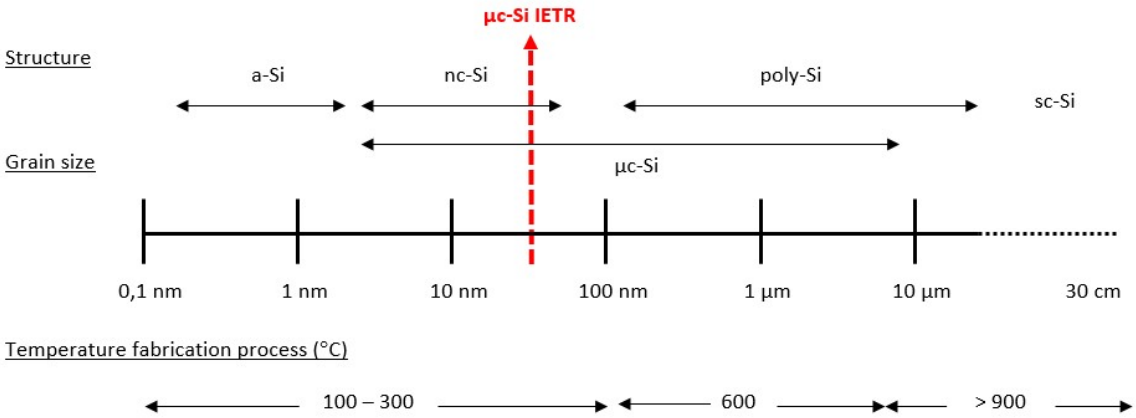

Figure 1-12. Classification of silicon as a function of the grain size and the temperature deposition range.

5 Metal electrodes

When flexible devices are submitted to bending or stretching deformation, all the layers of the sensor undergo this effect, so for flexible sensing devices, mechanical flexibility and stability of the electrodes must be taken into account.

Thick metals cannot be used for these applications, however ultra-thin metals can support bending conditions without easily breaking. This is due to the bending strain which decreases proportionally with thickness. In addition to thickness reduction, to reduce fractures, it is necessary to have a good design such as wavy structures, serpentine patterns, coiled springs [54] [55].

Conventional fabrication of metal electrodes in the laboratory consists in evaporation deposition, that it is the same technology used on hard substrates such as silicon wafers, but this can damage the soft substrate due to the use of strong solvents, high temperatures or high pressures [56]. There are other alternatives such as solution-based wet chemical methods, including printing and plating techniques which allow rapid, low temperature and cost effective fabrication.

There are some considerations for a good flexible electrode, such as its high electrical conductivity, its good adhesion and its great robustness against mechanical deformations. The most commonly used metal for electrode fabrication include gold (Au), silver (Ag), copper (Cu) and nickel (Ni), but for flexible applications some materials such as grapheme, carbon nanotubes (CNTs) or metal nanowire (NWs) are widely used because of their high conductivity and flexibility.

However, taking into account the cost/conductivity [57], silver is a good option for our devices. The performance of the electrodes can be evaluated by measuring the electrical conductivity though the contact resistivity between the metal and the semiconductor. This is deeply explained in chapter 3, as the measurements in our devices via the TLM device.

In addition to the electrical characterization, it is necessary to quantify the mechanical flexibility and robustness by performing the “bending test” as mentioned in the literature [58] [59]. As shown in Figure 1-13, the electrode is repeatedly bent into a curvature shape and the change of the bulk resistance is measured during the cycles.

Figure 1-13: Bending test on metallic electrodes.

6 Conclusion

This chapter allows us to present a general overview of the state of the art of pressure sensors. Characterization parameters, working principle and main applications in the electronic market were described. Moreover, the different methods used to fabricate flexible electronics, top-down or bottom-up were discussed.

In order to optimize the mechanical performance of flexible electronics, all the layers of the global structure should be chosen in function of the application of the device. Hence, a comparison was done between the different materials that form the sensor's structure such as the substrate choice, because this will determine the degree of flexibility of the structure, the semiconductor and dielectric materials, and the effect of metal electrodes in the electrical and mechanical performance. The synthesis and study of the properties of silicon, material used in our devices are also presented.

All these general information will help us to better understand the considerations that should be taken into account to fabricate flexible devices. In the next chapter, all of these will be used in our devices.

References

[1] Y. Zang, F. Zhang, C. Di, and D. Zhu, 'Advances of flexible pressure sensors toward artificial intelligence and health care applications', Mater. Horiz, vol. 2, no. 2, pp. 140–156, Feb. 2015.

[2] L. Persano, C. Dagdeviren, Y. Su, Y. Zhang, S. Girardo, D. Pisignano, Y. Huang and J. A. Rogers 'High performance piezoelectric devices based on aligned arrays of nanofibers of poly(vinylidenefluoride-co-trifluoroethylene', | Nature Communications, . [Online]. Available: https://www.nature.com/articles/ncomms2639. [Accessed: 25-Aug-2019], March 2013

[3] L. Pan, A. Chortos, G. Yu, Y. Wang, S. Isaacson, R. Allen, Y. Shi, R. Dauskardt and Z. Bao, 'An ultra-sensitive resistive pressure sensor based on hollow-sphere microstructure induced elasticity in conducting polymer film', Nature Communications., vol. 5, p. 3002, 2014.

[4] N. Lu, C. Lu, S. Yang and John Rogers, 'Highly Sensitive Skin-Mountable Strain Gauges Based Entirely on Elastomers', Advanced Functional Materials, vol. 22,pp. 4044-4050, 2012

[Online]. Available: https://onlinelibrary.wiley.com/doi/abs/10.1002/adfm.201200498. [Accessed: 25-Aug-2019].

[5] C. Pang, G-Y. Lee, T-I. Kim, S.M. Kim, H.N. Kim, S-H. Ahn and K-Y. Suh, 'A flexible and highly sensitive strain-gauge sensor using reversible interlocking of nanofibres', Nature Materials, vol. 11, pp 795-801, 2012, [Online]. Available: https://www.nature.com/articles/nmat3380. [Accessed: 25-Aug-2019].

[6] M. Kaltenbrunner et al., 'An ultra-lightweight design for imperceptible plastic electronics', Nature, vol. 499, no. 7459, pp. 458–463, Jul. 2013.

[7] M. Ramuz, B. C-K. Tee, J. B.-H. To and Z. Bao, 'Transparent, Optical, Pressure-Sensitive Artificial Skin for Large-Area Stretchable Electronics' Advanced Materials, vol. 24, no 24, pp. 3223-3227, 2012, [Online]. Available: https://onlinelibrary.wiley.com/doi/abs/10.1002/adma.201200523. [Accessed: 25-Aug-2019].

[8] T. Sekitani and T. Someya, 'Stretchable, Large-area Organic Electronics', Advanced Materials, vol. 22, no. 20, pp. 2228–2246, 2010.

[9] G.A. Salvatore, N. Münzenrieder, T. Kinkelde, L. Petti, C. Zysset, I. Strebel, L. Büthe and G. Tröster, 'Wafer-scale design of lightweight and transparent electronics that wraps around hairs', Nature Communications, vol. 5, no 2982, 2014, [Online]. Available: https://www.nature.com/articles/ncomms3982. [Accessed: 25-Aug-2019].

[10] X. Wu, Y. Han, X. Zhang, Z. Zhou and C. Lu, 'Large-Area Compliant, Low-Cost, and Versatile Pressure-Sensing Platform Based on Microcrack-Designed Carbon Black@Polyurethane Sponge for Human–Machine Interfacing'., Advanced Functional Materials, vol.26, no34, pp. 6246-6256, 2016, [Online]. Available: https://onlinelibrary.wiley.com/doi/abs/10.1002/adfm.201601995. [Accessed: 25-Aug-2019].

[11] X. Huang, Y. Liu, H. Cheng, W.-J. Shin, J.A. Fan, Z. Liu, C.J. Lu, G.W. Kong, K. Chen, D.Patnaik, S.H. Lee, S.Hage-Ali, Y. Huang and J.A. Rogers, 'Materials and Designs for Wireless Epidermal Sensors of Hydration and Strain', Adv. Funct. Mater., vol. 24, no. 25, pp. 3846–3854, 2014.

[12] S. Gong, D.T.H. Lai, B. Su, K.J. Si, Z. Ma, L.W. yap, P. Guo and W. Cheng, 'Highly Stretchy Black Gold E-Skin Nanopatches as Highly Sensitive Wearable Biomedical Sensors', Adv. Electron. Mater., vol. 1, no. 4, pp. 1400063, 2015.

[13] C.L. Choong, M.B. Shim, B.S. Lee, S. Jeon, D.S. Ko, T.H. Kang, J. Bae, S.H. Lee,K.E. Byun, J. Im, Y. Jin Jeong, C.E. Park, J.J. Park and U.I. Chung, 'Highly Stretchable Resistive Pressure Sensors Using a Conductive Elastomeric Composite on a Micropyramid Array', Adv. Mater., vol. 26, no. 21, pp. 3451–3458, 2014.

[14] I. Graz, M. Krause, S. Bauer-Gogonea, S. Bauer, S.P. Lacour, B. Ploss, M. Zirki, B. Stadlober and S. Wagner, 'Flexible active-matrix cells with selectively poled bifunctional polymer-ceramic nanocomposite for pressure and temperature sensing skin', J. Appl. Phys., vol. 106, no. 3, pp. 034503, 2009.

[15] S. Wu, R.B. Ladani, J. Zhang, K. Ghorbani, X. Zhang, A.P. Mouritz, A.J. Kinloch and C.H. Wang, 'Strain Sensors with Adjustable Sensitivity by Tailoring the Microstructure of Graphene Aerogel/PDMS Nanocomposites', ACS Appl. Mater. Interfaces, vol. 8, no. 37, pp. 24853–24861, 2016.

[16] S. Middelhoek and S. A. Audet, 'Silicon Sensors', published by Academic Press, Ltd, London, 376 pp. 1989, [Online]. Available: https://infoscience.epfl.ch/record/24206. [Accessed: 25-Aug-2019].

[17] R. Ramalingame, Z. Hu, C. Grelach, D. Rajendran, T. Zubkova, R. Baumann and O. Kanoun, 'Flexible piezoresistive sensor matrix based on a carbon nanotube PDMS

composite for dynamic pressure distribution measurement', J. Sens. Sens. Syst., vol. 8, no. 1, pp. 1–7, 2019.

[18] M. A. S. Mohammad Haniff, S.M. Hafiz, K.A.A. Wahid, Z. Endut, H.W. Lee, D.C.S.Bien, I.A. Azid, M.Z. Abdullah, N.M. Huang and S.A. Rahman, 'Piezoresistive effects in controllable defective HFTCVD graphene-based flexible pressure sensor', Nature, Sci. Rep., vol. 5, p. 14751, 2015.

[19] S. Xu, Y. Qin, C. Xu, Y. Wei, R. Yang and Z.L. Wang, 'Self-powered nanowire devices', Nature Nanotechnology, vol.5, pp. 366-373, 2010, [Online]. Available: https://www.nature.com/articles/nnano.2010.46. [Accessed: 25-Aug-2019].

[20] G. Zhu, Q. Yang, T. Zhang, Q. Jing, J. Chen, Y.S. Zhou, P. Bai and Z.L. Wang, 'Self-Powered, Ultrasensitive, Flexible Tactile Sensors Based on Contact Electrification', Nano Lett., vol. 14, no. 6, pp. 3208–3213, 2014.

[21] Chunyan Li, Soohyun Lee, A. Gorton, M. J. Schulz, and C. H. Ahn, 'Dome or bump-shaped PVDF-TrFE films developed with a new mold-transfer method for flexible tactile sensors', in 2007 IEEE 20th International Conference on Micro Electro Mechanical Systems (MEMS), pp. 337–340, 2007

[22] C. Chang, V. H. Tran, J. Wang, Y.-K. Fuh, and L. Lin, 'Direct-Write Piezoelectric Polymeric Nanogenerator with High Energy Conversion Efficiency', Nano Lett., vol. 10, no. 2, pp. 726–731, 2010.

[23] P. Rey, P. Charvet, M. T. Delaye, and S. A. Hassan, 'A high density capacitive pressure sensor array for fingerprint sensor application', in Proceedings of International Solid State Sensors and Actuators Conference (Transducers '97), vol. 2, pp. 1453–1456., 1997

[24] H. Lee, J. Chung, S. Chang, and E. Yoon, 'Normal and Shear Force Measurement Using a Flexible Polymer Tactile Sensor With Embedded Multiple Capacitors', J. Microelectromechanical Syst., vol. 17, no. 4, pp. 934–942, ~~Aug~~. 2008.

[25] Y. Huang, H. Yuan, W. Kan, X. Guo, C. Liu, and P. Liu, 'A flexible three-axial capacitive tactile sensor with multilayered dielectric for artificial skin applications', Microsyst. Technol., vol. 23, no. 6, pp. 1847–1852,. 2017.

[26] J. A. Dobrzynska and M. A. M. Gijs, 'Polymer-based flexible capacitive sensor for three-axial force measurements', J. Micromechanics Microengineering, vol. 23, no. 1, p. 015009,. 2012.

[27] R. Surapaneni, Q. Guo, Y. Xie, D. J. Young, and C. H. Mastrangelo, 'A three-axis high-resolution capacitive tactile imager system based on floating comb electrodes', J. Micromechanics Microengineering, vol. 23, no. 7, p. 075004, 2013.

[28] A. M. Almassri, W.Z.Wan Hasan, S.A. Ahmad, A.J. Ishak, A.M. Ghazali, D.N. Talib and C. Wada, 'Pressure Sensor: State of the Art, Design, and Application for Robotic Hand', Journal of Sensors, Vol. 201512 pp., 2014, [Online]. Available: https://www.hindawi.com/journals/js/2015/846487/abs/. [Accessed: 25-Aug-2019].

[29] L. Yang, I. Akhatov, M. Mahinfalah, and B. Z. Jang, 'Nano-fabrication: A review', J. Chin. Inst. Eng., vol. 30, pp. 441–446,. 2007.

[30] S.R. Quake and A. Scherer, 'From Micro- to Nanofabrication with Soft Materials',| Science, vol. 290, no 5496, 2000, [Online]. Available: https://science.sciencemag.org/content/290/5496/1536. [Accessed: 25-Aug-2019].

[31] V. Zardetto, T. M. Brown, A. Reale, and A. D. Carlo, 'Substrates for flexible electronics: A practical investigation on the electrical, film flexibility, optical, temperature, and solvent resistance properties', J. Polym. Sci. Part B Polym. Phys., vol. 49, no. 9, pp. 638–648, 2011.

[32] H.J. Levinson, 'Lithography Process Control', Spie Press Book, 1999. [Online]. Available: https://spie.org/publications/book/322162?SSO=1. [Accessed: 25-Aug-2019].

[33] J. Melngailis, A. A. Mondelli, I. L. Berry, and R. Mohondro, 'A review of ion projection lithography', J. Vac. Sci. Technol. B Microelectron. Nanometer Struct. Process. Meas. Phenom., vol. 16, no. 3, pp. 927–957, 1998.

[34] C. H. Lee, D. R. Kim, and X. Zheng, 'Transfer Printing Methods for Flexible Thin Film Solar Cells: Basic Concepts and Working Principles', ACS Nano, vol. 8, no. 9, pp. 8746–8756,. 2014.

[35] D. Song, A. Mahajan, E. B. Secor, M. C. Hersam, L. F. Francis, and C. D. Frisbie, 'High-Resolution Transfer Printing of Graphene Lines for Fully Printed, Flexible Electronics', ACS Nano, vol. 11, no. 7, pp. 7431–7439,. 2017.

[36] S. Joshi, A. Savov, and R. Dekker, 'Substrate Transfer Technology for Stretchable Electronics', Procedia Eng., vol. 168, pp. 1555–1558,. 2016.

[37] K. J. Yu et al., 'Bioresorbable silicon electronics for transient spatiotemporal mapping of electrical activity from the cerebral cortex', Nat. Mater., vol. 15, no. 7, pp. 782–791,. 2016.

[38] B. Zhu, Z. Niu, H. Wang, W.R. Leon, H. Wang, Y. Li, L. Zheng, J. Wei, F. Huo and X. Chen, 'Microstructured Graphene Arrays for Highly Sensitive Flexible Tactile

Sensors', Small, vol. 10, no 18, pp. 3625-3631, 2014, [Online]. Available: https://onlinelibrary.wiley.com/doi/abs/10.1002/smll.201401207. [Accessed: 26-Aug-2019].

[39] S. Janfaoui, 'Électronique CMOS en silicium microcristallin sur substrat flexible transparent', thesis, Rennes 1, 2012.

[40] S.R. Forrest, 'The path to ubiquitous and low-cost organic electronic appliances on plastic', Nature vol. 428, pp. 911-918, 2004, [Online]. Available: https://www.nature.com/articles/nature02498. [Accessed: 26-Aug-2019].

[41] J. S. Lewis and M. S. Weaver, 'Thin-film permeation-barrier technology for flexible organic light-emitting devices', IEEE J. Sel. Top. Quantum Electron., vol. 10, no. 1, pp. 45–57, Jan. 2004.

[42] T. Kelley, 'High-performance Pentacene Transistors - Organic Electronics', Book Editor Dr. H. Klauk 2006, Wiley Online Library. [Online]. Available: https://onlinelibrary.wiley.com/doi/abs/10.1002/3527608753.ch2. [Accessed: 26-Aug-2019].

[43] T. Someya, T. Sekitani, S. Iba, Y. Kato, H. Kawaguchi, and T. Sakurai, 'A large-area, flexible pressure sensor matrix with organic field-effect transistors for artificial skin applications', Proc. Natl. Acad. Sci., vol. 101, no. 27, pp. 9966–9970, Jul. 2004.

[44] B. E. Kahn, 'Organic Electronics Technology', " Organic Electronics 1st Edition (Frankfurt Am Main: VDMA Verlag, 2006), p. 32.

[45] Y. Yang, X. Yang, X. Zou, S. Wu, D. Wan, A. Cao, L. Liao, Q. Yuan and X. Duan, 'Ultrafine Graphene Nanomesh with Large On/Off Ratio for High-Performance Flexible Biosensors', Adv. Funct. Mater., vol. 27, no. 19, p. 1604096, 2017.

[46] S. Bae, H. Kim, Y. Lee, X. Xu, J.S. Park, Y. Zheng, J. Balakrishnan, T. Lei, H. Ri Kim, Y. Il Song, Y.J. Kim, K. S. Kim, B. Özyilmaz, J.H. Ahn, B. Hee Hong and S. Iijima**,** 'Roll-to-roll production of 30-inch graphene films for transparent electrodes', Nature Nanotechnology, vol.5, pp. 574-578, 2010. [Online]. Available: https://www.nature.com/articles/nnano.2010.132?draft=journal. [Accessed: 26-Aug-2019].

[47] Y. Sun and J. A. Rogers, 'Fabricating Semiconductor Nano/Microwires and Transfer Printing Ordered Arrays of Them onto Plastic Substrates', Nano Lett., vol. 4, no. 10, pp. 1953–1959,. 2004.

[48] H. Gleskova, S. Wagner, W. Soboyejo, and Z. Suo, ‘Electrical response of amorphous silicon thin-film transistors under mechanical strain’, J. Appl. Phys., vol. 92, no. 10, pp. 6224–6229, Oct. 2002.

[49] R.C. Chittick, J.H. Alexander and .F. Sterling, ‘The Preparation and Properties of Amorphous Silicon’,J. Electrchem. Soc., vol. 116, no 1, pp. 77-81, 1969, [Online]. Available: http://jes.ecsdl.org/content/116/1/77.short. [Accessed: 26-Aug-2019].

[50] K. Belarbi, K. Kandoussi, N. Coulon, C. Simon, R. Cherfi, A. Fedala and T. Mohammed-Brahim, ‘Stability of Microcrystalline Silicon TFTs’, ECS Trans., vol. 16, no. 9, pp. 121–129, Mar. 2008.

[51] C.-H. Lee, A. Sazonov, and A. Nathan, ‘High-mobility nanocrystalline silicon thin-film transistors fabricated by plasma-enhanced chemical vapor deposition’, Appl. Phys. Lett., vol. 86, no. 22, p. 222106, May 2005.

[52] P.-C., A. Jamshidi-Roudbari, and M. Hatalis, "Effect of mechanical strain on mobility of polycrystalline silicon thin-film transistors fabricated on stainless steel foil", Appl. Phys. Lett. 91, 24, p. 3507 (2007); https://doi.org/10.1063/1.2824812

[53] J. H. Cheon, J. H. Bae, and J. Jang, ‘Mechanical stability of poly-Si TFT on metal foil’, Solid-State Electron., vol. 52, no. 3, pp. 473–477, Mar. 2008.

[54] D.-H. Kim, R. Ghaffari, N. Lu, and J. A. Rogers, ‘Flexible and stretchable electronics for biointegrated devices’, Annu. Rev. Biomed. Eng., vol. 14, pp. 113–128, 2012.

[55] D.-H. Kim, J. Xiao, J. Song, Y. Huang, and J. A. Rogers, ‘Stretchable, curvilinear electronics based on inorganic materials’, Adv. Mater., vol. 22, no. 19, pp. 2108–2124, May 2010.

[56] R. V. Martinez, ‘Flexible Electronics: Fabrication and Ubiquitous Integration’, Micromachines, vol. 9, no 11, pp. 605, 2018.

[57] D. Wang, Y. Zhang, X. Lu, Z. Ma, C. Xie, and Z. Zheng, ‘Chemical formation of soft metal electrodes for flexible and wearable electronics’, Chem. Soc. Rev., vol. 47, no. 12, pp. 4611–4641, Jun. 2018.

[58] C.-H. Liu and X. Yu, ‘Silver nanowire-based transparent, flexible, and conductive thin film’, Nanoscale Res. Lett., vol. 6, no. 1, p. 75, Jan. 2011.

[59] Y. Yu et al., ‘Three-dimensional compressible and stretchable conductive composites’, Adv. Mater. Deerfield Beach Fla, vol. 26, no. 5, pp. 810–815, Feb. 2014.

CHAPTER 2 - N-type µC-Si investigated as a pressure sensor

1. Introduction

Nowadays, there are many flexible technologies used to perform physiological measurements. The aim of this section is to give an overview of flexible electronic devices; how to work with thin-film layers or how to select them depending on the application.

First, an introduction of the techniques used in the IETR laboratory to deposit microcrystalline silicon (µc-Si) at low temperature is presented. The piezoresistive properties of these materials are explained.

In addition, some points about the highlight of the fabrication process of our devices and the problems found during the development are discussed.

The final goal is to implement a flexible device that combines good sensitivity and high resolution.

2. Deposition techniques of µc-Si at low temperature

Generally, the mechanical properties of any flexible thin-film material will strongly depend on the temperature used for its deposition.

In IETR laboratory, the most widely used deposition method for microcrystalline silicon at low temperature is plasma-enhanced chemical vapor deposition (PECVD). While there are other methods available in the laboratory for depositing silicon, such as sputtering or low-pressure chemical vapor deposition (LCPCVD), these techniques don't achieve the same quality than PECVD.

Microcrystalline silicon deposited at low temperature, 165°C, had been optimized in the laboratory in 2007 [1] making it compatible with flexible substrates such as PEN or Kapton.

However, the acquisition by the laboratory of a new machine -based on the technique of inductively-coupled-plasma chemical vapor deposition (ICPCVD), requires us to investigate whether this method allows us to obtain microcrystalline silicon with better characteristics.

Although both techniques belong to the same principle of chemical vapor deposition (CVD) that it is based on deposit of thin films from vapor phase by the decomposition of chemicals on the substrate surface, there are some differences between them. For that reason, their working principle and a comparison between these two techniques are s first presented in this chapter.

2.1 Description of deposition system with PECVD reactor

Plasma enhanced chemical vapor deposition (PECVD) is a process used to deposit thin films from a gas vapor state to a solid state on a substrate. When a radio frequency (RF) power between two electrodes is generated, the plasma is created, involving the chemical reactions of the gases. The plasma produces energetic electrons, ions and free radicals, which assist the chemical reactions. The machine is formed by 3 parts: deposition reactor, pumping system and gases management system.

- Deposition reactor has two parallel electrodes; the anode that supports the substrate and is connected to ground and the cathode that it is connected to a RF source. Between the cathode and the RF source, there is a tuning box that allows the compensation of the reflected power. By adjusting it, it is possible to adjust the RF power applied. The substrate can be heated up to 350°C, depending on the film requirements. RF generator creates an alternative field at 13.56 MHz, this power can be regulated from microwaves to higher MHz [2], [3]. The distance between the electrodes is adjustable and this parameter can be very relevant to obtain a good quality film.

- Pumping system is constituted by a primary pump that provides a vacuum level about 2.10^{-2} mbar and a secondary pump that adjust the vacuum level until 10^{-6} mbar.

- Gases management system: the gases used during the deposition are controlled by flow meters that are located behind the reactor. The main gas used are Silane (SiH_4), Hydrogen (H_2) and Argon (Ar). Other gases can be added in order to obtain doped layers: phosphine (PH_3) or arsine (AsH_3) for n-doped layers or diborane (B_2H_6) for p-doped layers.

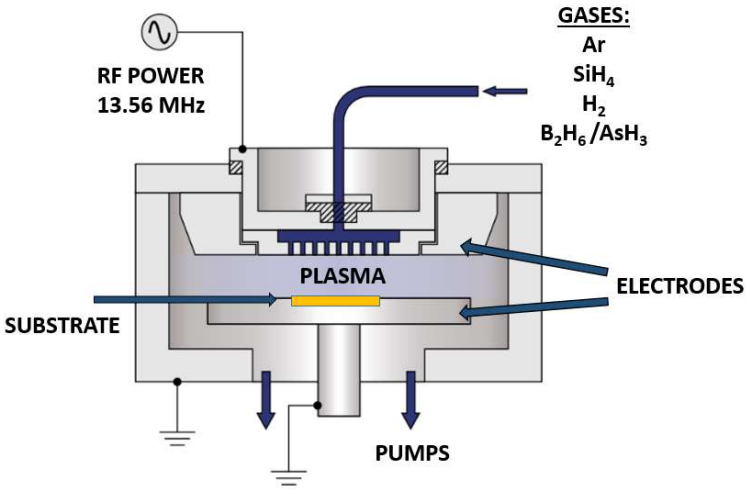

Figure 2-1. Schematic PECVD reactor.

2.2 Description of deposition system with ICP-CVD reactor

High Density Plasma Chemical Vapor Deposition (HDPCVD) is a special form of CVD technique that employs an Inductively Coupled Plasma (ICP) source to generate a higher density plasma with lower deposition pressures and temperatures than PECVD system.

With higher plasma density, it could be possible to obtain some advantages as for example, high-quality films using lower deposition temperatures than PECVD (typically 80°C to 150°C) or a better uniformity.

Generally, the inert gases go through the ICP source, and the reactive gases are introduced through a gas ring that is close to the lower electrode. Depending on the film required property, the lower electrode can be powered (~ 10W) or left floating (~ 0 W).

Most ICP-CVD systems process through a turbomolecular pump which limits the gas flowed into the chamber, and leads to lower deposition rates.

As in PECVD machine, a parallel electrodes reactor is used. The sample is placed on a grounded bottom electrode and RF voltage is applied to the upper electrode. This forms the plasma. For ICP-CVD machine the bottom electrode can be heated in a range 100-400°C.

To deposit low temperatures high-density films, even with temperatures lower of 100°C. A high- density-plasma (HDP) source is used, in which the electrons of the plasma are excited in a direction parallel to the chamber boundaries. The HDP source corresponds to the inductively coupled plasma (ICP) chamber. On this module, the plasma is driven by a magnetic potential set up by a coil wound outside chamber walls, as shown on figure 2-2. The electron current direction is opposite to that of the coil currents which are, by design, parallel to the chamber surfaces.

The inductively coupled coil is linked to a 13.56 MHz RF generator. This generator is not the same as the one used to power the lower electrode. This lower electrode, as in PECVD, is powered separately by another 13.56 MHz generator, which enables independent control of the energy of the ions of the plasma. The dissociation of the plasma and the density of the incident ions in the chamber is controlled by ICP coil power.

As it was commented previously, ICP-CVD is a new deposition technique in the laboratory, due to that, it appeared the necessity to investigate which are the optimum conditions to perform the N-type µc-Si deposition at low-temperature. With this machine, we will try to achieve film densities similar to PECVD but with better step coverage and at lower process temperatures. Also, it can offer the possibility to control the stress induced in the films due to the low ion energies.

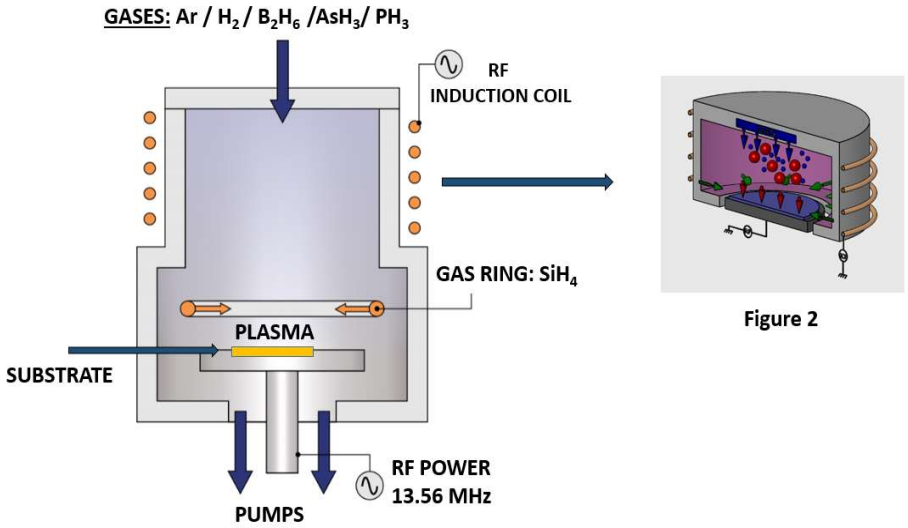

Figure 2-2. Schematics of high- density-plasma (HDP) chamber [3] and ICP-CVD reactor.

To summarize, Table 2-1 presents the main advantages of ICP-CVD technique over PECVD and some disadvantages.

Table 2-1. Advantages and disadvantages of ICPCVD technique compared to PECVD.

ICP-CVD	
Advantages over PECVD	**Main disadvantage**
High density plasma Low deposition pressures Lower range of temperatures process Lower induced stress Good step coverage	High cost of equipment New technique in the laboratory - necessity to investigate optimum deposition conditions

3. Flexible devices with microcrystalline silicon

Microcrystalline silicon deposited by PECVD technique was widely investigated in the IETR. To achieve a good quality on these materials, there are several parameters that were deeply studied such as the temperature or the pressure used during the deposition process, the percentage of SiH_4, H_2 or Ar in the gases dilution or the selected power. This semiconductor material was optimized during K. Kandoussi thesis [4] , fixing then the parameters that were used in the follow research.

There are different devices fabricated with this material, however here we will introduced briefly those that was fabricated onto flexible substrate.

The first example of µc-Si on a flexible substrate was realized during S. Janfaoui's thesis [5]., He has developed µc-Si top-gate thin film transistor (TFT) on 5 x 5 cm^2 sheets of PEN (Polyethylene naphthalene). In this work, the thickness of the sheets of PEN is 125 µm and it is encapsulated on both sides with 250 nm of Silicon Nitride. Over it, a layer composed of 100 nm thick undoped µc-Si and 70 nm thick N doped µc-Si is deposited. Here, the devices are characterized under static deformation with different curvature radius. They are bent under tensile and compressive stress. The main goal was to study the electrical and mechanical behaviors of these TFTs under mechanical stress. Figure 2-3 shows the architecture of the TFT used during this thesis.

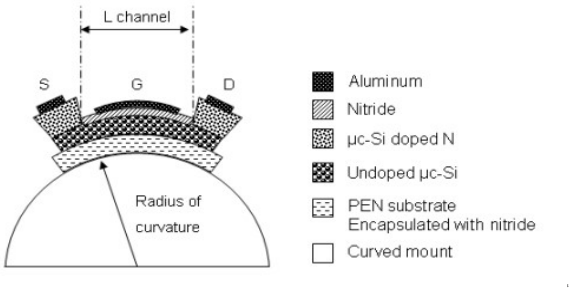

Figure 2-3. Schematic TFT developed in S. Janfaoui's thesis.

The following example of µc-Si used with a flexible substrate at IETR, was during Y. Kervran's Thesis [6]. The design of the devices consists in Transmission Line Measure method (TLM) and a strain gauge matrix using a Kapton substrate with different thicknesses of 125 µm and 50 µm. The goal of this thesis was to investigated if µc-Si has the ability to be used as a pressure sensor. The characterization test consists in submitting the devices to different curvature radii and to verify their sensitivity to the deformations. Figure 2-4 shows an example of the strain sensor used.

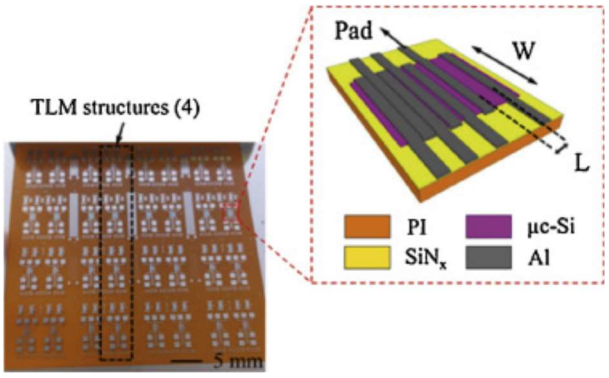

Figure 2-4. Schematic TLM structure developed during Y. Kervran's thesis.

Hence, taking into account these previous results of the laboratory where µc-Si was used on a flexible substrate; our project is to submit our samples to a dynamic and continuous deformation, because this it will verify the reliability of µc-Si as a pressure sensor. Moreover, this will give us more information about the material's behavior especially during dynamic strain. It was then necessary to create a dynamic acquisition system and try to find a structure that responds fast and exhibit a linear response to strain deformations. For this, different possibilities have been studied, such as reducing the thickness of the substrate to 25 µm or creating new designs to facilitate the recovery of the structure. All of this will be explained throughout this thesis.

4. Piezoresistive properties of N type µc-Si

To properly understand the piezoresistive properties of µc-Si, some concepts need to be introduced.

Our sensors are based on piezoresistive effect and, as it was explained in Chapter 1, when a material is deformed by an applied mechanical stress, an electrical change is produced and the resistance value varies. As shown in formula (2-1), a change in the resistance value (R) can be produced by the change of the resistivity or by the geometry.

$$R = \rho \frac{L}{S} \tag{2-1}$$

Where ρ is the resistivity, L corresponds to the length and S is the surface area of the sensing material, µc-Si in our case.

To quantify the sensitivity of the material to the applied mechanical stresses, the gauge factor (GF) is defined. As shown by the formula (2-2), it is formed by two components: the geometrical distribution (1+2υ) and the variation of the resistivity in function of the strain (Δρ/ε), where υ is the Poisson's ratio, ρ the resistivity and ε the axial strain applied.

$$GF = \frac{\Delta R/R}{\varepsilon} = (1 + 2v) + \frac{(\Delta\rho)}{\varepsilon} \tag{2-2}$$

For the metal strain gauge, the resistivity of the metal lines does not vary with the strain, therefore the equation (2-3) can be written as:

$$GF = \frac{\Delta R/R}{\varepsilon} = (1 + 2v) \tag{2-3}$$

Normally, the Poisson's ratio value is between $0.3 < \upsilon < 0.5$, so that their GF is in the range $1.6 < GF < 2$. [7]

However, for semiconductor materials like silicon, both terms of the Formula (2-2) should be considered, which means that the values obtained for the gauge factors can be several orders of magnitude higher than the metal ones. Hence, it is important to understand well the second term of the equation, and especially how the resistivity is changing.

When a material is understressed, it exhibits a constant resistivity, but when the structure is deformed by an external force, the lattice changes produce a change in the resistivity.

In the case of single crystalline silicon, it presents a diamond cubic lattice form described in Chapter 1. Generally, silicon is doped with impurities in order to increase its conductivity. Depending on the dopant used, this can be an electron donor or an electron acceptor.

When a semiconductor material is doped, it means that the bandgap is controlled by adding small impurities to the material. These impurities can change the electrical conductivity of the

lattice and therefore vary the performance of the semiconductor. Depending on the majority carriers ratio, it exists two different kinds of extrinsic semiconductors, p-type (holes are the majority) and n-type (electrons are the majority).

Depending on the direction than the stress (tensile or compressive) applied, the lattice structure is affected, generating a change in the carrier mobility (electrons and holes) through the lattice. Hence, the mobility of the carriers affect the resistivity of the material, as expressed for example with n-type material in equation 2-4.

$$\rho = \frac{1}{n\mu q} \tag{2-4}$$

Where μ is the carrier mobility, q is the absolute value of the electronic charge, and n is the concentration of free carriers.

In cases of n-type materials, where most charge carriers are electrons, when a tensile strain is applied, the interatomic spacing of the lattice will increase and that generates an increase of the mobility and thus a decrease of the resistivity. When a compressive strain is applied, the interatomic spacing decreases, reducing the mobility and increasing the resistivity.

Hence, the sensitivity of silicon to the strain depends on its crystalline orientation with respect to the applied field and also on its type of dopant.

In our case, the material used is N-type μc-Si and the gases used for doping are arsine and phosphine, and as explained before. We decided to dope because more the GF factor is high, higher is the sensitivity of the devices and this has a direct link with the doping concentration.

5. Mechanical behavior of thin films

In order to obtain sensors with good reliability, it is important that the total structure has the ability to come back fast to the initial state. The mechanical behavior of the compound structure depends on several properties such as the Elastic or Young Modulus, the hardness or the adhesion of the layers and the thickness of each part.

Nowadays, one the main disadvantage of reducing the thickness of the film is the fabrication process and handling due to the fragility of thin layers. However, during recent years, many remarkable advances in the technology of thin-film deposition and etching process technology have been achieved, thereby improving the quality of the films as well as their adhesion to the substrate.

The understanding of the behavior of thin materials is necessary and the definition of parameters that helps their classification is mandatory. Briefly, some basic concepts and definitions that need to be consider during the film selection to fabricate flexible devices are introduced.

- Young Modulus: It measures the elastic properties of a solid material when submitted to tension or compression in one direction. It is defined in formula 2-5 as the relationship between stress (force per unit area, σ, see equation 2-6) and strain (deformation in a solid due to the stress, ε, formula 2-7) of a material in the linear elasticity regime.

$$Young Modulus\ (E) = \frac{Stress}{Strain} = \frac{\sigma}{\varepsilon} \tag{2-5}$$

$$\text{Stress } (\sigma) = \frac{\text{Force(F)}}{\text{Area (A)}} \tag{2-6}$$

$$\text{Strain } (\varepsilon) = \frac{\Delta\text{L (change in large)}}{\text{L (original large)}} \tag{2-7}$$

The Young modulus should be constant for a given material. This parameter has a direct link with the elasticity and is also called Elastic Modulus (Y). When a material presents high elastic modulus, it is classified as stiff material and if the elastic modulus is low, it is classified as compliant.

- Hooke's Law: it expresses mathematically the relationship between the stress and the strain, as illustrated Figure 2-5. It demonstrates that, when an elastic material stays inside the elastic stress region, the stress should be linearly proportional to the strain. Also, in this region, the loading is reversible. However, one time that the elastic limit has been overcome and the stress vs. strain curve starts to deviates from the linear region, the deformation of the material will be irreversible.

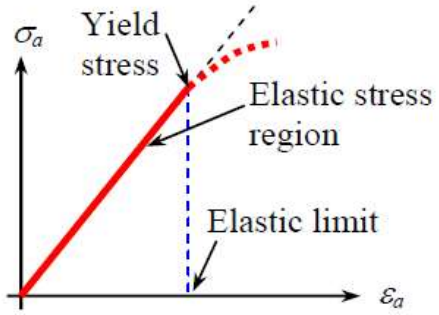

Figure 2-5. Stress (σ) vs. strain (ε) relation.

The mechanical behavior of thin films (f) on thin substrates (s) depends on the geometry, the elastic modulus (Y) and the thickness (d) of each part. In function of the two last parameters the behavior of substrate/film structure could be classified in:

i. **Yf .df << Ys .ds.** When the thickness and the elastic modulus of the deposited film is very low compared with the substrate ones, the substrate dominates and the film complies with it. The effect of the stress in the substrate is small and the film/substrate couple suffers from slight curves, even when the film is highly stressed.
ii. **Yf .df >> Ys .ds.** When the thickness and the elastic modulus of the substrate is very low compare to the film ones, the film dominates and the substrate complies with it.

In our case, the film dominates and the stress in the film creates a deformation on the film/substrate structure. The structure is bent with a radius of curvature R. This level of the curvature depends on the nature of the substrate, and especially on its thickness.

Film stress is usually calculated with Stoney's equation, which relates the biaxial modulus of the substrate, thickness of the film and substrate, and the radius of curvatures of pre- and post-process.

Stoney relation.

The Stoney relation is generally used to calculate the residual stress value for the linear, elastic region of the stress-strain curve. In the literature, there are different versions of this equation depending on the substrate type [8]. However, to apply this formula, all the versions should respect these two hypotheses:

(a) Film stress can be evaluated with the final measure of the curvature of the substrate (or change of curvature, if this was not initially flat).
(b) Results do not depend on the properties of the film, thus the measurement of the substrate curvature gives the current stress in the film.

Stoney Formula is presented for the case where the substrate stiff and the case where the substrate is compliant to the film.

- When the substrate is stiff and the film conforms to it ($Y_f .d_f << Y_s .d_s$). In this case, the stress in the substrate is smaller than in the film, so the substrate dominates, making that

the biaxial stress arise only for plane, Formula 2-8 (a). By this way, the radius of curvature (Ro) is given by Formula 2-8(b):

$$\sigma_f = \frac{\varepsilon_M \, Yf}{(1-\nu f)} \qquad \text{(2-8a)} \qquad Ro = \frac{Ys}{6\,\sigma_f\,(1-\nu s)}\frac{ds^2}{df} \qquad \text{(2-8b)}$$

Where ε_M is the biaxial mismatch strain, Y_f and Y_s are the biaxial elastic Young's modulus of the film and the substrate, d_s the thickness and ν_s the Poisson's ratio of the substrate, d_f the thickness of the film.

- When the substrate complies the film ($Y_f.d_f >> Y_s.d_s$). In this case, the substrate bents into a roll. The substrate is considerably deformed and the curvature radius (R_o) can become very small. In our case, during the deposition process, the substrate is held with a rigid frame, so the substrate is flat. The stress in the film is given by formula 2-9(a) where $Y_f^* = Y_f / (1-\nu_f)$, is the biaxial elastic modulus of the film.
  On this case, the stress in the film also depends on the thickness and elastic modulus of the substrate. The stress in the substrate is given by formula 2-9(b), and as result, the substrate will bend into a roll with a radius of curvature defined by the formula 2-9(c).

$$\sigma_f = \frac{\varepsilon_M Y_f^*}{1+\left(Y_f^* d_f\right)/\left(Y_s^* d_s\right)} \qquad \text{(2-9a)} \qquad \sigma_s = -\frac{\sigma_f d_f}{d_s} \qquad \text{(2-9b)}$$

$$Ro = \frac{\left(\overline{Y}_s d_s^2 - \overline{Y}_f d_f^2\right)^2 + 4\overline{Y}_f \overline{Y}_s d_f d_s \left(d_f + d_{hs}\right)^2}{6\varepsilon_M (1+\nu)\overline{Y}_f \overline{Y}_s d_f d_s \left(d_f + d_s\right)} \qquad \text{(2-9c)}$$

On Figure 2-6, it can be observed that, following formula 2-9 (c), it is possible to normalize the curvature radius of the film/substrate structure as a function of d_f/d_s [9]. The dashed lines represent the Stoney formula and the continuous lines are the response of a steel or Kapton substrate when applying this formula 2-9(c). However, this curve is not valid for the case where the film conforms to the substrate, formula 2-8 (b). In our specific case, Kapton HN substrate has a Young's modulus equal to 2.5 GPa and for N type µc-Si the Young's modulus is between [80 – 100 GPa]. Thus, Y_f/Y_s will be around 35.

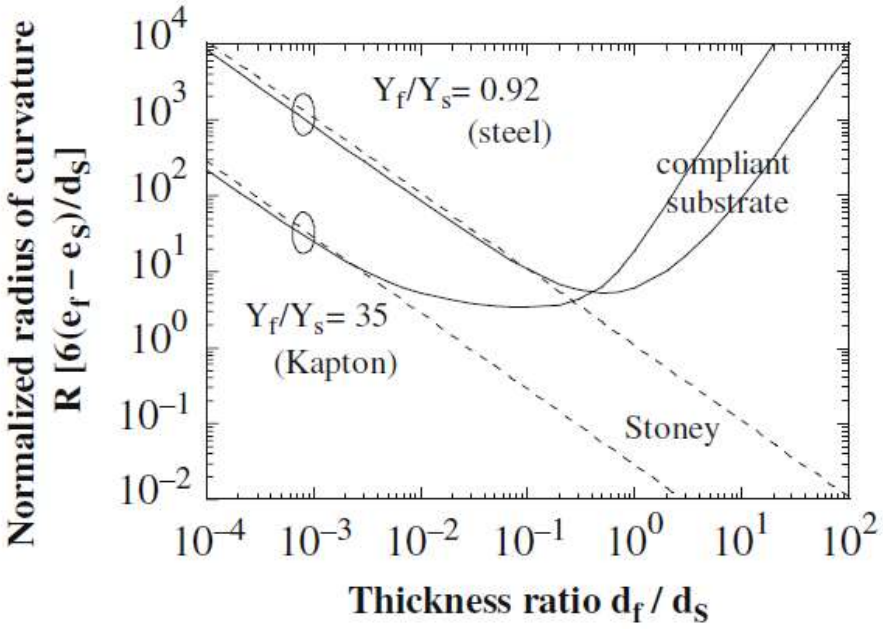

Figure 2-6. Normalized radius of curvature when the substrate compliant to the film [9].

5 Fabrication technology on thin film flexible devices

Traditionally, electronic devices are fabricated onto rigid substrates. However, the recent needs for devices that can be bend, rolled or stretched give rise to the flexible electronic. The reduction of the thickness in the different films generates some mechanical and electrical problems. In the following, the main manufacturing difficulties to perform thin film devices on flexible substrate will be introduce.

One of this problem comes from the thermal contraction of the substrate and the built-in stress of the films during and after the deposition step. This fact generates a curve and a change in the in-plane dimensions of the device.

Another common issue is the mismatch between the substrate and the deposited layers. This stress induces some problems like cracks or delamination in the layers. Usually, the stress on thin-film substrate appears during the depositions step, and is due to the difference between the thermal expansion/contraction coefficients or other reasons as the uptake and release of humidity in the substrate.

To try to avoid these effects, flexible electronics devices need to be handled on a rigid carrier during the manufacturing process. After depositing the layers that will form the structure of the

device, the flexible substrate needs to be flattened and temporarily bounded to a wafer or a glass until the end of the process.

Hence, we try to minimize the cracks produced on the device films or the mismatch during the alignment step due to stress-induced curvature.[10]

The misalignment and the curvature increase when the substrate is thinner. These effects will increased by using a 25 µm thick Kapton compared to a 50 µm thick ones. Different techniques such as an adhesive can be used to paste temporally the substrate. In all cases, the chosen method should be resistant to the chemicals used during all the process, should support temperature and be easy to remove at the end of the process, moreover as this last step could create some damages in the structure too. In order to minimize the effect of the cracks and the built-in stress introduced during film growth, various studies have been done and are described further. But first, the different kind of stress produced on thin-films and their classification in function of the origin are presented, in order to better understand how to minimize them.

5.1 Source of stress in thin film

A film's stress affects the performance, reliability and durability of the devices. This stress depends on the deposition conditions and the physical properties of the film and the substrate. Stress sources can be induced by differential thermal expansion or contraction of the films, depending also on the deposition method, by the release of humidity, or is influenced by the interface between film and substrate, etc. The origins of the stress could be of three types: intrinsic, thermal or mechanical. Often, intrinsic or thermal terms refer to residual stress. Mechanical stress may appear in the layer due to bending or stretching of the structure. The following section focuses on the description of these concepts.

5.1.1 Thermal stress

Thermal stress is caused by differences by differences in thermal expansion between the films and the substrate. It is usually caused by cooling from the deposition temperature to room temperature. The mismatch in the thermal expansion coefficients (CTE) of the substrate and the film can produce the film/substrate bending. This difference causes a contraction or expansion of the dominant material that extends to the rest of the structure. Figure 2-7 (a) shows the effect of the residual stress in the film due to compressive bending. Figure 2-7 (b) corresponds to the case where the CTE of the substrate is lower than the CTE of the film, producing a bending due to residual tensile stresses in the structure (compressive stress in the

film). When we process with thick and stiff substrates the effect of the thermal stress is hard to see with the naked eye, such as on a silicon wafer.

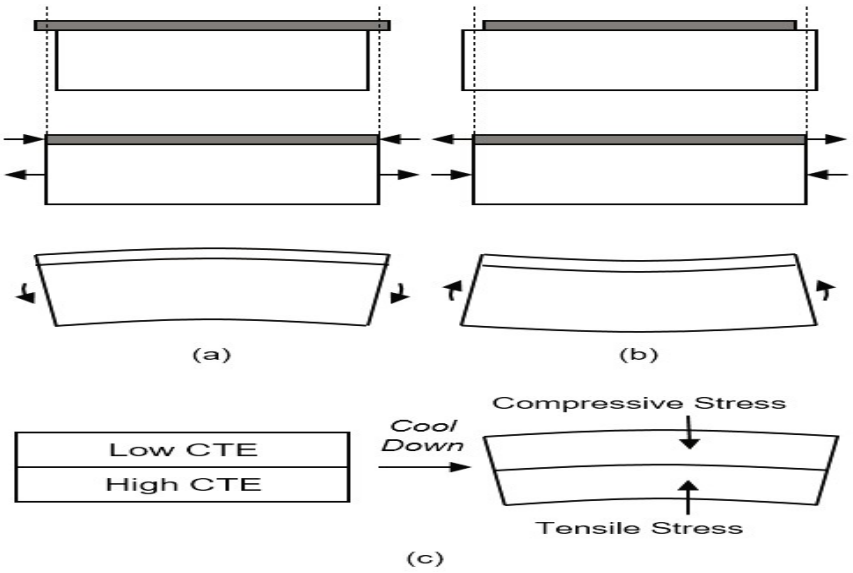

Figure 2-7: Film/substrate bending due to (a) compressive and (b) tensile residual stresses in the film and (c) due to mismatch of the coefficients of thermal expansion [11].

5.1.2 Intrinsic stress

It is defined as the stresses distribution that is present in the film during the deposition/ growth step films when these are deposited under non-equilibrium conditions (as always the case of plasma deposition). It strongly depends on the deposition process conditions, the impurities, the materials involved, the grain boundaries or of the energy ions …

Figure 2-8 shows the effect of the energy ions on the film. When the plasma has low energy ions, the substrate suffers tensile stress. For the contrary, if the ions have high energy during the deposition the substrate suffers compressive stress.

ICP-CVD machine could offer the possibility to control or decrease the stress induced in the films, due to the low energies ion.

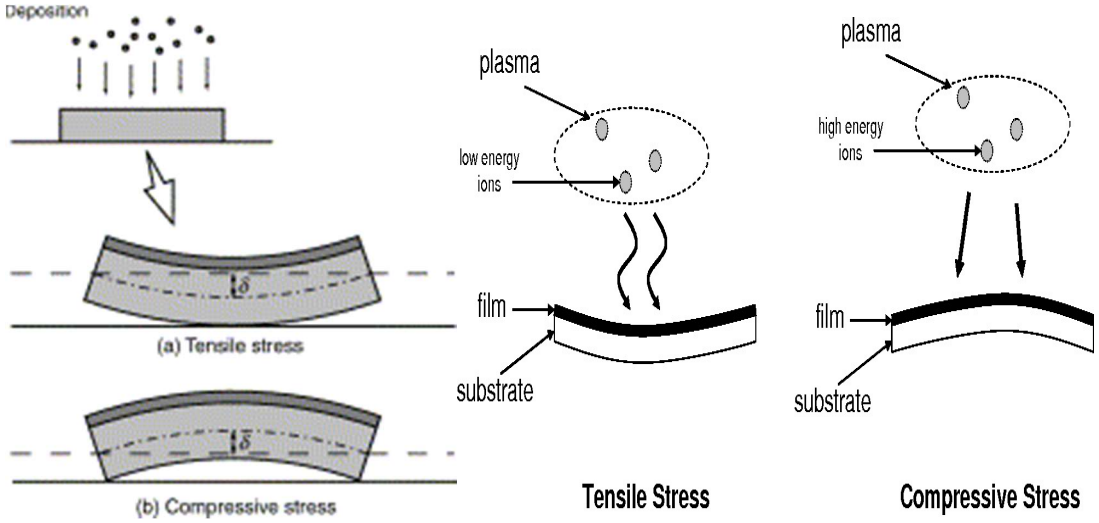

Figure 2-8. Effect of intrinsic stress on delamination.

5.1.3 Epitaxial stress

Epitaxial misfit stresses arise when there are no coherent interfaces between films and substrates, i.e., when a mismatch exists in the crystal lattices in film and substrates. The strain misfit is calculated as:

$$\varepsilon = \frac{a_{film} - a_{substrate}}{a_{substrate}} \tag{2-10}$$

Where a_{film} and $a_{substrate}$ are the lattice parameters correspond to the film and the substrate. This effect is represented in figure 2-9.

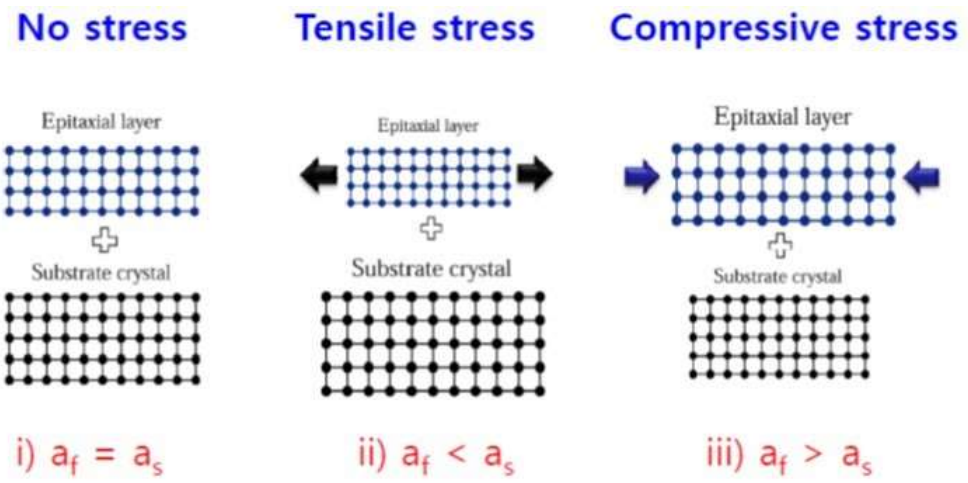

Figure 2-9. Effect of epitaxial stress [12].

5.1.4 Mechanical stress

Others external stresses may occur in the films due to mishandling. When the structure is extremely bended or stretched, it can create some damage, like debonding form by peeling or buckling. Figure 2-10 shows and example of this effect.

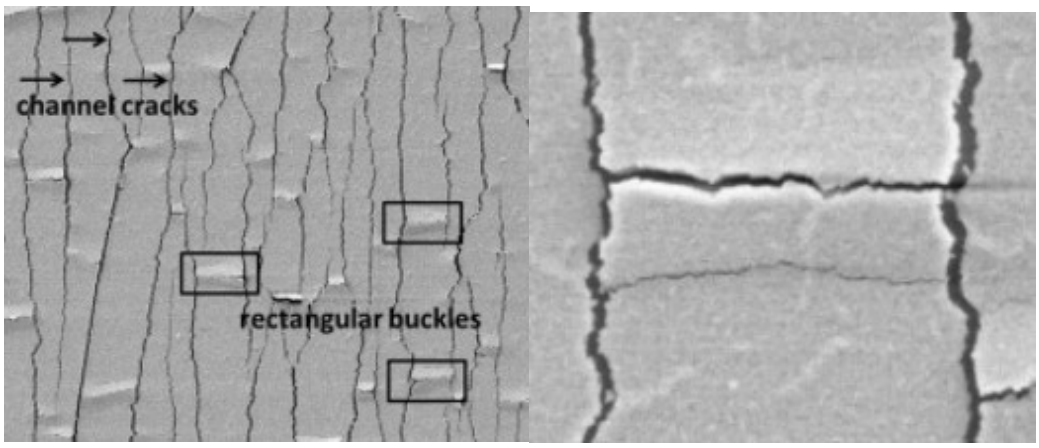

Figure 2-10. Effect due to mechanical stress [13].

6 Process and technological problems

In our case, during the manufacturing process, the main difficulties were associated with the low thickness of the substrate. The handling steps during etching, cleaning or deposition create some stress issues. As explained in the previous section, it is not surprising that after proceeding to a chemical vapor deposition (CVD) a deformation appears in the substrate. This residual stress results from the difference in the CTE of the film and the substrate (thermal stress) and from ion bombardment during plasma deposition (intrinsic stress) which damages the structure and induces misalignment in the following masking levels.

The first experiments had been first carried out on Kapton substrate of 50µm thick. The thickness of this substrate was not very low, for that reason, the problems due to the induced stress does not have a major effect on the global structure.

However, for the major experiments, the thickness of Kapton is only 25µm. Here, as show Figures 2-11 and 2-12 after µC-Si deposition, the global structure exhibited a roll-on deformation, causing cracks on the sensing material.

In the following sections, the fabrication process for our sensors is presented with the different approaches used to reduce stress-related problems.

Figure 2-11. Effect over Kapton 25µm after deposited the µC-Si.

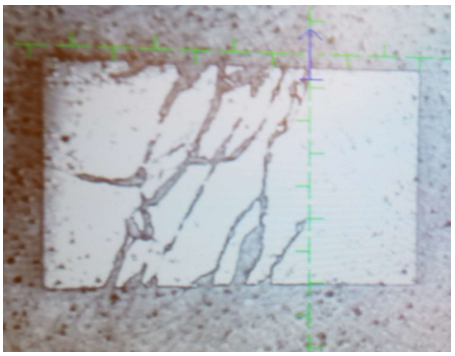

Figure 2-12. Cracks found in the µC-Si after roll-on effect.

6.1 Approaches to reduce stress related problems

Generally, the equipment available in the laboratory are focused towards the fabrication process on rigid substrates such as glass or silicon wafers. However, some of them are also compatible with plastic substrates. In order to improve the performances and reliability of devices, it is necessary develop an adapted fabrication process. This part presents the different problems found during the manufacturing steps, especially during deposition and lithography steps.

Moreover, it is dedicated to the treatment of stress problems and its consequences through three proposals: SiNx encapsulation, shadow mask and stability treatment of Kapton.

The photolithography machine available holds the samples using vacuum in the backside. This equipment is perfect for rigid substrates. However, if the substrates have thickness lower than 50 µm, the thin substrate needs to be temporally fixed on a rigid one (silicon wafer or glass) to avoid deformations due to the vacuum. Sticking the samples also helps for all the fabrication process and reduces the possibility to damage the structures during handling. For all these reasons, in order to adapt our process, different ways to stick the substrate on a rigid support is investigated.

As a first option, the substrate is stuck on glass or wafer support with Kapton adhesive, placed in the four corners of the sample. This option has the advantage to be easy. However, the main problem found with this technique is the infiltration of water, solvents or acids during the fabrication process, as shown in Figure 2-13. Those liquids accumulate between the sample and the support. To avoid their absorption in the Kapton, it is necessary to remove the tape and to dry it, fact that complicate the process and can induce some cracks in the layers.

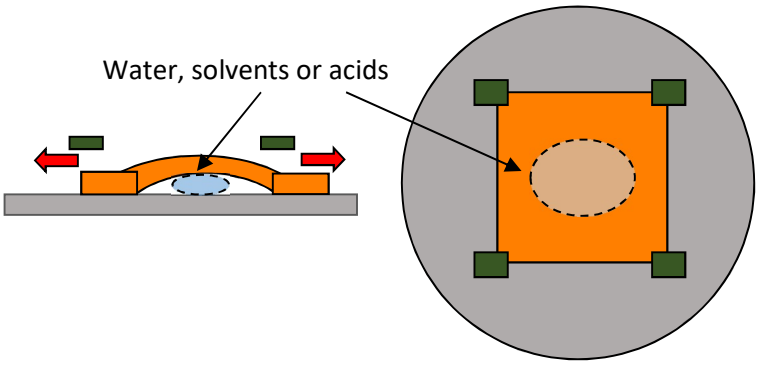

Figure 2-13. Issues of temporary bonding on silicon wafer.

The other solution, that was selected, is to deposit by spin coating a thin layer of PDMS over a silicon wafer as shown Figure 2-14. PDMS layer allows to stick the Kapton substrate, which will be removed from the wafer only at the end of the process. To avoid the bubbles between Kapton and PDMS, the sample is put under vacuum.

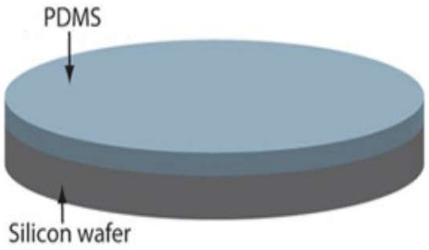

Figure 2-14. Support for temporary bonding using a thin film of PDMS.

6.2 Solutions for mechanical stresses introduced during fabrication

As it was commented before, strains/stresses in the film/substrate structure can create some cracks or delamination in the film and curling or buckling problems in the substrate, thus changing the dimensions in-plane of the structure. All of these factors affect devices performance and create some alignment problems between the different layers that constitute

the device. The thinner the thickness of the substrate is, the greater the curvature and the misalignment are [14]. For that reason, a proposal has been studied to try to compensate for all these effects.

6.2.1 Effect of SiNx encapsulating layers

Following literature recommendations [10], a silicon nitride layer can be used to try to compensate the tensile built-in stress between Kapton substrate and µc-Si after deposition. Silicon nitride can be used for several goals, as to protect the substrate against chemical processes or to provide adhesion of the other layers. But it can also be used to balance the stress-induced curvature [10]. Figure 2-15 shows a clear example of how is it possible to balance the ion induced stress on Kapton by adjusting the RF deposition power on PECVD machine from 5 to 25 W. The deposition temperature used for this experiment was 150°C [10].

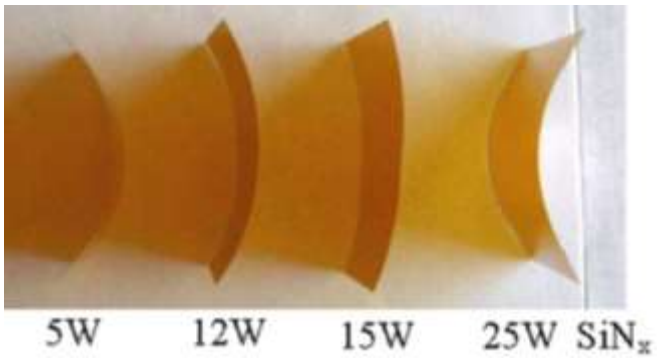

Figure 2-15. Curvature induced by stress in films of (b) SiNx [10].

In our case, the parameters selected to use silicon nitride as encapsulation layer were the same ones used for previous thesis in IETR laboratory [15] [16] and it is presented in Table 2-2.

Table 2-2. Conditions used for SiNx layer

Parameters	Power (W)	Pressure (mbar)	Distance electrodes (cm)	Temperature (T °C)	SiH_4 (sccm)	N_2 (sccm)	H_2 (sccm)
SiNx	50	0.3	4.5	150	1	100	5

In order to balance the induced stress after µc-Si deposition and see if silicon nitride layer has some effect on the devices performance, three different structures are compared (figure 2-16):

a) µc-Si was deposited directly on the Kapton substrate.
b) Encapsulation of Kapton on one side of the substrate with 50nm SiNx
c) Encapsulation of Kapton substrate in both sides.

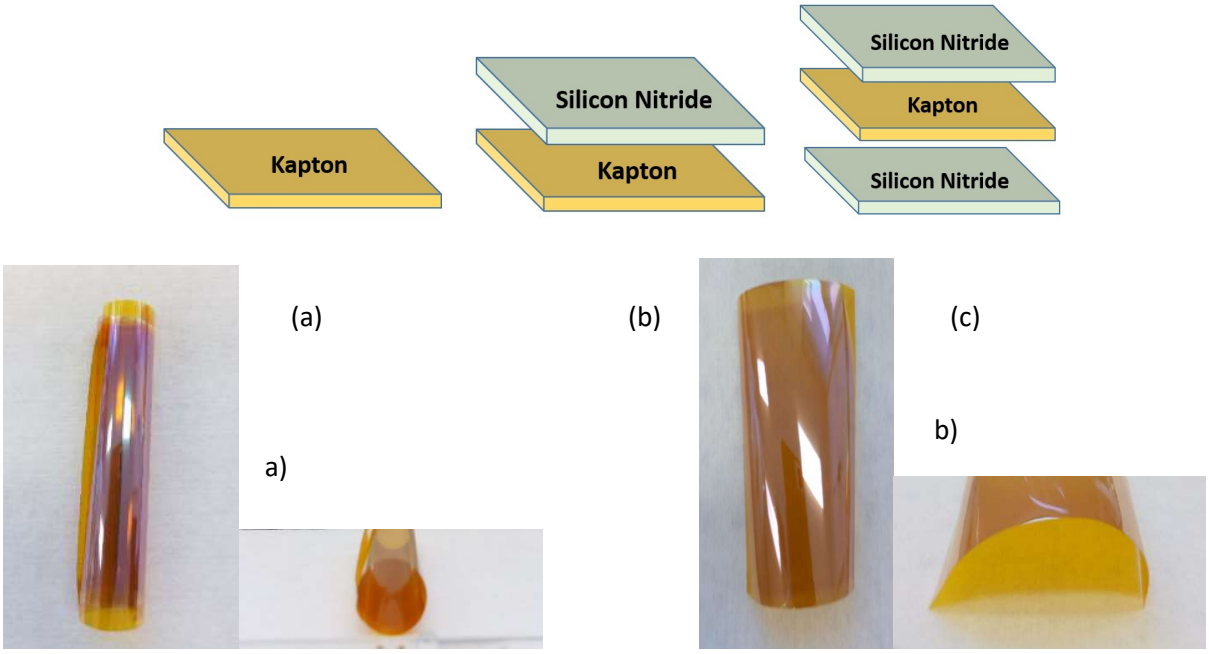

Figure 2-16. Structure for 25 µm of Kapton after µc-Si deposition a) without any encapsulation layer b) and c) with SiNx layer encapsulation.

Figure 2-16 shows the visual effect of Kapton substrate when µc-Si is directly deposited over it a) and when encapsulation of the kapton is performed before deposition of µ-Si b) and c). It can be observed that with an encapsulation of SiNx, the curvature due to the induced stress is considerably reduced. However, when Kapton is encapsulated on one side b) and on both side c), the induced-stress curvature seems to be the same.

Therefore, it can be conclude that using SiNx as encapsulation layer allows to control the induced-stress after µc-Si deposition, and should reduce the cracks and the misalignment problems.

The next step is to verify if this encapsulation has some effect on the electrical performance of the sensor. To do that, when the fabrication process is finished, the sensors are measured before and after being submitted to different deformations. Figure 2-17 shows the three different structures and the shift produced in the resistance before and after deformation. The calculation of the shift value is the result of subtracting the final resistance value (R_f) minus the initial value (R_0) :

$$\text{Shift} = R_f - Ro \tag{2.11}$$

With Ro is the initial value of the resistance and R_f corresponds to the value of the resistance in flat position, after been submitted to different strain deformations.

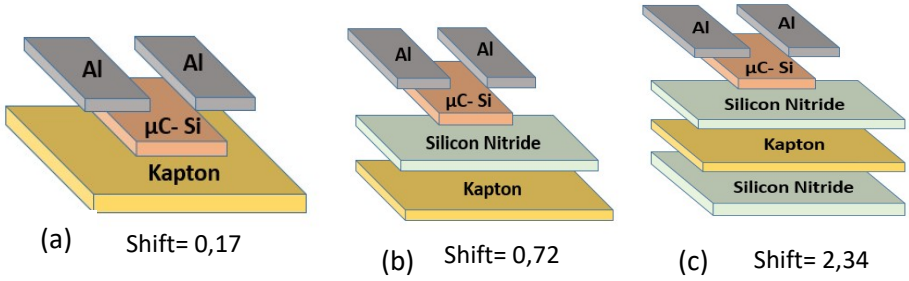

Figure 2-17. Structures and values of resistances shiftiness.

The shiftiness produced on the samples with silicon nitride layer is higher. This fact can be explained by the very high Elastic Modulus of Silicon Nitride, which is around 183 GPa. This hardness induces some cracks during deformation, these cracks are expanded to the rest of the structure making that the value of the resistance changes after deformations. SiNx layer cannot then be a good option to balance the induced stress after µc-Si deposition, because SiNx layer produces a strong shift of the resistance value after deformations and worse the reliability of the devices.

6.2.2 Effect of reducing the area of µc-Si deposition

One other method developed to reduce the induced stress was to reduce the deposition area of µc-Si. Considering Stoney's theory for a substrate conforming to the film, we decided to hold the substrate with a rigid frame during the deposition process.

A shadow mask has been designed with ANSYS software. During the design, attention was paid to the phenomenon of the step coverage in CVD, the dimension of the squares of these mask are bigger than the area of µc-Si that will be used for the devices.

Figure 2-18 shows the dimensions of the squares are 3 x 4cm². The maximum area of µC-Si used for transmission line measurement (TLM) mask is 1 x 1 cm² and the minimum value is 1 x 0.0125cm². (Those masks will be further fully described).

Figure 2-18(b) shows the theoretical effect of the step coverage of CVD films and Figure 2-18(c) shows an example of this effect in one of our sample using the designed shadow mask.

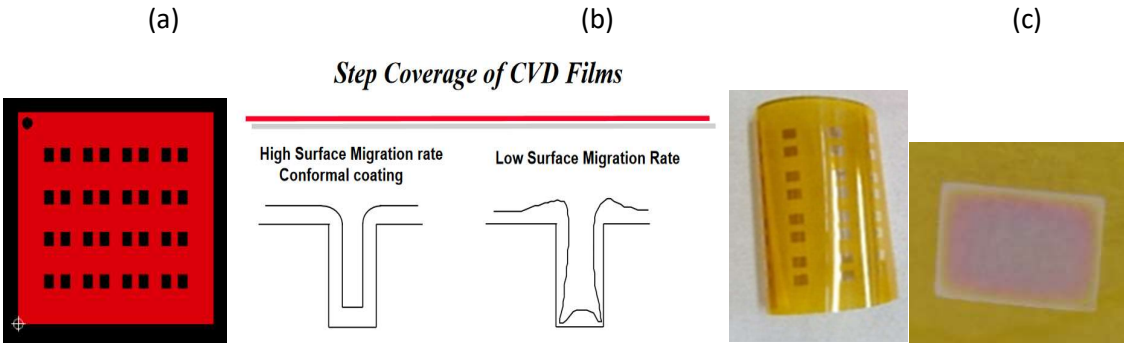

Figure 2-18. (a) Shadow mask design to reduce the area of µC-Si deposition for TLM mask. (b) Effect step coverage of CVD films. (c) Sample using the shadow mask for µc-Si deposition and the effect of the step coverage.

6.2.3 Dimensional stability of Kapton---- shrinking

Despite the use of all the techniques commented previously, the induced curvature has been reduced but it still remains a little present.

In the 25 µm Dupont Kapton polyimide datasheet, it is written that the substrate suffers for a shrinking during and after the first exposure to high temperature. This effect is permanent and, once the substrate has been exposed, Kapton follows the normal values of the linear expansion thermal coefficient.

For this reason, to set the substrate to its stable form, a pre-bake process is realized after the cleaning procedure. The substrate is baked in the hot plate during 30 min at 150°C. This bake is also important to remove solvents residuals. After the prebake process, the substrate is ready for fabrication steps.

Figure 2-19(a) shows the induced curvature of Kapton substrate using a shadow mask during µc-Si deposition and Figure 2-19(b) shows the effect on the sample when the pre-bake process is done before µc-Si.

Hence, by making a combination between this pre-bake and the shadow mask, the residual stress is strongly reduced. This dimensional stability of the substrate is important to avoid alignment problems or delamination of the layers, thus improving the electrical and mechanical performance of the devices.

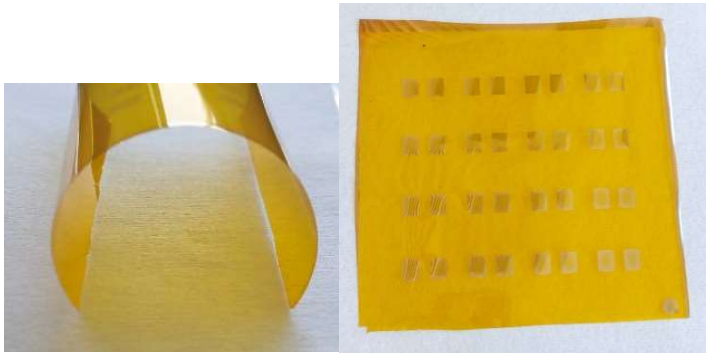

(a) (b)

Figure 2-19. Effect curvature induced (a) after µc-Si using a shadow mask (b) pre-bake substrate before µc-Si using a shadow mask.

7 Conclusion

In this chapter, we have presented the different deposition techniques available in the laboratory to develop µc-Si, as well as some examples of this material used on flexible substrate. In addition, the main disadvantages of working with a flexible substrate and some solutions to minimize the problems associated with this thin thickness were discussed.

8 Bibliography

[1] K. Kandoussi, “Procédé de fabrication à T<200°C de transistors en couches minces de silicium microcristallin déposé par PECVD en mélange SiH_4-H_2-Ar.,” thesis, Rennes 1, 2007.

[2] A. Shah *et al.*, “Intrinsic microcrystalline silicon (μc-Si:H) deposited by VHF-GD (very high frequency-glow discharge): a new material for photovoltaics and optoelectronics,” *Mater. Sci. Eng. B*, vol. 69–70, pp. 219–226, Jan. 2000.

[3] W. J. Soppe, C. Devilee, M. Geusebroek, J. Löffler, and H.-J. Muffler, “The effect of argon dilution on deposition of microcrystalline silicon by microwave plasma enhanced chemical vapor deposition,” *Thin Solid Films*, vol. 515, no. 19, pp. 7490–7494, Jul. 2007.

[4] “Inductively Coupled Plasma - Chemical Vapor Deposition (ICPCVD),” *Corial*, 20-Dec-2016.

[5] S. Janfaoui, “Électronique CMOS en silicium microcristallin sur substrat flexible transparent,” thesis, Rennes 1, 2012.

[6] Y. Kervran, “Cartographie d’un champ de pression induit par l’occlusion dentaire.”, thesis.

[7] S. Middelhoek and S. A. Audet, “Silicon Sensors,” *Infoscience*, 1989. [Online]. Available: https://infoscience.epfl.ch/record/24206. [Accessed: 25-Aug-2019].

[8] A. Mézin, “Coating internal stress measurement through the curvature method: A geometry-based criterion delimiting the relevance of Stoney’s formula,” *Surf. Coat. Technol. - SURF COAT TECH*, vol. 200, pp. 5259–5267, May 2006.

[9] H. Gleskova, I.-C. Cheng, S. Wagner, and Z. Suo, “Mechanical Theory of the Film-on-Substrate-Foil Structure: Curvature and Overlay Alignment in Amorphous Silicon Thin-Film Devices Fabricated on Free-Standing Foil Substrates,” in *Flexible Electronics: Materials and Applications*, W. S. Wong and A. Salleo, Eds. Boston, MA: Springer US, , pp. 29–51, 2009

[10] I.-C. Cheng, A. Kattamis, K. Long, J. C. Sturm, and S. Wagner, “Stress control for overlay registration in a-Si:H TFTs on flexible organic-polymer-foil substrates,” *J. Soc. Inf. Disp.*, vol. 13, no. 7, pp. 563–568, 2005.

[11] K.-B. Kim, Y. Oh, and Y.-H. Song, “Simulation of residual stress and its impact on a poly-silicon channel for three-dimensional, stacked, vertical-NAND flash memories,” *J. Korean Phys. Soc.*, vol. 70, pp. 1041–1048, Jun. 2017.

[12] “Epitaxy (epitaxial growth, 에 피 택 셜 성 장) IT 툞 아 보 기 .” [Online]. Available: https://depletionregion.tistory.com/116. [Accessed: 25-Jun-2019].

[13] F. Toth, F. G. Rammerstorfer, M. J. Cordill, and F. D. Fischer, “Detailed modelling of delamination buckling of thin films under global tension,” *Acta Mater.*, vol. 61, no. 7, pp. 2425–2433, Apr. 2013.

[14] W.-Y. Chang, T.-H. Fang, and Y.-C. Lin, “Physical characteristics of polyimide films for flexible sensors,” *Appl. Phys. A*, vol. 92, no. 3, p. 693, May 2008.

[15] K. Belarbi *et al.*, “Stability of Microcrystalline Silicon TFTs,” *ECS Trans.*, vol. 16, no. 9, pp. 121–129, Mar. 2008.

[16] K. Kandoussi, A. Gaillard, C. Simon, N. Coulon, T. Pier, and T. Mohammed-Brahim, “Improved microcrystalline silicon TFTs,” *J. Non-Cryst. Solids*, vol. 352, no. 9, pp. 1728–1731, Jun. 2006.

CHAPTER 3 - Transmission Line Measurements (TLM)

1. Introduction

The aim of this chapter is to investigate the piezoresistive properties of microcrystalline silicon and its sensitivity to different mechanical deformations.

First, we will introduce the method used to characterize this material. It is based on the principle of Transmission Line Measurements (TLM). In this section, the parameters extracted with this method will be theoretically explained with special attention to the specific contact resistivity. This parameter has become very important in recent times due to the sharp reduction in the size of devices, where the value of parasitic resistances must be significantly low.

Following, the mask used and the fabrication process of these devices will also be described.

The deposition of μc-Si was carried out using two different techniques: PECVD (Plasma-enhanced chemical vapour deposition) and ICPCVD (Inductively Coupled Plasma Chemical Vapour Deposition). According to both techniques, the results obtained were divided in two parts. The first consists in studying the classic parameters of the TLM structure such as the specific contact resistivity (ρ_c), the sheet resistance (R_{SH}) or a mapping of uniformity of the resistivity. The second part presents the sensitivity of the microcrystalline silicon as a deformation sensor, when this material is subjected to different radii of curvature.

2. Transmission Line measurement (TLM)

The Transmission Line Measurement or TLM method is one of the most common approaches to calculate the specific contact resistance, the transfer length and the sheet resistance (R_{SH}) of the semiconductor.

This method was introduced by Shockley in 1964 [1] and, as shown in Figure 3.1, consists of measuring parallel resistances separated by contacts with variable spacing or length (d1, d2, d3, d4). The values of the resistances obtained are plotted in a linear regression, from which all the parameters mentioned above can be extracted.

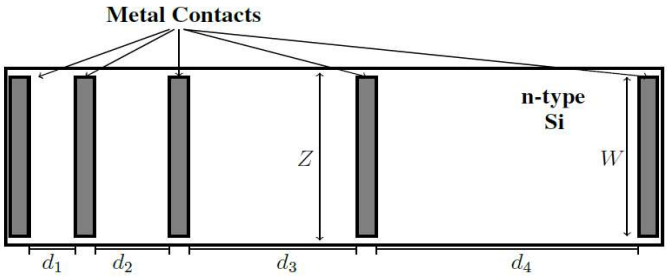

Figure 3.1. Top view of Transmission Line structure.

2.1 Parameters extraction

Figure 3.2 shows a scheme of a resistance measurement and a horizontal view of the TLM structure.

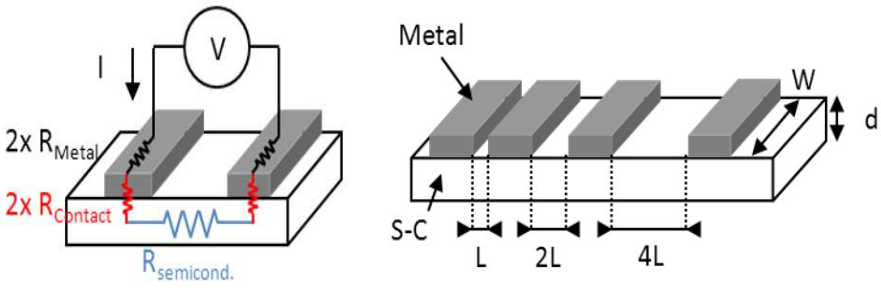

Figure 3.2. Typical trace resulting from a TLM test [2].

I-V measurements were realized between each adjacent contact, and they are plotted as a function of the total resistance (R_{Tot}) and the contact spacing (L). The total resistance can then be expressed by the formula (3.1):

$$R_{Tot} = R_{SH} + 2R_{Contact} + R_{metal} \quad (3.1)$$

Where R_{SH} corresponds to the semiconductor resistance or sheet resistance and can be obtained from the slope of the curve. R_{metal}, is the metal resistance and generally can be considered as

negligible. $R_{contact}$, is the contact resistance in the metal-semiconductor junction. This parameter have a direct impact in the device's performance, and for this reason, must have a small value. From the contact resistance, the contact resistivity can be extracted, however this parameter depends on the contact area size. For that reason, to make a comparison independent of its size, in the literature [3], the contact resistance is employed and can be obtained directly through TLM model.

Firstly, to better understand what happens in the junction between the metal-semiconductor and how this affects the devices performance, it is necessary to understand how the current flows through the interfaces.

The contact between metal and semiconductor can be classified mainly in ohmic contact or Schottky barrier contact.

- Schottky contacts (also called barrier or rectifiers) have important applications such as Schottky diodes or MESFET transistors. The main characteristic of the rectifier contacts is that they allow working at high speeds, and therefore, they are widely used in high frequency applications such as switches. They are so used as power rectifier diodes since they easily dissipate heat through the metallic contact.

- The ohmic contacts refer to the contact in which there is no rectifying effect. Basically, an ohmic contact is a low resistance joint that provides conduction in both directions between the metal and the semiconductor. Ideally, the current through the ohmic contact is a linear function of the applied potential. The quality of an ohmic contact is evaluated by determining specific contact resistance that will be defined later.

Theoretically, to achieve an ohmic contact between a metal and N-type semiconductor, the condition to be fulfilled is that the working function of the metal is less than that of the semiconductor (or higher if it is a P-type semiconductor). Unfortunately, there are very few combinations able to achieve this requirement. Therefore, the most common alternative is to use heavily doped semiconductor. However, depending on the semiconductor doping level, there are three main conduction mechanisms between metal and semiconductor, shown in Figure 3.3. The thermionic emission presents a low doping impurities concentration and its I-V curve behaves such a Schottky barrier (a); the thermionic-field emission has a medium doping level of impurities (b) and the field emission, here the junction metal semiconductor is heavily doped obtaining an ohmic contact as shows the graphic (c).

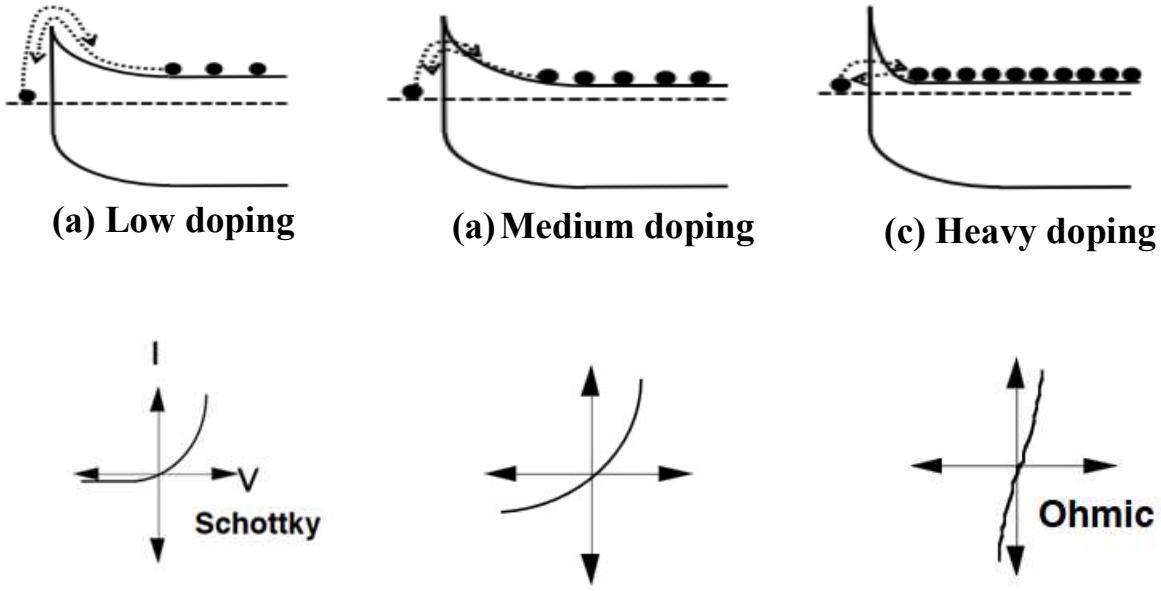

Figure 3.3: Conduction mechanisms for metal/n-type semiconductor contacts as a function of the barrier height and width. (a) Thermionic emission; (b) thermionic-field emission; (c) field emission [3].

2.2 The specific contact resistivity

The specific contact resistivity is used to determine the quality of the metal-semiconductor junction and is a useful parameter to qualify an ohmic contact.

As explained before, an ohmic contact allows that the charge flow easily in both directions between the metal and the semiconductor [4]. In this case, the value of the contact resistance should be negligible and the I-V curve obtained should be linear or quasi-linear.

There are other methods to measure the specific contact resistivity (ρ_c) such as Cross Bridge Kevin Resistance (CBKR) [5]. However, our work focuses on the transmission line measurement method (TLM).

This method allows to calculate the specific contact resistivity (ρ_c) by means of the transfer length (L_T), which is defined as the length at which more than 60% of the current flows through the contacts.

Figure 3.4 shows what occurs really in the electrodes. Here the current density over its conduction area is not uniform and it enters the contact from the top, the bottom and the front. However, to simplify the calculus and because almost all of the current enters through a path under the contact, we only consider that the current density enters from the bottom.

According to the level of the specific contact resistivity, two different cases can be described. For very small values of ρ_c, shown figure 3.5 (a), only the edge of the contact area is used in the conduction t, and for high values of ρ_c, as shown figure 3.5 (b), a large area of the contact is used for the conduction.

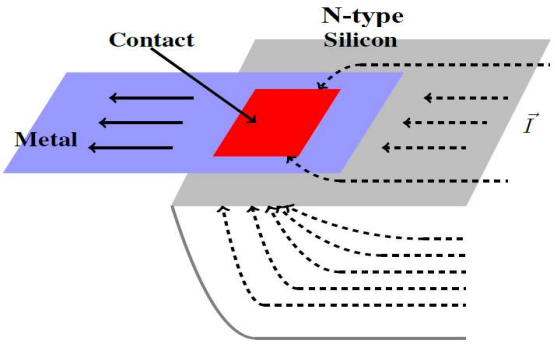

Figure 3.4. Current flows [3].

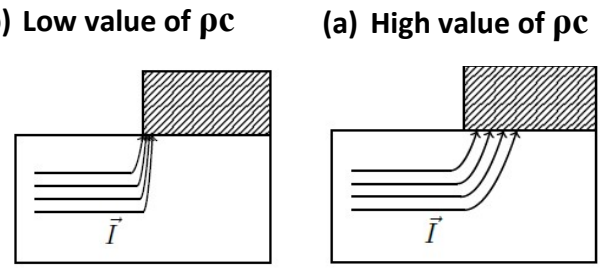

Figure 3.5. Current lines in function of the ρ_c electrodes [3].

Formula 3.2 (a) or (b) is used to calculate the value of the specific contact resistance ρ_c, where R_{SH} is the sheet resistance of the underlying layer, R_C corresponds to the contact resistance and W is the width. The value of the transfer length, L_T can be extracted from the graph in Figure 3.6. It corresponds to the half value of the x-axis interception between the total resistance (R_T) and the spacing distances (d).

$$L_T=\sqrt{\frac{\rho_C}{R_{SH}}} \qquad (3.2\ a)$$

$$L_T=\frac{\rho_C}{R_C\ x\ W} \qquad (3.2\ b)$$

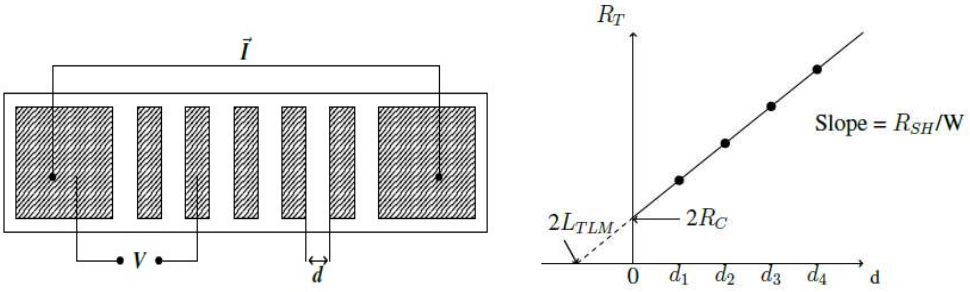

Figure 3.6. Graphic used to extract TLM parameters [3].

Moreover in our case, TLM devices are used to evaluate the uniformity of the resistivity at different points of the sample. In the second part of this chapter, this structure is used to evaluate the sensibility of µc-Si to different deformations.

3. Mask design and fabrication process

The designed mask used to perform TLM devices is shown in Figure 3.7. Its surface area is 5x5cm^2, there are four columns with four different width values (W = 125, 1000, 500, 250 µm). Each line presents the same dimensions and each TLM structure is formed by 6 resistances with different lengths (L= 5, 10, 20, 40, 80, 160 µm). The design contains 24 resistances with different dimensions.

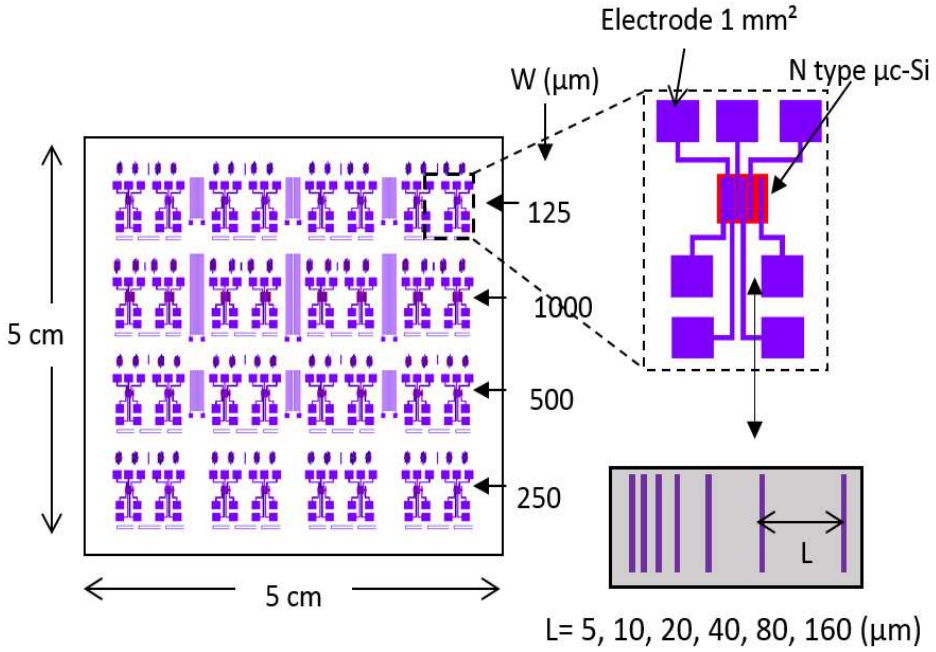

Figure 3.7. TLM design used in our devices [2].

Next, the fabrication process used in TLM devices is commented. Taking into account the technological barriers encountered with a flexible thin substrate and the solutions used (see Chapter 2) only the steps for the production process are described below.

4. TLM Device Manufacturing Process

Here is described the fabrication process of TLM devices. The first step is to cut the Kapton substrate foil in a 6x6cm^2 square. The substrate's trimmed area is 1cm^2 bigger than the mask' size (5x5cm^2) to help us in the manipulation process. The next steps in the fabrication process are described below and are represented on Figure 3.8.

1) Substrate cleaning and post treatment, Figure 3.8 (a):

   Kapton substrate is cleaned with acetone and alcohol to remove small particles pollution, this process is repeated as often as necessary. Once the substrate is dry, it is necessary to bake it in the hot plate during 30min at 150°C. As explained in Chapter 2, this step is necessary due to Kapton shrink after the first deposition at high temperature.

2) Silicon nitride (50nm) as an encapsulation layer Figure 3.8 (b):

   This layer was only used in the first devices manufactured, as written in chapter 2. Indeed, its effect on the mechanical behaviour of the structure leads to the creation of cracks. However, the influence of the nitride layer on the electrical behaviour of the device will be analysed in this chapter. Its removal will help to improve the performance and flexibility of our sensors.

3) µc-Si (100nm) as sensing material Figure 3.8 (c1):

   This material is deposited by two different techniques, PECVD and ICPCVD. The µc-Si areas of the devices are defined by photolithography and etching.

   Photolithography: this step consists in spin coating a thin layer of photoresist S1818 over µc-Si layer. After that, it is baked at 100°C to dry the photoresist. A mask is used to flash the sample that will define the device's pattern. The photoresist is then developed to verify if the shape is well defined.

   Etching: in the case of µc-Si, etching is made by using a Reactive Ion Etching (RIE) reactor. The gas used to realize the etching is SF_6, Figure 3.8 (c2).

4) Electrodes, Figure 3.8 (d1):

   Aluminium is the material selected to fabricate the electrodes. It is deposited though evaporation by Joule effect and the thickness of the layer is 150 nm. The photolithography step is then realized.

   For aluminium, a wet etching consisting in immersing the sample into solution of phosphoric acid (H_3PO_4) at a temperature of 50°C, Figure 3.8(d2) is achieved.

5) Annealing:

   This is realized during 2 hour under nitrogen at 180°C. The annealing step is necessary to improve the junction between the metal and the semiconductor enhancing the bonding between the two materials.

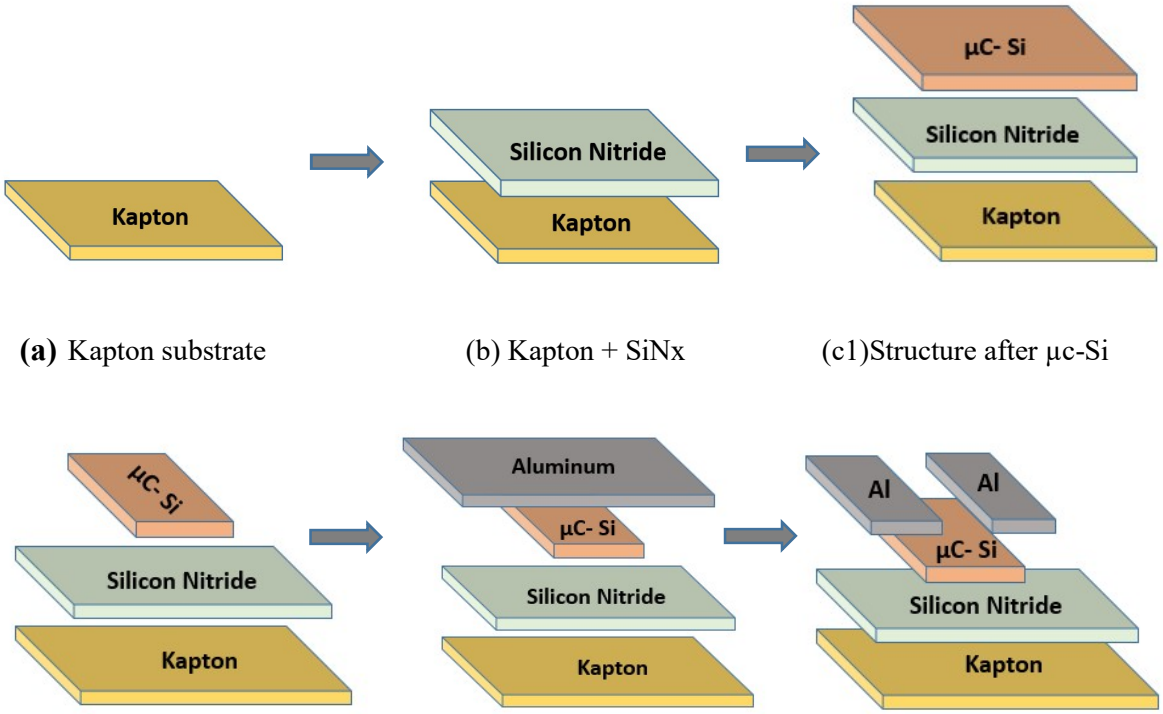

(a) Kapton substrate (b) Kapton + SiNx (c1)Structure after µc-Si

(c2) Structure (c1) after etching (d1) Aluminium deposition (d2) Final structure

Figure 3.8. Fabrication process in TLM devices.

5. Raman spectroscopy

In order to compare the quality of microcrystalline silicon deposited by two different methods (PECVD, ICPCVD), Raman spectroscopy can be performed to analyse this material and determine its crystallinity [6].

As described in Chapter 1, microcrystalline silicon is a mixture of crystalline zones separated by grain boundaries (amorphous zone). By using Raman spectrometry, it is possible to know the crystallization level also called crystalline fraction ($f_{C\%}$)

The spectrum allows us to obtain more information of the link between molecules observed. The spectrum is formed by the convolution of 3 Gaussian contributions as shown on figure 3.9:

- Amorphous phase of silicon (C_{am}): the curve is centered at 480 cm^{-1}.
- It exists an intermediate phase (C_{int}) that corresponds to a defective crystalline phase with a center at about 510 cm^{-1}. It highlights the presence of joints of crystalline grains and crystallites of dimensions less than ten nanometers [7].

- Crystalline phase of silicon (C_{mono}): A narrow Gaussian centered at about 520 cm-1, corresponding to the crystalline phase of the material. The position and width of the Gaussian depends on the grain size and stress in the material. [8] [9] [10].

Once this deconvolution has been achieved, the calculation of the area under each curve allows to calculate the crystalline fraction using the formula 3.3.

$$(f_C\ \%) = \frac{C_{mono} + C_{int}}{C_{mono} + C_{int} + C_{am}} \tag{3.3}$$

where Ic, Ii and Ia are respectively the integrals of the Raman intensities centered in the vicinity of the 520, 510 and 480 cm- lines.

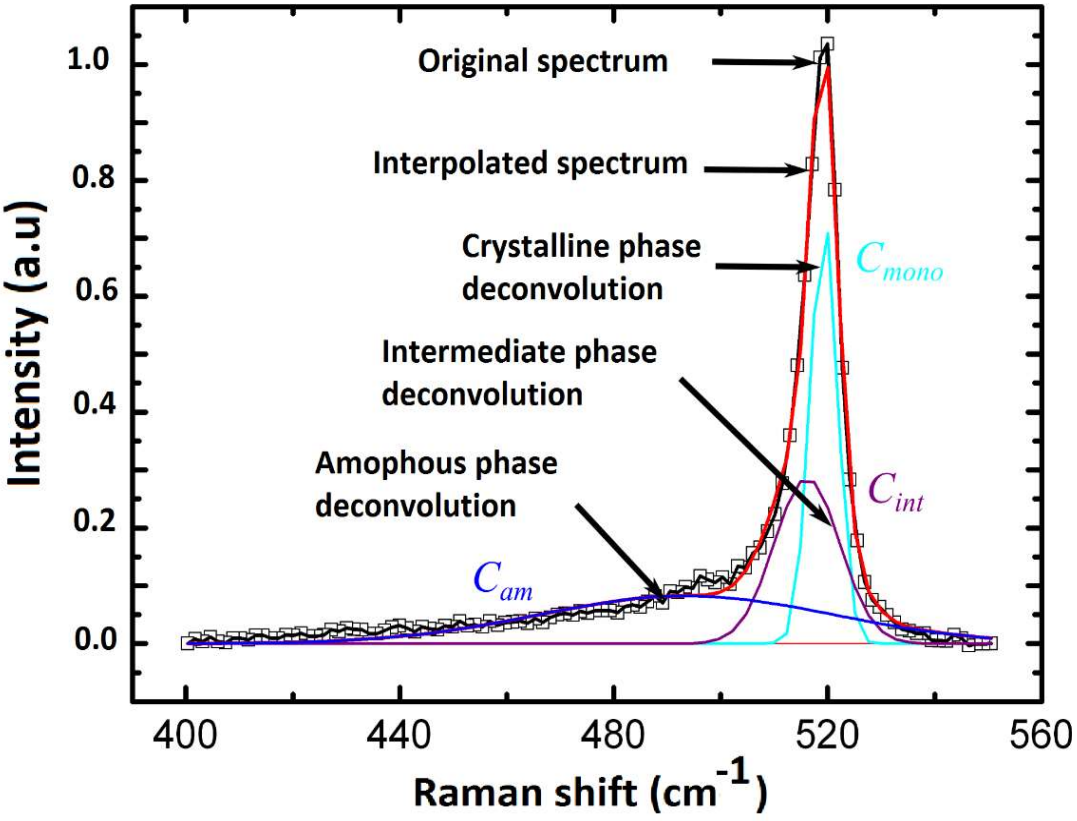

Figure 3.9. Raman spectrum deconvolution for three curves. [11]

6. Results obtained with TLM technology

TLM structures are used for different objectives, so the results will be separated in two sections.

Firstly, the results obtained with both deposition techniques (PECVD, ICPCVD) will be shown. The parameters extracted such as the specific contact resistivity (ρ_c), the sheet resistance (R_{SH}) and a mapping of resistivity uniformity are presented. The calculations are based on the theory shown in section 2 of this chapter.

Secondly, these structures are used to calculate the sensitivity of N-type microcrystalline versus different deformations. TLM design is not usually dedicated to this goal, but we will use them to study the piezoresistive properties of the sensing material.

6.1 TLM parameters for N-type µc-Si deposited by PECVD technique

This is the historical technique used in the laboratory to deposit N-type microcrystalline silicon at low temperature. The deposition parameters of this technique has been improved during K. Kandousi's thesis [12] and are shown in Table 3.1.

Temperature	**Power**	**Pressure**	**Gases**	
T=165ºC	15 W	0.9 mbar	Ar = 75 sccm	SiH_4 = 1.5 sccm
			H_2 = 75 sccm	AsH_3= 10 sccm

Table 3.1. N-type doped µc-Si conditions for the deposition in PECVD machine.

In order to learn to work with 25 µm thick flexible substrate and to compare the results with previously ones obtained in the IETR [2], with substrates thickness of 50 µm, three different structures were tested.

I. Kapton (50µm) + SiNx (50 nm) + N-type µc-Si (100nm)
II. Kapton (25µm) + SiNx (50 nm) + N-type µc-Si (100nm)
III. Kapton (25µm) + N-type µc-Si (100nm)

The thickness of the global structure is reduced gradually, first the thickness of the substrate from 50 µm (I) to 25 µm (II) and then silicon nitride layer is eliminated (II to III).The motivation to reduce the thickness of the global structure is that the main objective of the thesis is to create a sensor that can be used to detect weak and fast deformations. Table 3.2 shows the values obtained with TLM for ρ_c and R_{SH}, L_T, R_c.

	(I)	(II)	(III)
	Kapton (50µm)+SiNx (50nm)+µC-Si (100nm)	**Kapton (25µm)+SiNx (50nm)+µC-Si (100nm)**	**Kapton (25µm)+ µC-Si (100nm)**
R_{SH} (kΩ)	26 kΩ	13 kΩ	16 kΩ
R_c(Ω)	94 Ω	59 Ω	32 Ω
L_T (µm)	3.6 µm	4.5 µm	2 µm
ρ_c (Ωxcm^2)	3.4 x 10^{-3}	2.6 x 10^{-3}	6.4 x 10^{-4}

Table 3.2. Values obtained on TLM devices deposited by PECVD technique.

By observing the values of Table 3.2, we realized that when the global structure is reduced, the values of the contact resistance (Rc) and the sheet resistance (R_{SH}) are also reduced. To explain this fact, we decided to compare first the influence of the Kapton thickness (50µm versus 25µm), and then the effect of the silicon nitride layer.

1) Kapton substrate thickness effect:

We can compare the structures I) and II) where the only difference is the thickness of the substrate. Our first option was to investigate if the topography of the substrate has some influence on the conductivity.

Other researchers have investigated the effect of substrate material during PECVD deposition and the possible alteration during the film growth due to micro topographical features .[13].

W.Y. Chang [14] has investigated the physical characteristics of polyimide films for flexible sensor by using AFM measurement in the x-y plane on a surface of 5x5µm^2. He demonstrates that the average surface roughness (Ra), shown on table 3.3 for both thickness are very similar. Therefore it is discarded that the roughness of Kapton's surface have some influence on this. Moreover, in the literature, we can be find other studies that follow our theory comparing the roughness of different substrates before and after deposition. For example, Amirzada concludes that the nature of the substrate does not affect the final value of the surface roughness. [15]

Thickness (µm)	Ra (nm)
25	10.3
50	13.8

Table 3.3. Topography study Kapton film.

By observing the R_{SH} and R_C values obtained for the structures I) and II), when the substrate is reduced from 50µm to 25µm, these values are also reduced (Table 3.3). This may be due to the fact that the 25 µm thick substrate is more in contact with the electrodes during the plasma creation during µc-Si deposition. By reducing the thickness of the substrate, conductivity is improved.

2) Removal of the silicon nitride layer:

The Young's modulus value for silicon nitride layer is around 183 GPa [16]. For µc-Si, it is about 80 GPa [17]. This value makes that the hardness of SiNx is bigger than µc-Si. Cracks appear more often in this case, and that can increase the value of the contact resistance (Rc), as shown in Table 3.3. Removing the nitride layer results in a decrease in contact resistance (Rc), transfer length (T_L) and conductivity ($\rho_{c,}$). By removing the nitride layer, the hardness of the structure is reduced and some problems between the layers such as delamination or stress cracks in the thin film are also reduced. These problems affect the conduction between metal-semiconductor and can degrade contact junction.

Moreover, to analyse the uniformity of the deposition, a mapping of the resistivity in different points of the sample was achieved. To perform this, 8 resistances with L= 40µm and W= 1000µm have been measured on each layer. The resistivity have been extracted from the following formula 3.4:

$$R = \frac{\rho}{W x\, t} L \Rightarrow \rho = \frac{Rx\, W x\, t}{L} \quad (\Omega xcm) \tag{3.4}$$

Table 3.4 shows the results and Figure 3.11 the values obtained for the resistivity and its corresponding standard deviation.

	Mapping resistivity		
	Kapton (50µm)+SiNx (50nm)+µC-Si (100nm)	**Kapton (25µm)+SiNx (50nm)+µC-Si (100nm)**	**Kapton (25µm)+ µC-Si (100nm)**
ρ (Ωxcm)	0.132± 0.0021	0.137 ± 0.0112	0.139 ± 0.029

Table 3.4. Mapping of resistivity and it standard deviation using PECVD deposition.

Analyzing the values in Figure 3.10, uniformity decreases as a function of the thickness of the overall structure. Indeed, during the µc-Si deposition process, substrates with lower thickness show a higher induced curvature after the deposition process. This curve generates cracks in

different zones, which modify the resistivity value and increase the non-uniformity of the sample, generating larger values in the standard deviation.

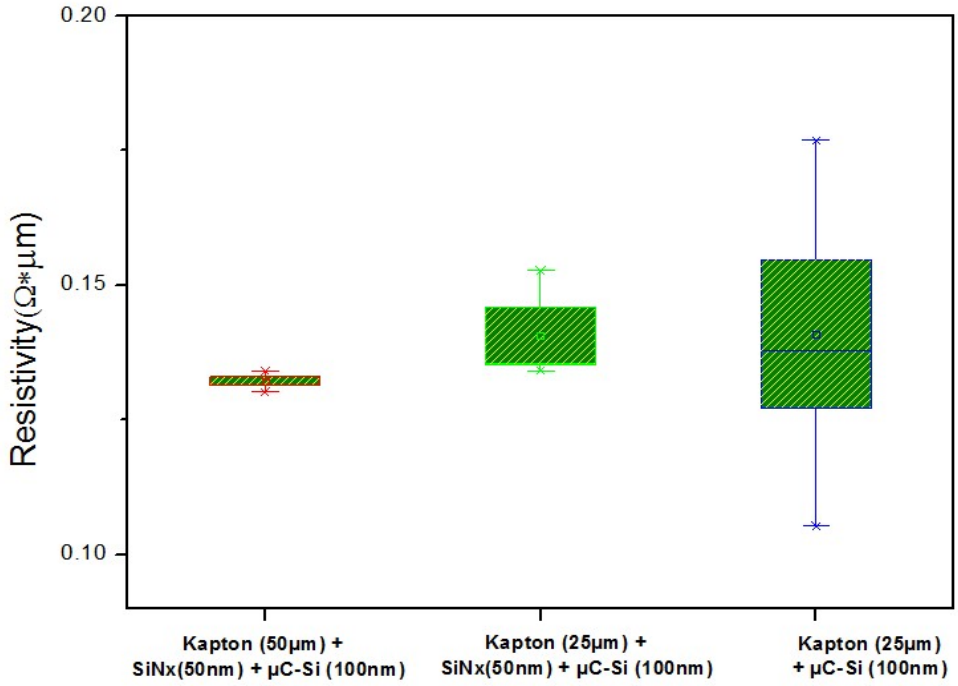

Figure 3.10. Representation of the resistivity mapping and its standard deviation on PECVD deposition.

6.2 TLM parameters for N-type µc-Si deposited by ICPCVD technique

As ICPCVD is a new technique in the laboratory, it is necessary to study which parameters are the most appropriate to develop our sensors. To do that, several conditions, summarized in Table 3.5, are tested.

SAMPLE 1	**SAMPLE 2**	**SAMPLE 3**	**SAMPLE 4**	**SAMPLE 5**
20 PH_3 RF 0W LF 600W	20 PH_3 RF 0W LF pulse 600-900 W	20 PH_3 RF 40 W LF 600W	20 PH_3 RF pulse 0-40W LF 600W	20 AsH_3 RF pulse 0-40W LF 600W
SAMPLE 6	**SAMPLE 7**	**SAMPLE 8**	**SAMPLE 9**	**SAMPLE 10**
20 AsH_3 RF 0 W LF 600W	5 PH_3 RF 0 W LF 600W	10 PH_3 RF 0W LF 600W	10 PH_3 RF pulse 0-40W LF 600W	10 AsH_3 RF pulse 0-40W LF 600W

Table 3.5. ICPCVD conditions.

In the same way that for PECVD, the calculus of the specific contact resistivity (ρ_c), sheet resistance (R_{SH}), the transfer length (L_T) and the contact resistance (R_c) have been done with the method described in section 2. The values obtained are presented in Table 3.6.

	S1	**S2**	**S3**	**S4**	**S5**
R_{SH}(kΩ)	16 kΩ	15 kΩ	15 kΩ	5.8 kΩ	27 kΩ
R_c(Ω)	133 Ω	15 Ω	86 Ω	29 Ω	45Ω
R_c/R_{SH} (Ω %)	0.83	0.1	0.57	0.5	0.167
L_T(µm)	8 µm	0.9 µm	6 µm	5 µm	1.8 µm
ρ_c (Ωxcm^2)	1.07×10^{-2}	1.4×10^{-4}	5.2×10^{-3}	1.5×10^{-3}	8.1×10^{-4}

	S6	**S7**	**S8**	**S9**	**S10**
R_{SH}(kΩ)	26 kΩ	67 kΩ	18 kΩ	8 kΩ	23 kΩ
R_c(Ω)	74Ω	1.7 kΩ	51 Ω	25 Ω	356 Ω
R_c/R_{SH} (Ω %)	0.285	2.54	0.283	0.313	1.55
L_T(µm)	3 µm	3.4 µm	2.5 µm	4.3 µm	8.2 µm
ρ_c (Ωxcm^2)	2.2×10^{-3}	5.8×10^{-2}	1.3×10^{-3}	1.1×10^{-3}	2.8×10^{-2}

Table 3.6. Values obtained on TLM devices deposited by ICPCVD technique.

In order to organize these results, it was decided to represent them in the Figure 3.11, in which appear the values of the resistivity of specific contact as a function of the transfer length (since this parameter defines the length from which more than 60% of the current enters in the contacts). The ratios R_C/R_{SH} are also presented on this figure, and represent the percentage of the contact resistance over the sheet resistance.

Here it can be observed that as the L_T value increases; the ratios R_C/R_{SH} also increase. This is logical, because, as it was explained in previous sections, for small values of the contact resistivity ρ_c, that the current enters quickly in the contact, leading to a small value of the R_C/R_{SH}. Therefore these two parameters increase in proportion with L_T value.

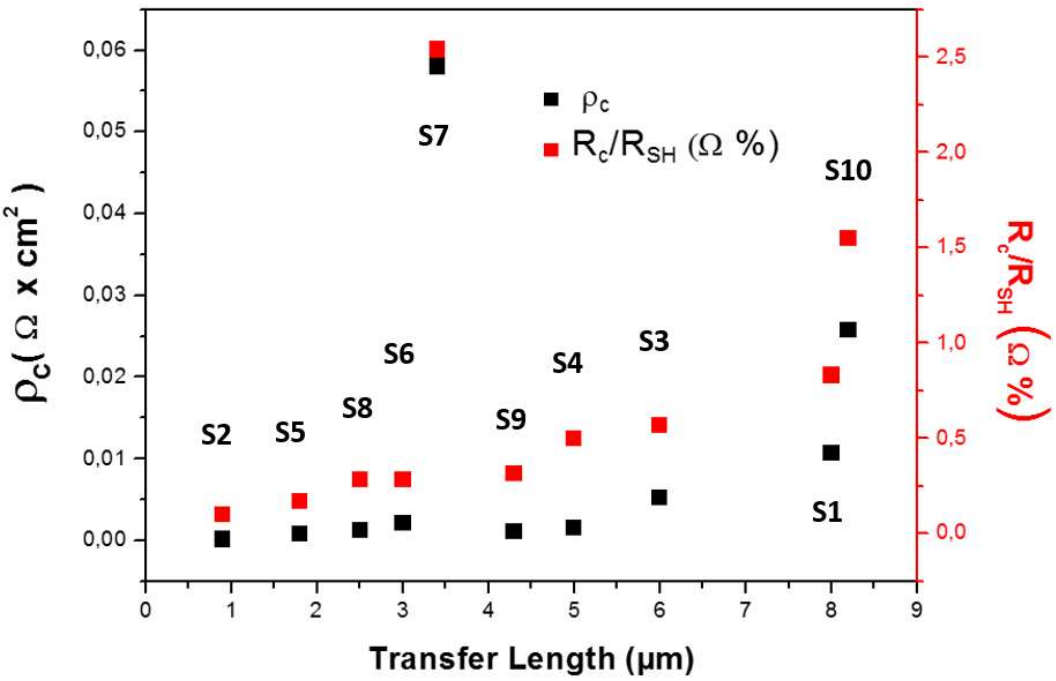

Figure 3.11. ICPCVD results of it specific contact resistance (ρ_C) and R_C/R_{SH} in function of its transfer length (L_T).

Now some relevant cases can be commented:

- S2 is the sample with the lowest values, this is normal because LF power pulses are used, and this effect should increase the crystallinity and therefore the conductivity making smaller the values for L_T, ρ_C and R_C/R_{SH}.
- It was also observed that for the same doping gas flow rate (AsH_3 or PH_3), when pulses are applied in RF power (samples 4 versus samples 1 and 3 and sample 5 versus sample 6), the values of the specific contact resistivity are lower, for the samples where RF power pulse is applied. Figure 3.12 shows an example of this. Moreover, to verify if the grain size is bigger when it is applied pulses in the RF power, the crystallinity fraction (f_c%), measured on these samples, was calculated from Raman spectroscopy measurement. Table 3.7 shows the values obtained.

	(S4) 20 PH_3 RF pulse 0-40W	(S3) 20 PH_3 RF 40W	(S1) 20 PH_3 RF 0W
Crystallinity fraction	79.82 %	72.8 %	71.4 %

	(S5) 20 AsH_3 RF pulse 0-40W	(S6) 20 AsH_3 RF 0W
Crystallinity fraction	66.4 %	64.4 %

Table 3.7 Results obtained for the crystallinity fraction (f_c%).

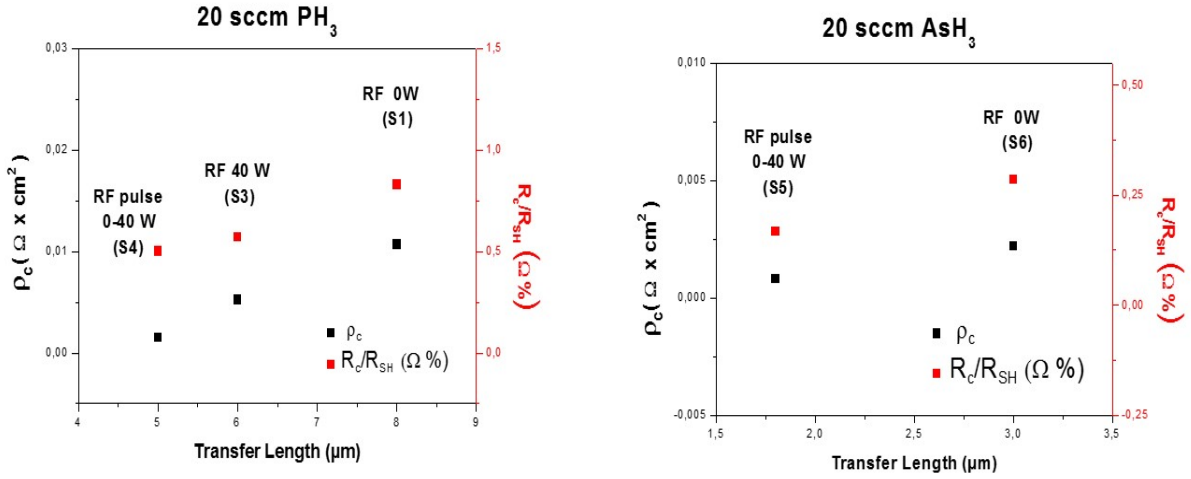

Figure 3.12. Effect on specific contact resistance (ρ_C) and Rc/R_{SH} when it is applied pulses in RF power.

As demonstrated for the samples deposited by PECVD technique, when the thickness of the substrate is reduced, the standard deviation of the results obtained increases. However, to improve our skills in the manipulation of thin substrates that will be used in the devices for dynamic measurement in Chapter 4, all the samples were performed with low thickness substrate.

Table 3.8 shows the values obtained for the resistivity mapping for all the samples. Figure 3.13 shows these values sorted in increasing order according to their resistivity.

	Mapping resistivity				
	S1	**S2**	**S3**	**S4**	**S5**
ρ (Ωxcm)	0.165±0.0228	0.154 ± 0.0153	0.143 ± 0.0538	0.108± 0.0533	0.289 ± 0.0238

	S6	**S7**	**S8**	**S9**	**S10**
ρ (Ωxcm)	0.273 ± 0.0413	0.668 ±0.0447	0.170 ±0.0151	0.083 ±0.008	0.226 ±0.0826

Table 3.8. Mapping of resistivity and it standard deviation using ICPCVD deposition.

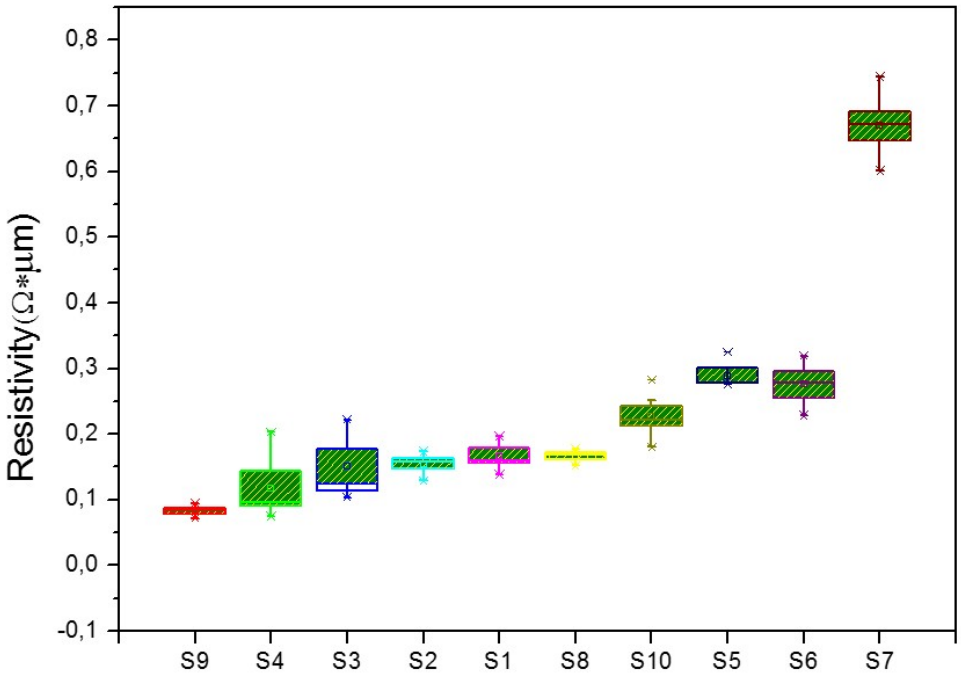

Figure 3.13. Representation of the resistivity mapping and its standard deviation on ICPCVD deposition.

7. Study of the sensitivity of µc-Si under different strain

7.1 Strain calculation

To investigate the sensitivity of µc-Si, the structure is submitted to different bending radius of curvature R and the electrical change of the resistance is measured. As was commented in Chapter 2, the parameter used to measure it is well-known as Gauge factor (GF) and is defined in Formula 3.5. Hence, GF in a material depends both on the geometrical change and on the resistivity change.

$$GF = \frac{\frac{\Delta R}{R}}{\varepsilon} \tag{3.5}$$

When the film/substrate structure is bent, the top surface is under tension and the bottom surface is under compression. It exists one part inside the sheet that does not suffer from any strain, this is known as the neutral plane. Figure 3.14 shows the film/substrate structure under bending and the thicknesses are defined such as d_f and d_s and Young's modulus Y_f and Y_s for the film and the substrate.

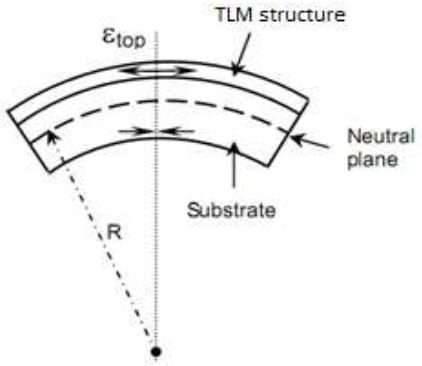

Figure 3.14: Film/substrate structure under a bending radii

In function of the nature of the substrate two different cases are used to calculate the strain in the top surface (ε_{top}):

a) The film is deposited on a stiff substrate:
   If the Young's modulus is the same for film and substrate, the neutral surface corresponds to the middle of the structure and the strain in the top surface is given by formula 3.6:

$$\varepsilon_{top} = \left(\frac{d_f + d_s}{2R} \right) \tag{3.6}$$

b) The film is deposited on a compliant substrate:
   If the Young's modulus of the film is bigger than the Young's modulus of the substrate ($Y_f > Y_s$), the neutral surface shifts from the mid surface toward the film. As a consequence, the strain on the upper surface is given by formula 3.7:

$$\varepsilon_{top} = \left(\frac{d_f + d_s}{2R} \right) \frac{\left(1 + 2\chi\eta + \chi\eta^2\right)}{(1+\eta)(1+\chi\eta)} \text{ Where } \eta = \frac{d_f}{d_s} \text{ and } \chi = \frac{Y_f}{Y_s} \tag{3.7}$$

Figure 3.15 represents the normalized strain in the film (ε_{top}) in function of the thickness d_f/d_s. In this figure, the two cases commented up are compared, a) when film/substrate have the same Young's modulus ($Y_f/Y_s \approx 1$) and, b) when the Young's modulus of the film is higher than the substrate ($Y_f/Y_s \approx 100$).

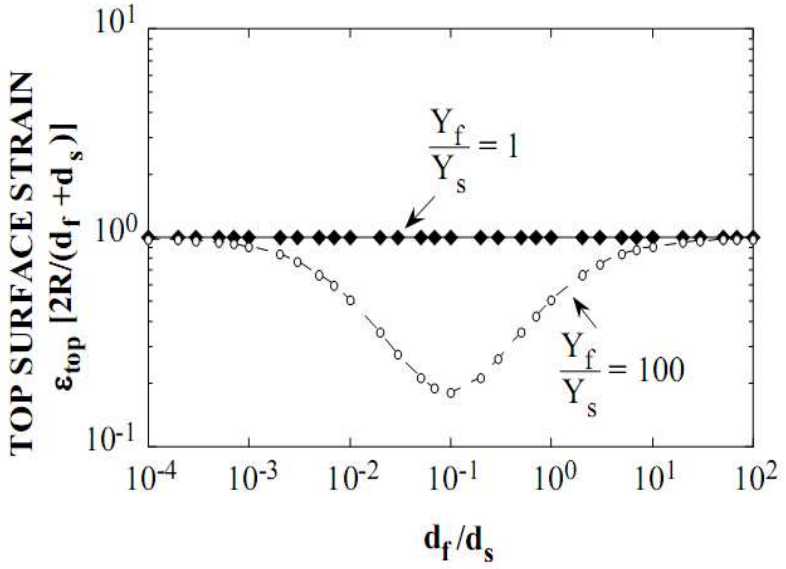

Figure 3.15. Normalize graphic of top surface strain vs the thickness ratio d_f/d_s [18].

In our case, in order to determinate the sensibility of the structure for static deformations, the devices are fixed over half cylinders with different diameters, as shown in Figure 3.16. The I-V measurement is performed at room temperature using the Agilent B1500A software within a voltage range of ±1V.

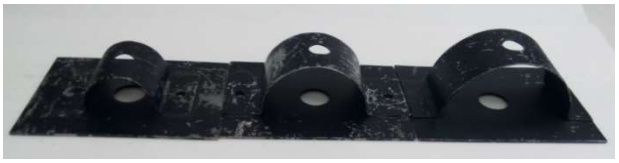

Figure 3.16. Tensile diameter 2 cm, 3 cm and 4 cm.

The characterization process consists in first by measuring the resistance without bending (flat substrate) to obtain the initial value. Then, the sample is fixed onto the highest curvature (lowest diameter, 2cm). This is an important step to obtain a good linearity in the curve. Indeed, when the sample is submitted to the highest bending curvature radius, some cracks can be created, and that increases the value of the resistance. After that, the resistance is measured again without bending (flat state) and this new value is taken as the initial value of the resistance (R_0).
One time that this step is done, the resistance are bent from the higher diameter (5cm) to the lower (2cm) and between each bending, resistors are re-flattened.

7.2 Strain calculation for our structures

In our case, the film is deposited on a compliant substrate, and for this reason, the calculus realized for the applied strain was done with Formula 3.7. Here it is necessary take in account given values such as the thickness (d) and Young's modulus (Y) for each layer. Table 3.9 shows a summary of them.

	Kapton	**SiNx**	**µc-Si**
Young's modulus (Y)	2.5 GPa	183 GPa	80 GPa
Thickness (d)	50 or 25 µm	50 nm	100 nm

Table 3.9 Thickness (d) and young modulus (Y) for the layer used in the structure.

The values obtained for the calculus of each radius of curvature are shown in Table 3.11, the strain ε applied is calculated using a bi-layer simplified model [19]. This model only takes into account the substrate and the stiffest layer, because these will determine the mechanical behaviour of the device. Moreover, this model does not consider the electrodes.
Hence, three different calculations depending on the structure are done for each R value.
As shown in table 3.9, the value of Young's modulus of SiNx is higher than the value of µc-Si. For this reason, for the samples with this layer, the calculi are realized in function of Kapton substrate and of the SiNx layer.

	Top surface strain calculation (ε_{top} %)		
Radii curvature	**Kapton (50µm) + SiNx (50nm) + µC-Si (100nm)**	**Kapton (25µm) + SiNx (50nm) + µC-Si (100nm)**	**Kapton (25µm) + µC-Si (100nm)**
R = 2.5cm	0 ,107	0,0564	0 ,0557
R = 2cm	0,134	0 ,0705	0,0696
R = 1.5cm	0,178	0,0940	0,0928
R = 1cm	0 ,267	0,1410	0,139
R = 0.5cm	0,534	0,282	0,278

Table 3.10. Calculations of the strain suffer on the top of the surface for different structures.

8. Sensitivity N- type µc-Si deposition by PECVD

As we previously studied the deformation detection sensitivity of films elaborated by PECVD [2], our first objective here was to verify that the GF value of µc-Si deposited with this technique presents the same value regardless of the structure.

The values for the strain calculation were extracted from Table 3.10 and the parameters used to deposit µc-Si by PECVD were presented in Section 6.1 above. The three different structures are presented below, and their resistance variation versus the strain calculation is drawn (figures 3.17, 3.18 and 3.19). GF parameter, is calculated from an average slope of each curve.

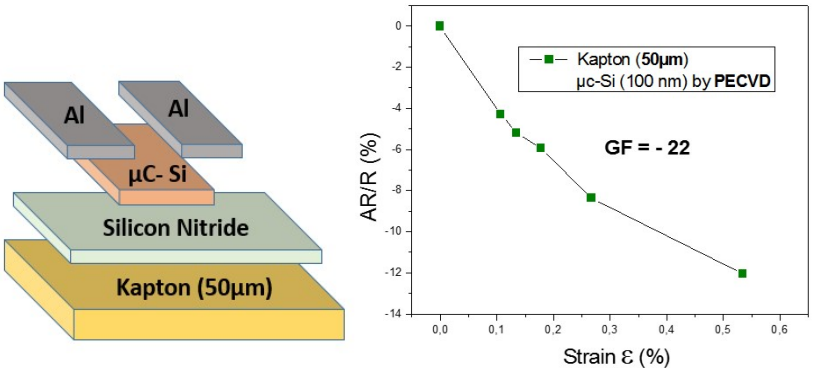

Figure 3.17: GF determination for Kapton (50µm) + SiNx (50 nm) + N-type µc-Si (100nm).

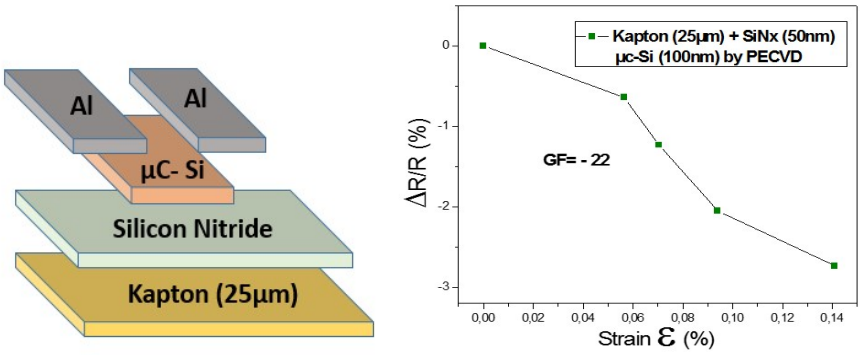

Figure 3.18: GF determination for Kapton (25µm) + SiNx (50 nm) + N-type µc-Si (100nm).

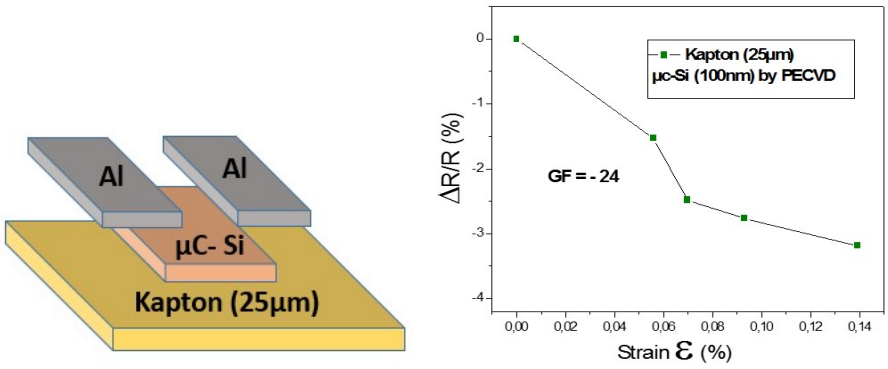

Figure 3.19: GF determination for Kapton (25µm) + N-type µc-Si (100nm).

By observing the results obtained for all these structures, the GF value is practically the same in all cases. However, it is easy to see that the linearity of the slope is worse when the thickness of the substrate is reduced, from 50 µm to 25 µm. This occurs especially during characterization under high strains.

9. Sensitivity N-type µc-Si deposition by ICPCVD

For the ICPCVD technique, the optimal deposition parameters are yet not defined as in the PECVD. Therefore, it is necessary to investigate which could be a good candidate to be used as sensing material under weak deformations. This will be done by analyzing the 10 different conditions showed before in Table 3.6.

To organize the data, the study is divided into different sections and subsections:

a) In function of the doping gas:

Here, a comparison between AsH_3 and PH_3 is done to see if RF and LF power have an effect on sensitivity or if they have different influence on the material sensitivity and they react in the same way.

b) Selected PH3 as doping gases:

It is investigated which plasma parameters can be improved by using PH_3 as doping gas. To do that, the doping flow rate (sccm) of PH_3 has been varied, the effect of applying a pulse on RF or on LF has been studied as well as different constant values of RF power.

One of the biggest problem found during the characterization, beside of the handing of the thin substrate, was the standard deviation of the results, not only in the initial value, but also during the strain deformations.
For all the conditions presented, an average of 5-6 resistances was characterized. For that reason, the graphics are represent with box plot, showing that the standard deviation of some sample is very large, especially for the higher strain.

9.1 Doping gas: AsH_3 or PH_3

When a semiconductor is doped, it means that some impurities are added that will change the electrical, optical and structural properties. Silicon belongs to the group IV and the most common dopant agents for it are the group III such as Boron or Gallium (P-type) or the group V such as Arsine or Phosphine (N-type).
In our case, we decided to focus our depositions on the N-type impurities. We selected AsH_3 and PH_3 as doping agents. Both will be investigated in order to analyze if, by using the same conditions, it exists some change in the sensitivity (GF), or in the resistivity.

This study is divided into several sections such as the comparison of the effect of constant RF and LF power, the influence to add some pulse on RF power or the variation of the doping gas flow rate.

9.1.1 Deposition with constant RF and LF power:

To see the effect of RF and LF power, a doping flow rate of 20sccm for AsH_3 and PH_3 is tested, with constant RF and LF powers (RF=0W and LF=600W). Table 3.11 summarizes the conditions used and the values obtained from the GF.

	RF	LF	DOPING GAS	GF
SAMPLE 1	0 W	600 W	**20 PH_3**	-31
SAMPLE 6			**20 AsH_3**	-34

Table 3.11. Summary conditions and value of the GF obtained for sample 1 and 6.

Moreover, Figure 3.20 presents the box plot of the resistance values under strain. The value of the GF that corresponds to the slope, was extracted from this graphics. GF values are practically the same for both gases. However, the values of the dispersion obtained in the deformations are higher for PH_3.

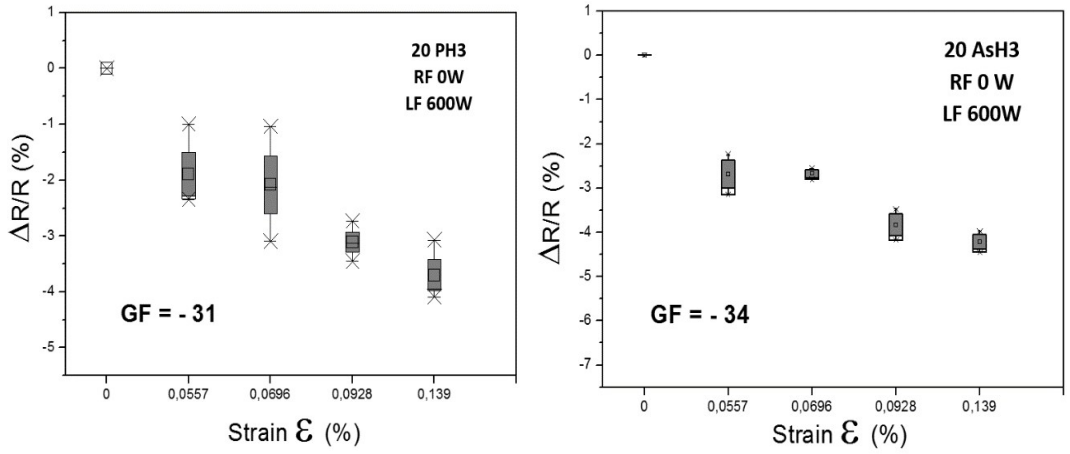

Figure 3.20 Box plot graphic for conditions of Sample 1 and Sample 6.

Figure 3.21 [20] shows the Raman peak in single-crystal silicon when no stress is applied. On this figure is indicated the shift direction produced in the spectrum when it is submitted to tensile or compressive stress. The GF values did not give us a lot of information so Raman measurement in flat state was performed for both doping gases, Figure 3.22.

Here, it was observed that for the sample 6 which was doped with AsH_3, the value of Raman peak corresponds to 521 cm^{-1}. However, when silicon is doped using AsH_3, the value of Raman peak corresponds to 522 cm^{-1}. This change in the spectrum is generated for the stress in the lattice.

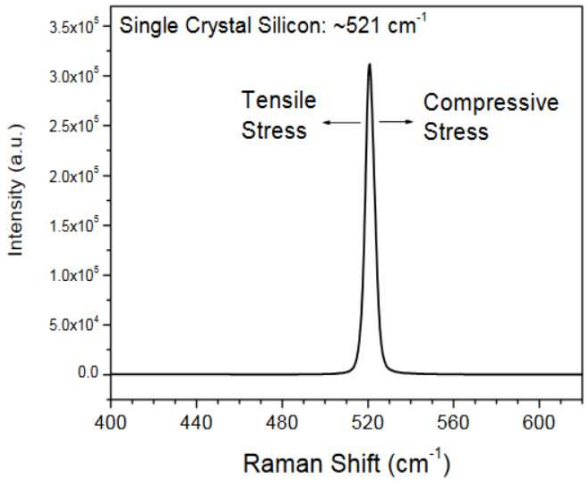

Figure 3.21. Raman spectrum of stress-free single crystal silicon [20].

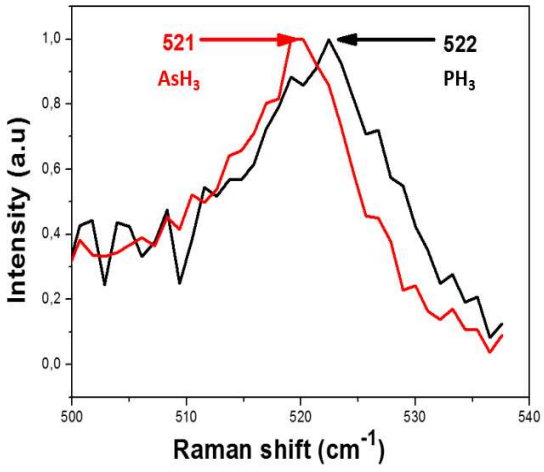

Figure 3.22. Raman spectrum of Sample 1 (black) and sample 6 (red).

This shift can be explained by the fact that the ionic radius of Arsine (119 pm) is similar to that of Silicon (111 pm), but is higher for Phosphorus (195 pm). When the atomic radius is different to the host atoms, this causes strain lattice hence, instability in the crystal structure and in the measures.

The use of Phosphorus as doping gas, whose radius is larger than the host (silicon) induces a compressive stress in the lattice, however for Arsine the ionic radius is similar to silicon, maintain constant the lattice.

9.1.2 Influence on deposition with Pulse in RF power

The values obtained in the GF using a constant RF and LF power is practically the same for both doping gases. We decided then to test if while applying some pulse on RF power, it is possible to see some differences in the sensitivity of N-type μc-Si. As in previous section, Table 3.12 shows the conditions used with its values followed by the graphics obtained, Figure 3.23.

	RF	LF	DOPING GAS	GF
SAMPLE 4	PULSE 0-40 W	600 W	**20 PH_3**	- 30
SAMPLE 5			**20 AsH_3**	- 45

Table 3.12. Summary conditions and value of the GF obtained for sample 4 and 5

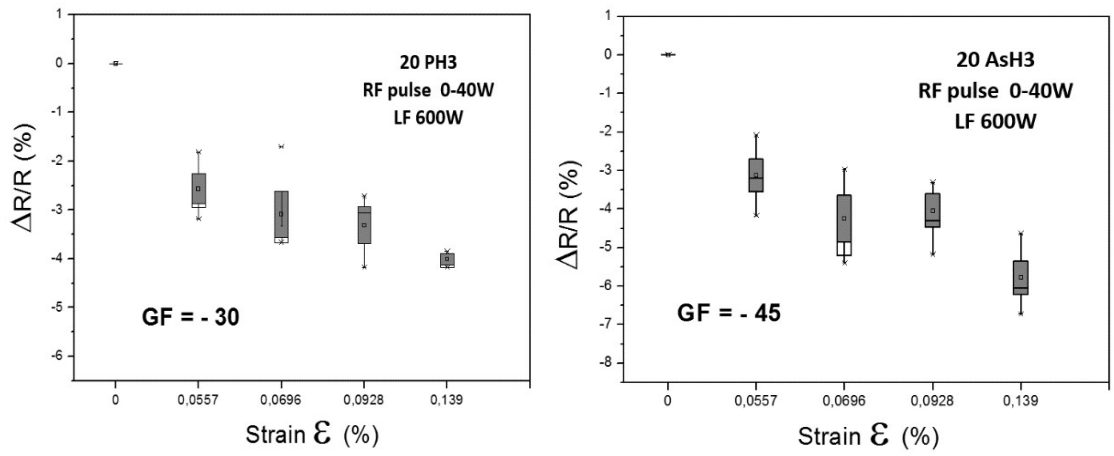

Figure 3.23. Box plot graphic for conditions of Sample 4 and Sample 5.

Here it is obtained a remarkable difference in the GF between both doping agents when a pulse is used in the RF power.

This is due to the addition of pulses in the plasma which generates a higher plasma density compared to the traditional process. When the plasma density is higher, it leads to a higher rate of dissociation of the precursor molecules. [21]

Hence, making a comparison for PH_3 as doping gas, the value of the GF is the same when RF power is applied with RF=0W (Table 3.12) and RF pulse between 0-40W (Table 3.13).

However, when pulses are applied in RF power, and by using AsH_3 as doped gas, the value of the sensitivity increases from -34 to -45. This can be due to the fact that applying pulses on RF power, helps the molecules' dissociation during the deposition process.

AsH_3 presents a slow diffusion, around ten times less, then PH_3 as it is shown in the literature [22]. Our theory is then that with the application of pulse in the plasma, this diffusion is accelerated, and leads to an increase of the GF compared to the one obtained with a constant pulse plasma.

9.1.3 Effect of doping flow rate with pulse in RF power

After analyzing the sensitivity of the samples while applying pulses in the RF power, we will study the influence of the flow rates of the doping gases on the sensitivity, when they are reduced by half, from 20sccm to 10sccm.

Firstly, this was analyzed for PH_3 as doping gas. Table 3.13 shows that there are quite no variation in GF while decreasing the doping level. Figure 3.24 presents the box plot of the change of the resistance under strain. This can be due to the necessity dose required for this gas under the chosen conditions tends to be immediately saturated, which is sufficient with 10sccm.

Doping Gas: PH_3				
RF	**LF**	**Gas flow [sccm]**		**GF**
PULSE 0-40 W	600 W	**20 sccm**	**SAMPLE 4**	-30
		10 sccm	**SAMPLE 9**	-35

Table 3.13. Summary conditions and value of the GF obtained for sample 1 and 6

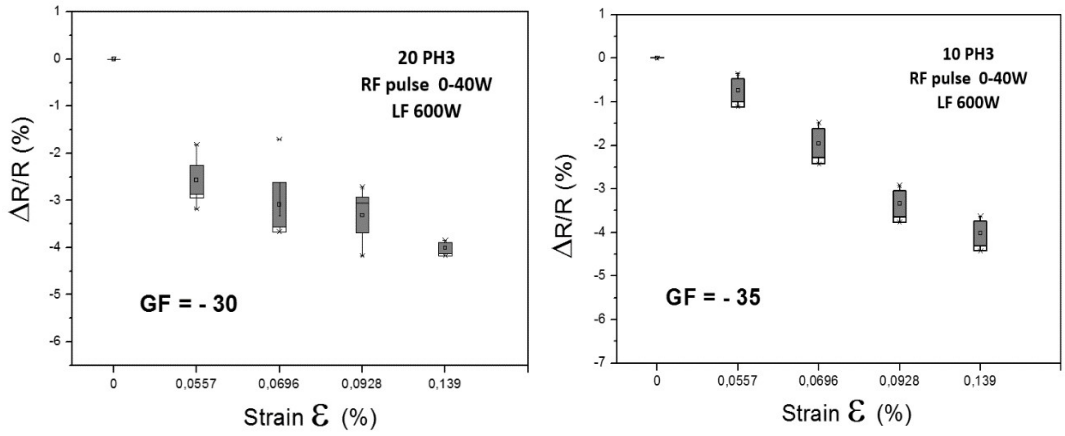

Figure 3.24. Box plot graphic for conditions of Sample 4 and Sample 9.

Secondly, the case of AsH_3 as doping gas is studied. Table 3.14 shows that GF decrease from -45 to -31. Hence the flow rate for this doping gas is relevant in the sensitivity in this case. Indeed, when the gas flow rate of AsH_3 increases, the sensitivity of the material also increases.

Doping Gas: AsH_3				
RF	**LF**	**Gas flow [sccm]**		**GF**
PULSE 0-40 W	600 W	**20 sccm**	**SAMPLE 5**	**-45**
		10 sccm	**SAMPLE 10**	**-31**

Table 3.14. Summary conditions and value of the GF obtained for sample 5 and 10.

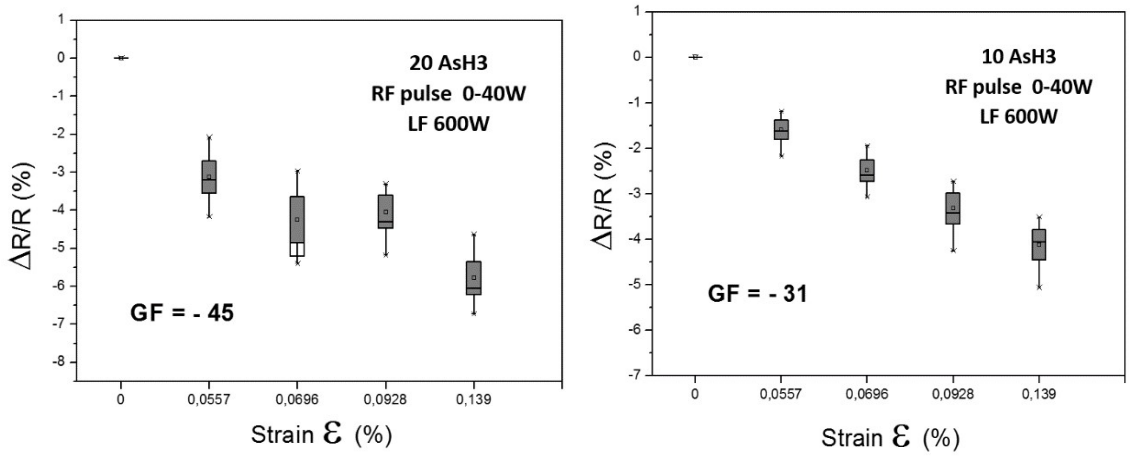

Figure 3.25. Box plot graphic for conditions of Sample 5 and Sample 10.

9.2 Investigation PH_3 as doping gas

In the case of AsH_3 as doping gas, we obtained different results in the sensitivity, depending on the application of pulses in in the RF power or when the doping gas flow rate is varied.
It was decided to continue our research using PH_3 as doping gas to see if the modification of the deposition conditions improves the sensitivity. To this end, it is proposed the following studies:

9.2.1 Constant RF: 0W and 40W

In previous sections, we studied the effect of RF power by applying a constant RF power (RF = 0 W) and with pulse in the range 0-40. However, no effect were really detected. For that reason, we have tested if there are some difference when the RF is constant but with higher power, 40W. Generally, when the power is incremented, the density of the plasma is increased. Table 3.15 shows the conditions and the values obtained for the GF.

DOPING GAS:20 (sccm) PH_3			
	RF	**LF**	**GF**
SAMPLE 1	**0 W**	600 W	- 30
SAMPLE 3	**40 W**		- 35

Table 3.15. Summary conditions and value of the GF obtained for sample 1 and 3.

It is not surprising that these values are quite the same. Indeed, when pulses in the RF power were applied, the plasma density is higher and the maximum power applied during the pulse correspond to the constant value of RF = 40W.

9.2.2 Effect of LF or RF power

As it was study before, the applied pulse in RF power does not affect the sensitivity (GF is -30 or -35).. For that reason, it was decided to see the effect of the pulse in LF power.
The application of pulses in LF power increments the ion acceleration in the sheath and is considered to enhance the surface migration, that should increase the crystallinity [23]. A study of this effect was done by applying pulse in the LF power from 600 to 900W.

Table 3.16 shows a comparative between a constant RF power and the effect of apply pulse in RF and LF power.

DOPING GAS:20 (sccm) PH_3			
	RF	**LF**	**GF**
SAMPLE 1	**0 W**	600 W	- 30
SAMPLE 2	**0 W**	**PULSE**	- 45
SAMPLE 4	**PULSE**	600W	- 30

Table 3.16. Summary conditions and value of the GF obtained for sample 1, 2 and 4.

The pulses addition in LF power produce an increment in the crystallinity fraction also produce an increment in the conductivity due to the decrease of amorphous fraction in boundaries between μc-Si grains of the material, improving it sensitivity.

9.2.3 Flow rate in PH_3 with RF = 0W

Previously, in Table 3.14, the effect of the gas flow rate was studied, when the deposition is realized with pulsed RF between 0W and 40W. For this reason, the experiment was repeated by reducing the doping gas flow rate to 20, 10 and 5 sccm. Table 3.17 presents the values obtained for the resistivity and for GF depending of the flow rate used during the deposition process. Figure 3.27 shows these results.

DOPING GAS: PH_3					
	RF	**LF**	**Flow rate [sccm]**	**ρ (Ωxcm)**	**GF**
SAMPLE 1	0 W	600 W	**20 sccm**	0.165±0.0228	-30
SAMPLE 8			**10 sccm**	0.170±0.0151	-43
SAMPLE 7			**5 sccm**	0.668 ±0.0447	-60

Table 3.17. Summary conditions and value of the GF obtained for samples 1, 7 and 8.

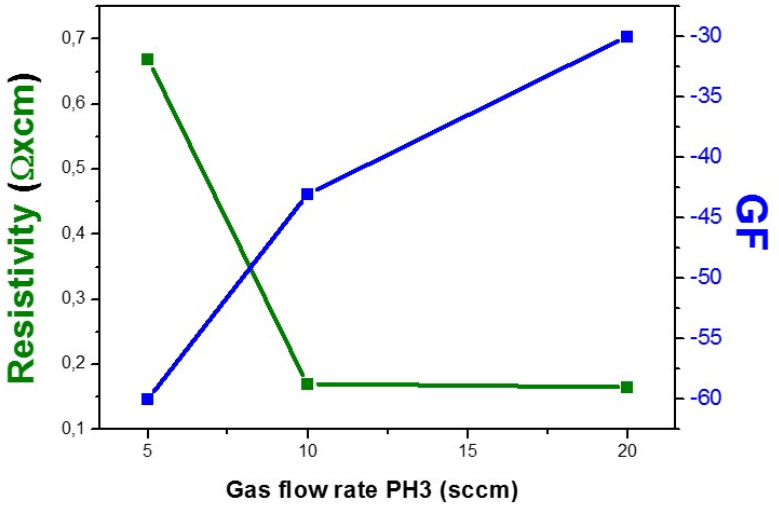

Figure 3.26. Box plot graphic for conditions of samples 1, 7 and 8.

On Figure 3.26, it is observed that, when the doping concentration is reduced, it leads to an increase in the gauge factor. However, in previous Table 3.14, when AsH_3 is used as doping gas, it occurs in the contrary sense, the GF increases when the flow rate is incremented. This is also observed in the literature, as show in Figure 3.28 that represents the value of GF for P and N type depositions on polysilicon versus the doping concentration. Here the GF increments until one optimal concentration and after that, it decreases when the doping concentration increases [24].

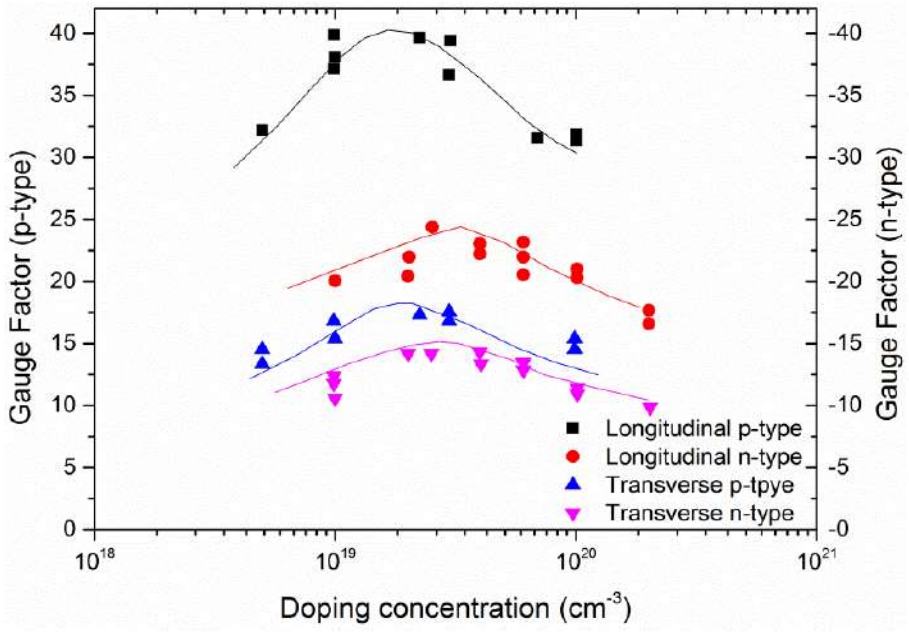

Figure 3.27.GF as a function of doping concentration for boron and phosphorus doped material. [24]

10. Conclusion

Throughout this chapter it was analyzed the piezoresistive properties of µc-Si deposited by two different techniques PECVD and ICPCVD. To do that it was used TLM structure.

The aim was to study different parameters such as the specific contact resistance or the uniformity of the deposition though resistivity measurement at different points. Also this structure was used to calculate the sensibility of the material in front of different curvature radius.

With the results obtained, it was observed several things such as:

For PECVD samples, the values obtained for µc-Si were similar to the values obtained before in the laboratory for this material. However, it was observed that decrease in the thickness of the global structure does not affect the sensitivity of µc-Si, obtained similar values for the three structures, however, the not uniformity of the deposition increases when the thickness of the structure decreases.

ICPCVD samples were also investigated using ten different conditions. Here it was compared the doping gases flow rate and the effect of applied pulse in RF and LF power.

By using the same doping gas with the same flow rate it was demonstrated that applied pulses in the plasma decrease the transfer length between the semiconductor and the electrodes, thus decreasing the specific contact resistance value and increasing the crystalline fraction of the material.

The sensitivity of the samples where it was used AsH_3 as doping gas (S5, S6, S10) have a notorious increment of the GF when it is applied pulse on the RF power.

However, using PH_3 as doping gas it was necessary to vary the quantity of gas flow to appreciate some variations in the GF. This variation was only appreciated with a constant RF power, the results obtained in the GF when the quantity of PH_3 from 20 to 10 sccm and it is applied some pulses in the RF plasma are practically the same.

Hence, it was demonstrated that when it is applied high energy plasma on the samples doped with AsH_3, the values for the GF increase notorious, however in samples doped with PH_3, it is not necessary to have a high energy in the plasma due to its lower diffusion coefficient. To see some increments in GF using this doping agent it is necessary to decrease the amount of flow rate injected during the deposition process.

In the next chapter, we will use some of these conditions to create the sensor that will be used in dynamic deformations. For ICPCVD deposition, due to the standard deviation of PH_3 as doping agent is lower than AsH_3 this will be the doping gas selected.

11. Annex

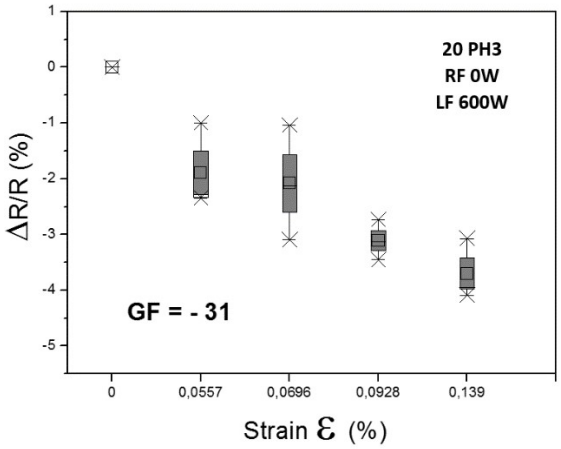
20 PH3
RF 0W
LF 600W
GF = - 31
ΔR/R (%)
Strain ε (%)
0
0,0557
0,0696
0,0928
0,139

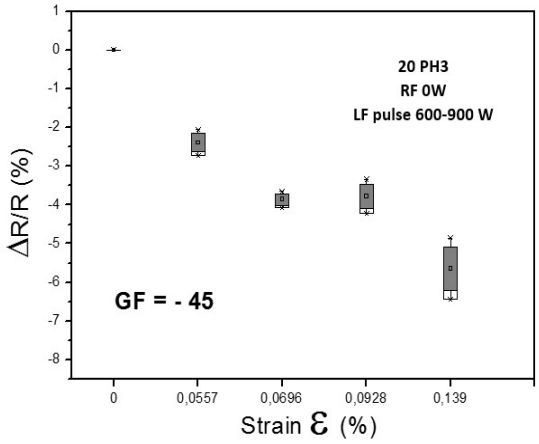
20 PH3
RF 0W
LF pulse 600-900 W
GF = - 45
ΔR/R (%)
Strain ε (%)
0
0,0557
0,0696
0,0928
0,139

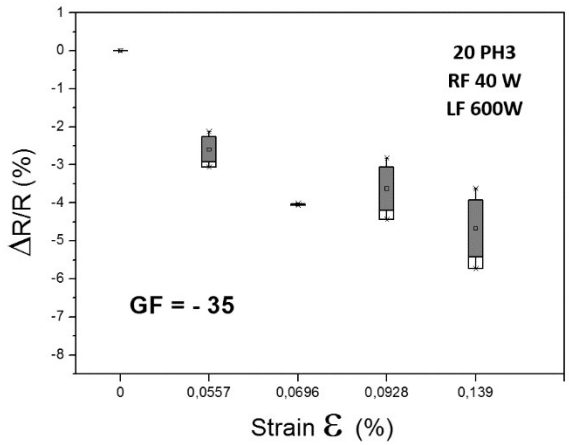
20 PH3
RF 40 W
LF 600W
GF = - 35
ΔR/R (%)
Strain ε (%)
0
0,0557
0,0696
0,0928
0,139

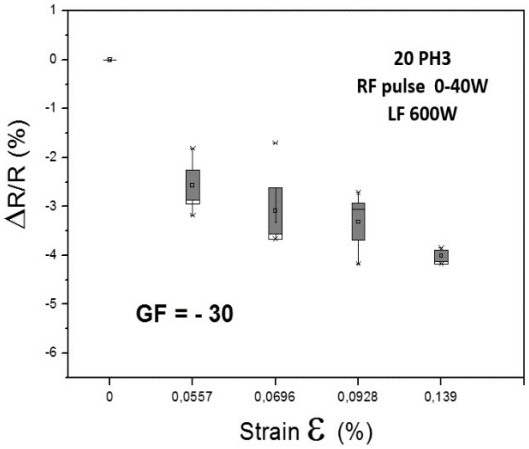
20 PH3
RF pulse 0-40W
LF 600W
GF = - 30
ΔR/R (%)
Strain ε (%)
0
0,0557
0,0696
0,0928
0,139

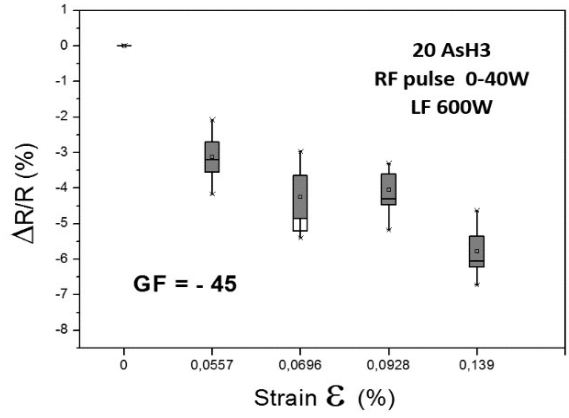
20 AsH3
RF pulse 0-40W
LF 600W
GF = - 45
ΔR/R (%)
Strain ε (%)
0
0,0557
0,0696
0,0928
0,139

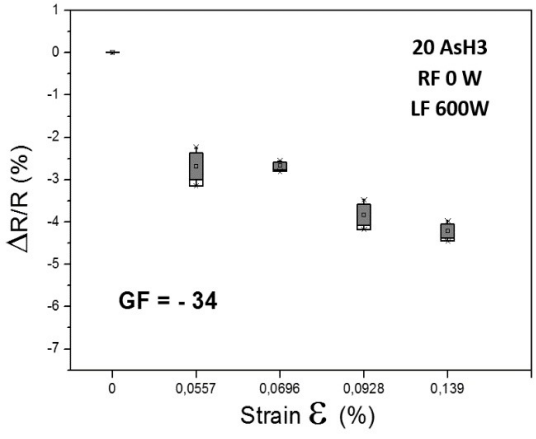
20 AsH3
RF 0 W
LF 600W
GF = - 34
ΔR/R (%)
Strain ε (%)
0
0,0557
0,0696
0,0928
0,139

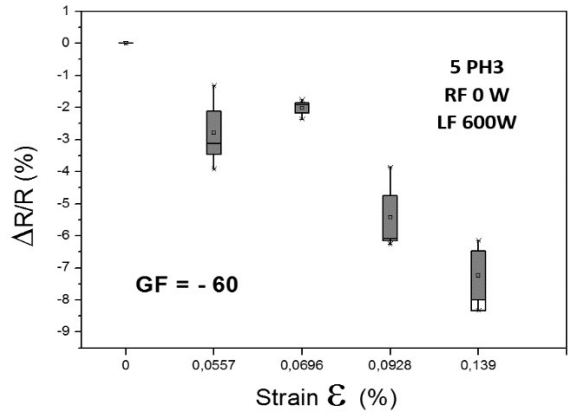
5 PH3
RF 0 W
LF 600W
GF = - 60
ΔR/R (%)
Strain ε (%)
0
0,0557
0,0696
0,0928
0,139

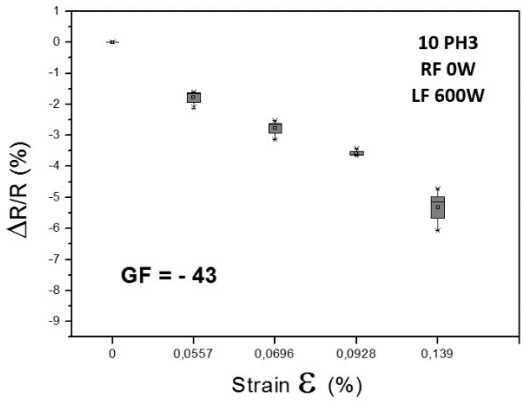
10 PH3
RF 0W
LF 600W
GF = - 43
ΔR/R (%)
Strain ε (%)
0
0,0557
0,0696
0,0928
0,139

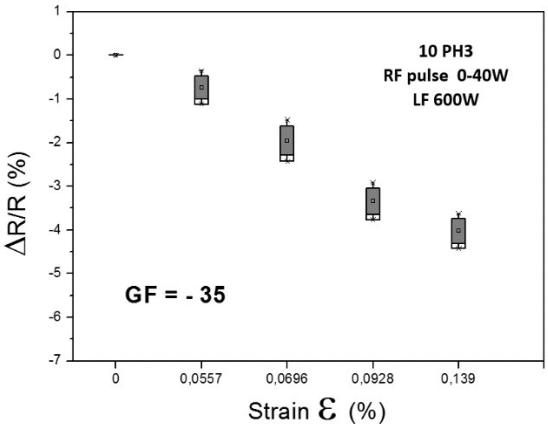
10 PH3
RF pulse 0-40W
LF 600W
GF = - 35
ΔR/R (%)
Strain ε (%)
0
0,0557
0,0696
0,0928
0,139

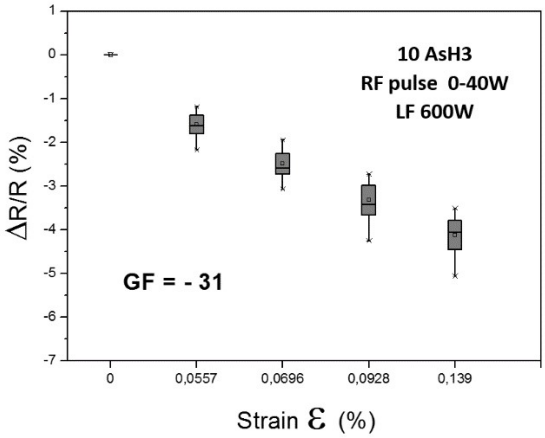
10 AsH3
RF pulse 0-40W
LF 600W
GF = - 31
ΔR/R (%)
Strain ε (%)
0
0,0557
0,0696
0,0928
0,139

12. References

[1] A. Goetzberger and R. M. Scarlett, 'Research and investigation of inverse epitaxial uhf power transistors', Clevite transistor PALO ALTO CA SHOCKLEY TRANSISTOR DIV, Sep. 1964.

[2] Y. Kervran 'Cartographie d'un champ de pression induit par l'occlusion dentaire', thesis, Rennes 1, 2015.

[3] S. Grover, 'Effect of Transmission Line Measurement (TLM) Geometry on Specific Contact Resistivity Determination', thesis Rochester Institute of Technology 2016.

[4] S. Wolf and R. N. Tauber, *Silicon Processing for the Vlsi Era: Process Technology*, 2nd ed. Sunset Beach, Calif: Lattice Press, 2002.

[5] N. Stavitski, J. H. Klootwijk, H. W. van Zeijl, A. Y. Kovalgin, and R. A.M. Wolters, 'Cross-Bridge Kelvin Resistor Structures for Reliable Measurement of Low Contact Resistances and Contact Interface Characterization', *IEEE Trans. On Semicond. Manuf.*, vol. 22, no 1, pp. 146–152, Mar. 2009.

[6] D. J. Gardiner and P. R. Graves, Eds., *Practical Raman Spectroscopy*. Berlin Heidelberg: Springer-Verlag, 1989.

[7] H. Wernerus, M. Bivour, L. Kroely, M. Hermle, and W. Wolke, 'Characterization of Ultra-thin μc-Si:H Films for Silicon Heterojunction Solar Cells', *Energy Procedia*, vol. 55, pp. 310–319, 2014.

[8] G. Viera, S. Huet, and L. Boufendi, 'Crystal size and temperature measurements in nanostructured silicon using Raman spectroscopy', *J. Appl. Phys.*, vol. 90, pp. 4175–4183, 2001.

[9] J. Zi, H. Büscher, C. Falter, W. Ludwig, K. Zhang, and X. Xie, 'Raman shifts in Si nanocrystals', *Appl. Phys. Lett.*, vol. 69, no. 2, pp. 200–202, Jul. 1996.

[10] E. Anastassakis, 'Strain characterization of polycrystalline diamond and silicon systems', *J. Appl. Phys.*, vol. 86, pp. 249–258, Jul. 1999.

[11] B. Le Borgne, 'Microcapteurs chimiques basés sur des couches nanométriques de silicium polycristallin : application à la détection de plomb', thesis Rennes1, 2016.

[12] K. Kandoussi, 'Procédé de fabrication à T<200°C de transistors en couches minces de silicium microcristallin déposé par PECVD en mélange SiH_4-H_2-Ar.', thesis, Rennes 1, 2007.

[13] B. J. Jones and J. J. Ojeda, 'Substrate and material transfer effects on the surface chemistry and texture of diamond-like carbon deposited by plasma-enhanced chemical vapour deposition', *Surf. Interface Anal.*, vol. 44,, pp. 1187–1192, 2012.

[14] W.-Y. Chang, T.-H. Fang, and Y.-C. Lin, 'Physical characteristics of polyimide films for flexible sensors', *Appl. Phys. A*, vol. 92, pp. 693–701, Aug. 2008.

[15] M. Amirzada, A. Tatzel, V. Viereck, and H. Hillmer, 'Surface roughness analysis of SiO2 for PECVD, PVD and IBD on different substrates', *Appl. Nanosci.*, vol. 6, pp. Mar. 2015.

[16] H. Gleskova, S. Wagner, and Z. Suo, 'Failure resistance of amorphous silicon transistors under extreme in-plane strain', *Appl. Phys. Lett.*, vol. 75, pp. 3011–3013, Dec. 1999.

[17] J. Gaspar, A. Gualdino, B. Lemke, O. Paul, V. Chu, and J. P. Conde, 'Mechanical and piezoresistive properties of thin silicon films deposited by plasma-enhanced chemical vapor deposition and hot-wire chemical vapor deposition at low substrate temperatures', *J. Appl. Phys.*, vol. 112, Jul. 2012. pp.

[18] Z. Suo, E. Ma, H. Gleskova, and S. Wagner, 'Mechanics of Rollable and Foldable Film on Foil Electronics', *Appl. Phys. Lett.*, vol. 74, pp. 1177–1179, Feb. 1999.

[19] H. Gleskova, P. I. Hsu, Z. Xi, J. C. Sturm, Z. Suo, and S. Wagner, 'Field-effect mobility of amorphous silicon thin-film transistors under strain', *J. Non-Cryst. Solids*, vol. 338–340, no. 1 SPEC. ISS., pp. 732–735, Jun. 2004.

[20] V. T. Srikar and S. Spearing, 'A Critical Review of Microscale Mechanical Testing Methods Used in the Design of Microelectromechanical Systems', *Exp. Mech.*, vol. 43, pp. 238–247, Sep. 2003.

[21] D. Lundin and H. Pedersen, 'High Power Pulsed Plasma Enhanced Chemical Vapor Deposition: A Brief Overview of General Concepts and Early Results', presented at the Physics Procedia, 2013, vol. 46. pp.

[22] S. W. Jones, 'Diffusion in Silicon', 2008.

[23] I.-K. Oh *et al.*, 'Very high frequency plasma reactant for atomic layer deposition', *Appl. Surf. Sci.*, vol. 387, pp. 109–117, Nov. 2016.

[24] D. Grech, 'Development of a Quasi-concertina MEMS sensor for the characterisation of biopolymers', 2014. .

Chapter 4- Dynamic deformation

1. Introduction

The previous section has been focussed on the piezoresistive effect of N-type microcrystalline silicon, deposited by using two different deposition techniques, PECVD and ICPCVD.

Transmission line measure (TLM) structure was used to extract parameters such as contact resistance (Rc), specific contact resistivity (ρc) or sheet resistance of the semiconductor (R_{SH}). Moreover, the uniformity and the sensitivity of µc-Si when the material is submitted to different curvature radii, corresponding to the gauge factor (GF), were studied.

These parameters were obtained through static characterization bending test, however, one of the main innovations of this thesis is to study how µc-Si reacts to dynamic deformations to perform a sensor that is able to detect fast, continuous and weak deformations.

There are important advantages when dynamic measurements are realized because it provides more information about the behaviour of the materials and the sensor's structure. To obtain a sensor with good reliability and accuracy, the reaction to the applied stimulus should be linear, with high sensibility, the amplitude of the variations should present the similar values and moreover, the intrinsic structure of the materials should be able to come back quickly to the initial state.

Unfortunately, the main disadvantage of dynamic deformation is that it requires expensive and sophisticated characterization systems. For this reason, in our case, various low-cost prototypes have been developed with a home-made acquisition system set up. These have been evolved along this thesis until the completion of the final design.

Since this was the first time µc-Si was submitted to dynamic deformations in the laboratory, we did not know how it would react. For this reason, the first circuit was designed to be used with a wide range of resistance values. To make a comparison between the structures studied, different parameters were tested to characterize the sensors and those to which all the sensors are able to react were selected

Hence, along this chapter, we will explain the process followed in the development of the new acquisition system, the considerations taken to choose the appropriate microcontroller and the creation of a new specific software code for this one. Furthermore, an electronic circuit has been developed to adapt the new design. Several prototypes were created to obtain a reliable frequency system that let us to work at variable pressures and velocities and allows to apply

different wave shapes over the devices. Therefore, in order to create the new dynamic set up, it was necessary to modify the computer processing, the connectors and the prototypes to realize the deformation.

The signal processing system selected for this new system is the Arduino platform, because it presents some advantages as a good quality- price ratio, a big forum platform with many projects and examples, a C-based programming language that allows a user with basic programming knowledge configures the microcontroller. However, it presents some design limitations as the resolution levels, the range of input voltage, the processing speed, etc. These limits will be commented below. This fact forces us to look for other alternatives to adapt our sensors and take full advantage of all the possibilities offered by Arduino.

2. Characterization system

One of the main reasons to discard TLM mask to perform dynamic measurements is that its design is not adequate for this type of measurement; moreover, due to its geometry design, it induces noise during its characterization.

The previous characterization system based on probes with needles on the edge, it is not compatible with dynamic deformations, so it was necessary to create a new one dedicated to dynamic deformations.

The first problem was to design a system to applied continuous deformations always with the same amplitude and modulating frequency. To do that, several ideas were proposed, such as flex tensional piezoelectric actuator, or the use of a motor with cylinders that press the sensor; however, all this options were not precise.

After some research and testing with a homemade system used to apply the deformations, a flow control system called Elveflow OB1 [1] was bought. This equipment is based on piezoelectric regulators, enabling a flow control 20 times more precise and 10 times faster than the other flow controllers on the market. Generally, it is used for microfluidic applications but in our case, it has been configured to be used with compressed air. Moreover, it was necessary to create a platform to apply this pressure. For this goal, the sensor is placed onto a homemade vibration membrane that changes its shape when the impulse is applied. As the sensor is totally attached to the membrane, the impulse is exactly reproduced on the sensor. The vibration membrane is connected to the pressure supply machine whose outlet can be set with a specific

pressure range that can be modulated to create different shapes. The system is shown on Figure 4.1

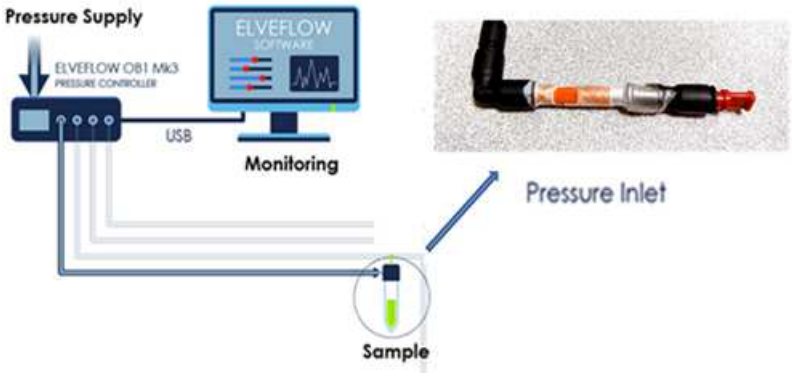

Figure 4.1 Schematic of Elveflow OB1 pressure machine and rubber membrane [1].

For the TLM mask, the electrodes are very close to the place where the deformation is applied and the probes used to realize the characterization have a needle in the edge to realize the contact between the devices' electrodes and the acquisition system, Figure 4.2. For dynamic measurements, this method is not a good option for two reasons: *i)* due to the low thickness of the substrate (25 µm) it is easier that the needle makes holes on it during the manipulation moreover, *ii)* when the deformation is applied, the membrane moves and the distance between the probes and the electrodes changes. For that reason, in order not to lose contact, it is necessary that the probes be moved with the stimulus. This fact was an important reason in the design of the new mask to place the electrodes at the edge of the mask area and the devices structure in the centre where will be applied the deformations.

To perform the connection between devices probes we tried different methods until we found the most appropriated to our goal.

For the design of the new mask, the electrodes have been done following the dimensions required to use the connector shows in Figure 4.3. These connectors used a kind of pins that must be embedded in the substrate, however when some vibrations of the deformation go to the edge, the pins produced a tear on the thin substrate.

Another option, tested to discard the use of the probes needles, pins or another method that implies creating holes on the substrate, was to use directly thin wires soldered to the electrodes through silver conductive Epoxy. Figure 4.4 shows an example of it.

With this method, the contact between electrodes and probes is total; moreover there are no holes on the substrate. The big drawback is that the solder have to be done on each device, with difficulty for the handle and with high time-consuming.

Finally, to optimize the time and make a mix between the main advantages of the three connector´s methods used, we design a board card, shows on Figure 4.5. It consists of a piece of resin card where the electrodes are printed with the same dimensions than the electrodes of our mask design and both of them are pressed between them.

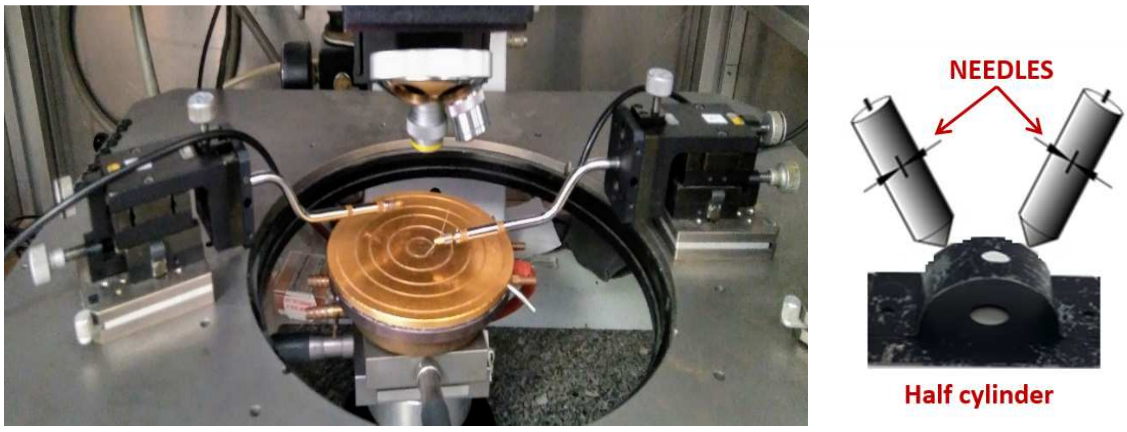

Figure 4.2 Characterization system based on probes with needles to perform static deformations.

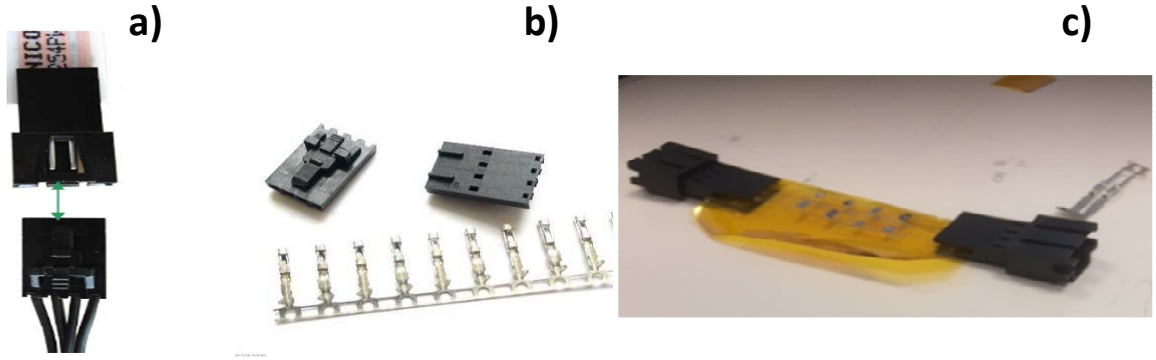

Figure 4.3 a) Connectors adapter for the new mask b) Pins that are embedded to the substrate c) New mask design with the connector

Figure 4.4 Silver conductive Epoxy and example of one of our sensor

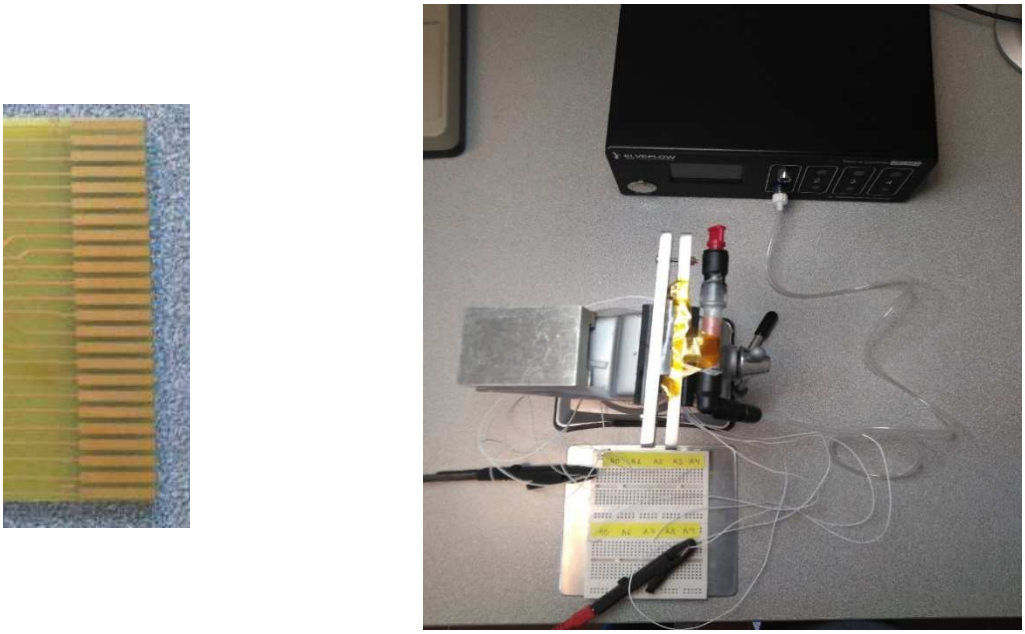

Figure 4.5 Board card of resin with printed electrodes and final system with the sensors connected to the board card.

3. Data acquisition system

The necessity to change the probes connectors forced us to modify the acquisition system. We decided to choose a small system that can be easily transported to get a mobile system.

Currently, in the electronic market we can find different low-cost hardware to perform data acquisition. However for our project, Arduino was selected because it is one of the most used. This platform gives a huge information, documents, forums and projects available that helped us to solve our problems.

Then, to show the possibilities that it offers and the considerations that had to be taken into account, its architecture and the basic knowledge that it is necessary to understand how to work with this microcontroller are briefly explained. Figure 4.6 shows a picture of Arduino UNO with its components. However, the theory focuses on the components that have some influence on our characterization system set up. This will be separated into the kind of input pins, the basic specifications, and acquisition theory of microcontroller and the kind of communication used between the PC and the module.

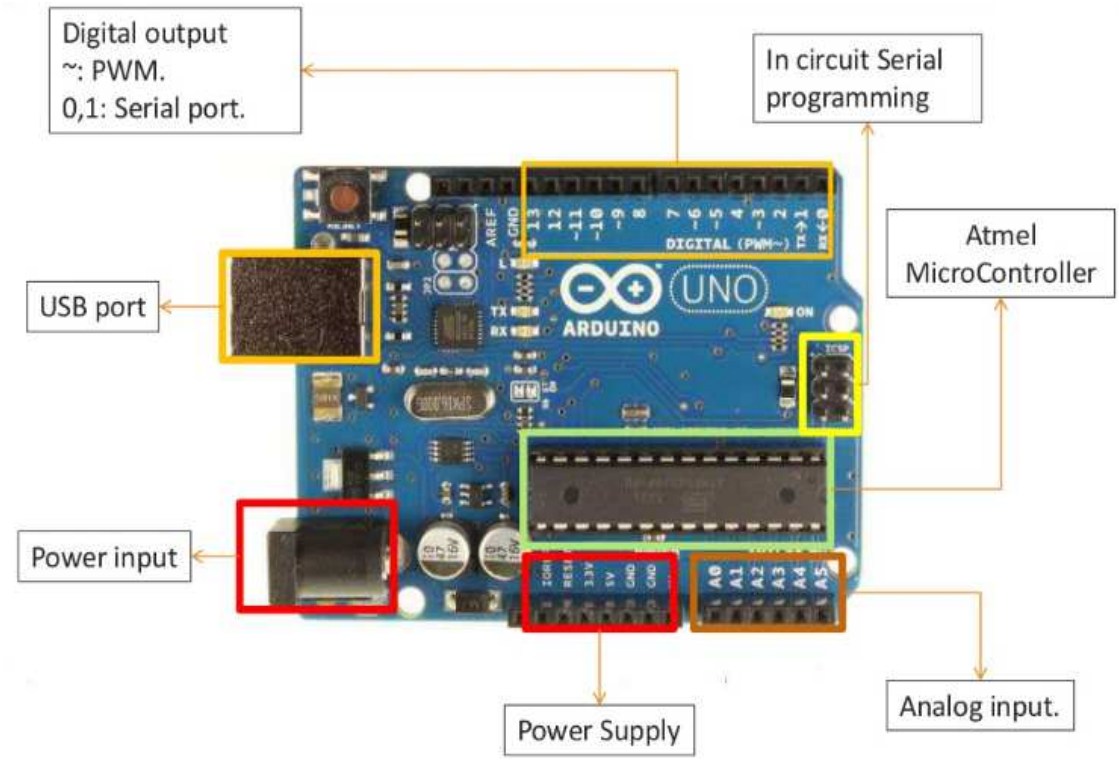

Figure 4.6. Arduino UNO architecture [2].

3.1 Inputs pins

The pins' groups can be divided into the digital pins and the analog pins. However, for our circuit, only analog pins are used and they are used to transform the signal produced by the sensor into information easy to process for the ADC converter.

The analog pins are connected to the ADC converter through a multiplexer. This is a necessary component as the Arduino doesn't present the possibility to work with more than one input at the same time, which means that once one input is analysed, it can shift to the next one. The time that it needs to read one analog input and pass to the next takes around 100 microseconds,

so the maximum reading rate is about 10,000 times a second [2]. This is important to take it in an account if we want to compare the data of several inputs.

Each of these pins is capable of digitizing an input signal between 0 V and 5 VCC, converting the input voltage to a numerical value that goes from zero to 1023; this range of values corresponds to the resolution of the ADC.

3.2 Analog to Digital Converter

One of the main parts of a data acquisition system, DAS, is the processing unit which is responsible for receiving the signal and coding it to be processed. The most important element of the processing unit is the ADC, Analog Digital Converter. The ADC will be the element that will allow us to transform the analog signal that comes from the sensor into a digital signal or binary form that can be processed (Figure 4.7).

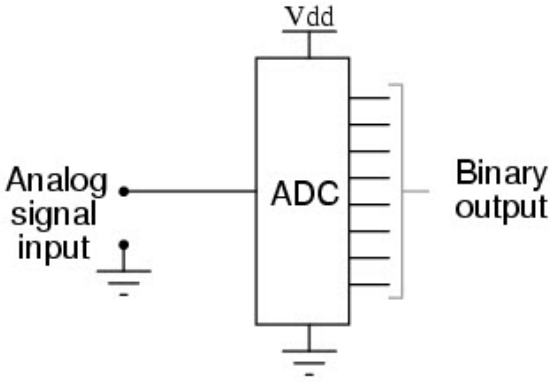

Figure 4.7. Schematic analog to digital converter.[3]

Depending on the ADC chosen and the technology used in the microcontroller, we will be limited to certain design parameters (resolution levels, input voltage levels, processing speed, etc.). Currently, many microprocessors have their own integrated ADC and, thanks to this, we can concentrate all our processing units on a single chip. In Arduino's case, the microcontroller used is ATMEL328P-PU, the most important characteristics of Arduino UNO are shown in Table 4.1.[2]

Voltage range	0-5V	**CPU**	8bits
Microcontroller	ATmega328P	**Clock frequency**	16MHz
Digital Pins	14	**ADC resolution**	10bits
Analog/PWM Pins	6	**Current outside pins**	40mA

Table 4.1. Basic specifications of the Arduino UNO [2].

The two main considerations for a good conversion of analog signals to digital signals are sampling rate and quantization levels or sampling precision.

Sampling rate or sampling frequency corresponds to the rate at which the digital values are sampled from the analog signal to be converted in digital values.

Quantization is the process in which the voltage range signal is divided into several discrete quanta, later the input signal is matched with the correct quantum. The next step is the encoding process where each quantum will be assigned a digital binary code.

The quantum is defined by the term resolution, which corresponds to the conversion of the analog voltage into a digital value in a computer. It is determined by the ADC bits and the voltage range of the ADC and this calculus is done though the Formula 4.1.

When the ADC uses for example 10 bits, that means that when it performs an A/D conversion, the ADC samples the input values present in the analog voltage and converts it into a 10-digit binary number, each digit can take 2^{10}= 1024 values. As shown in Table 4.1 Arduino UNO has an input range of 0V to 5V. This means that the decimal number 0, will be returned by the ADC to the computer when in its analog input is presents the voltage of 0 V, and when the input voltage is 5V will be equivalent to 1024. By this way, the voltage range of 0 to 5V is divided into 1024 levels, with each level is defined by the Formula 1, where Vout represents the voltage range, and N corresponds to the bits number of the ADC, 10bits. With these values, it is possible to calculate the resolution of the ADC which corresponds to 4.88 mV per unit. This value represents each division of the quantization levels.

Figure 4.8 shows an example for the sampling signal using the same ADC voltage range but different resolution bits, as it is observed, for higher bit values in the ADC, the digital signal replicates the analog signal with more precision.

Hence, the accuracy to transform the signal from analog to digital is a combination of sampling and quantization.

$$\text{n-bit DAC Resolution (or step sise)} = \frac{\text{Vout}}{2^N}$$

Formula 4.1. Resolution of ADC calculus.

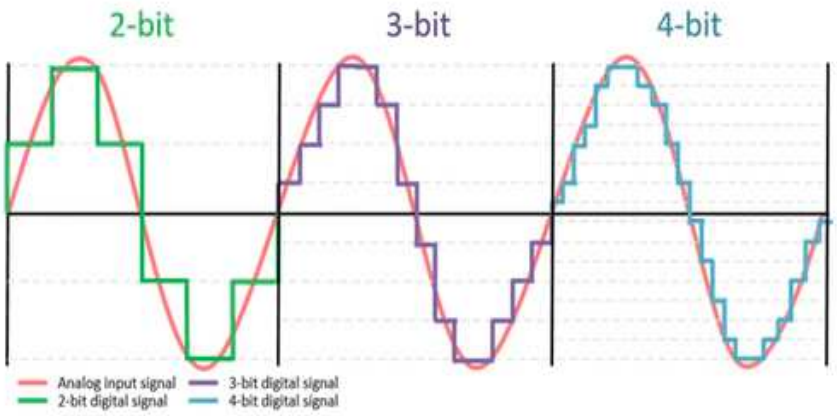

Figure 4.8 Analog signal conversion using ADC of 2 bit, 3 bit and 4 bit of resolution.[4].

Finally, in the last step, the serial communication is realized between Arduino and the computer to transfer the data from one module to the other.

To do that, the UART module is chosen, the unit that uses is bauds. If the bauds are increased, the duty cycle generates more data. The bauds rate rateable in Arduino are: 300, 600, 1200, 2400, 4800, 9600, 14400, 19200, 28800, 38400, 57600, or 115200 and it is defined as the number of symbol changes across the transmission medium per time unit (bits per second). An inappropriate baud rate generates the aliasing phenomenon, this is the distortion or artificial values of the signal. In our case, the maximum baud rate used to avoid erroneous data is 57600.

4. Deformation measurement: electronic and signal processing

Due to the limitations of Arduino in terms of resolution, voltage range or processing speed, it was necessary to create an adaptive electronic circuit to measure the voltage variation produced when the sensor is submitted to different and continuous deformations.

As it was commented before, for Arduino, the resolution of the ADC is 4.88mV, it corresponds to the minimum step between two data points. Our sensors react with variations of few mV for that reason the idea of the adaptive circuit is to select only the variation produced by the deformation and make an amplification of it.

Figure 4.9 shows the global schematic of the adaptive circuit. However, following it will be explained all the steps follow before introducing the signal in the microcontroller.

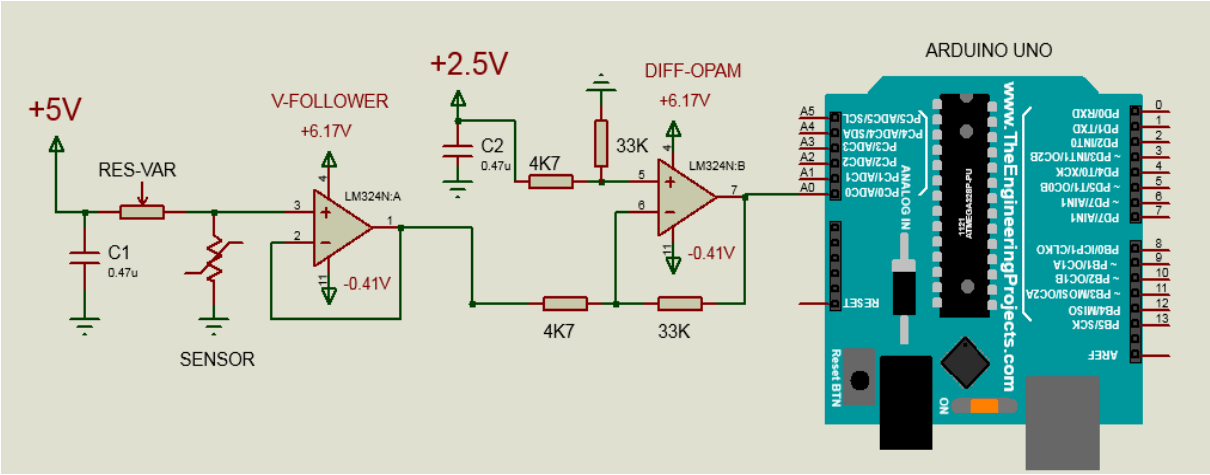

Figure 4.9 Schematic used to adapt our sensor to the acquisition system.

The first block, as shown in Figure 4.10, is to design a voltage divider between our sensor and a variable resistance or potentiometer. The aim of the voltage divider is to obtain a voltage signal because Arduino does not have an analog input where it is possible to directly measure the value of the resistance or the electrical current.

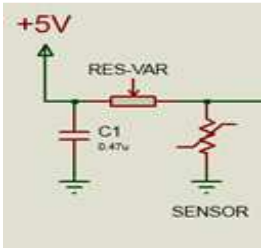

Figure 4.10 Schematic of a voltage divider between our sensor and a variable resistance.

After that, the signal is introduced in an operational buffer or voltage follower, the goal of this component is to prevent the signal source from being affected by any voltages or current.

When the value of the variable resistance in the voltage divider is changed, it is possible to adjust the value of the voltage that we want in the output. It is important to play with this value to determinate the voltage reference that will be introduced in Arduino, thus this value will correspond to the negative voltage input, V1, of the differential amplifier.

The last block used is the differential amplifier, the purpose of this electronic component is double: it makes a difference between two input voltages, which suppresses any voltage common to the two inputs and it amplifies this difference.

Figure 4.11 shows the electronic schematic of this component, where there are two input voltages, V1 (-) that is the voltage signal providing for the voltage divider block, Figure 4.10, and V2 (+) a reference voltage that we have defined as 2.5V.

Moreover, it is possible to do an amplification step which in our case corresponds to gain ≈7. This value was chosen because of the restrictions of Arduino voltage (0-5V), it is not possible to make an excessive amplification, because large values can destroy our microcontroller.

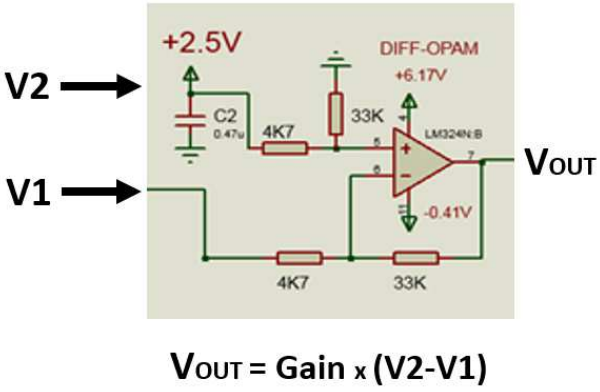

Figure 4.11 Schematic differential amplifier.

When the design of the differential amplifier block was realized, we decided to introduce the signal from our sensor in the negative input, V1 (-). This is due to the fact that for our sensors, the semiconductor material selected is N-type µc-Si and as explained in Chapter 2, with tensile strain, its value decreases. Therefore, in order to make it visually simpler, the signal is inverted, so when a tensile pulse is applied, the resulting signal will increase. One of the main advantages of our design is that it is possible to shift the voltage signal through the voltage divider to fix our signal input reference in Arduino to a determined value. For example, if the input voltage reference is fixed to 2V it is possible to apply deformations in both senses for our sensor, compressive and tensile.

5. Problems and limitation of acquisition system

5.1 Electrical noise

One of the biggest problems we found during the acquisition was the electrical noise. The low level of the variation produced in the signal when the impulse pressure is applied makes it difficult to have distinguishable levels between the electrical noise of the circuit and the variation of the signal.

Depending on the variation of the pressure applied, the signals obtained by the strain gauge could be very small. As a consequence, error signals can even exceed the measuring signals amplitudes, so, in order to determine the sensitivity of our sensor and its working range, this error signal must be suppressed by hardware or by software. Figure 4.12 is an example, a square

pulse signal is applied with a weak variation of pressure, 20mbar. We observe then that the sensor is sensible enough to follow the shape of the signal applied, however by observing this graphic, we can see that the level of noise is 0.02V and the voltage variation on the sensor is 0.01V. Hence, the noise totally covers the sensor signal.

For a square signal, where the deformation applied stays in the same position for certain time, it is possible to distinguish something, however, when the impulse applied is with short duration it is not possible to differentiate the noise from the actual signal.

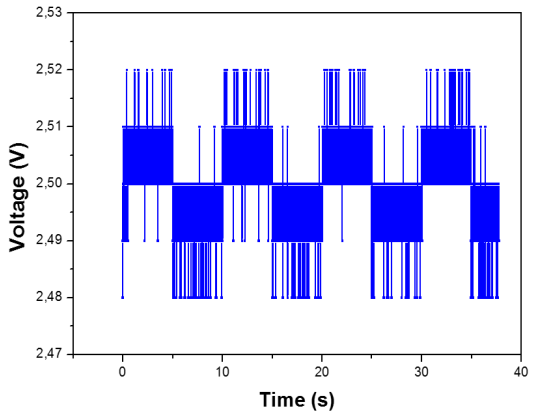

Figure 4.12 Signal obtained when it is applied a square signal with variable pressure 40-20mbar with pulse duration of 5 seconds.

To try to eliminate this problem, we decided to remove the noise of the recovered signal. The filter condition was realized by Origin 8 software. To do this, we first calculated the FFT (Fast Fourier Transform) and based on it, the original signal was filtered with a low pass filter. Figure 4.13 shows an example obtained with a cut-off frequency fc= 48Hz. However, this cut-off frequency (fc) is not always the same, there are some variations on it that could come from different sources such as the vibration of the membrane, the frequency pulse applied or from the µc-Si layer. Moreover, it was not possible to obtain good filtering of the signal in all cases because of the resolution of the ADC, 10 bits, the digital signal obtained is not very accurate for good signal treatment condition.

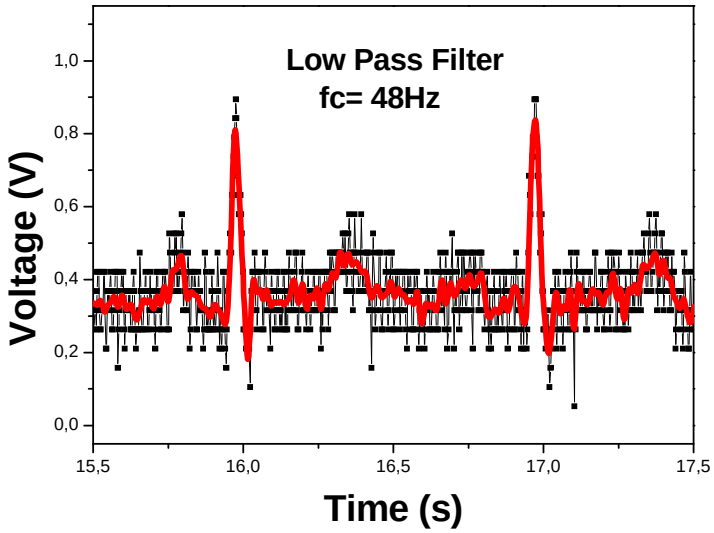

Figure 4.13 Low pass filter with cut-off frequency fc = 48Hz

5.2 Increase ADC resolution since 10 to 32 bits

The other main problem along with the noise is the resolution level of the ADC. As it was commented before, Arduino's ADC has a voltage range from 0-5V and 10bit of the resolution, so the minimum quantum step corresponds to 4.88mV. To improve this resolution, there are only two possible solutions:

1. Arduino has the option to modify the voltage reference of the ADC with the AREF pin, this pin gives us 3.3V instead of 5V which corresponds to the normal alimentation of by this way. According to Formula 4.1 for 3.3V the minimum distance between two points will be 3.3/1023 = 3.22mV. However, this option reduces the maximum voltage range of the ADC since 5V to 3.3V, in this way the hardware amplification that we can realize also is reduced.

2. The second option, which is also the most efficient, is to increment the ADC bits without varying its voltage range. To do this, the unique solution is to connect a new module to Arduino. The selected module is called ADS126 [5], it is a 32-bit Analog-to-Digital Converter (ADC) with Programmable Gain Amplifier (PGA). Moreover this module offers some incorporated filter such as 50Hz reject filter or some others that can be configured. Thanks to the higher resolution, it will be easier to filter the signal later with Origin software.

6. Sensor design to perform dynamic measures

When dynamic deformations are applied, there are several factors that influence the behaviour of the devices. To obtain a sensor that reacts quickly, linearly and with a good sensibility to the deformations, it is necessary to select the appropriate materials and design because both are relevant for the sensor working.

In our case, we wanted to investigate µc-Si effect under dynamic deformation and use different geometry design to improve its sensitivity.

Depending on the sensor's application and the nature of the substrate (rigid, flexible or stretchable), there are different geometries such as serpentine, rosette, etc. Selecting an appropriate design will help to improve the sensitivity as well as the quality-life and efficiency of the devices.

As it was commented before, the necessity to modify the probe for the characterization system to apply dynamic deformations offered us the possibility to change the mask design for a new one adapted to our new acquisition system. It was then necessary to consider different factors.

In a strain sensor, the Gauge factor (GF) depends on the Formula 4.2

$$GF = (1 + 2v) + \frac{(\Delta\rho)}{\varepsilon} = \frac{dR/R}{\varepsilon} \tag{4.2}$$

with ε the mechanical strain, R the electrical resistance, νthe Poisson's ratio, ρ the resistivity

By observing this formula it can be deduced that to improve the GF it is necessary to increase the variation of the resistance obtained before and after deformation. Figure 4.14 shows the design of a resistance. Hence, to improve the sensitivity, the length (L) must be increased without increasing the cross-sectional area (A).

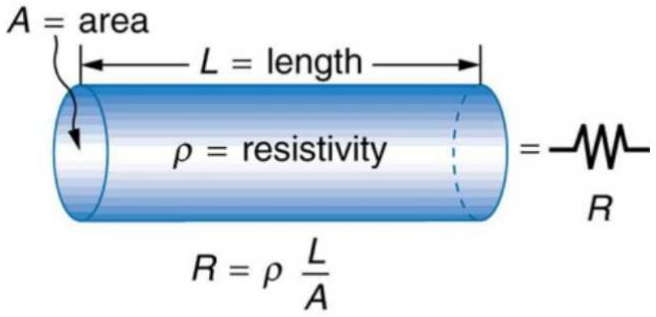

Figure 4.14 Resistance design and formula area definition [6].

Our sensors designs are based on strain gauges. For commercial gauges, their length is the active or strain-sensitive length of the grid and, as shown in Figure 4.15, and resistance are generally designed with a long length in a small area. However in our case, due to the relative rigidity of µc-Si and the previous problems found on this material with the cracks, it was decided to increment the length with no curve in the design.

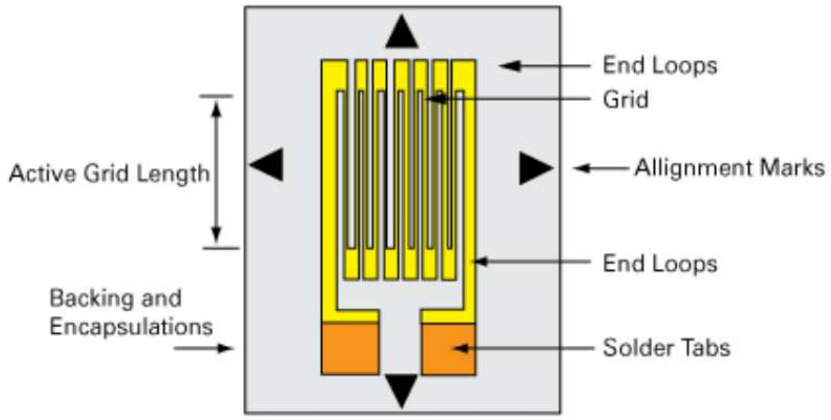

Figure 4.15 Design for a commercial strain gauge sensor [7].

To study the geometry, a mask was designed with Virtuoso Analog Design Software shown in Figure 4.16. It is composed of resistances designs with rectangular shapes and ten resistances in parallel. Table 4.2 presents the different dimensions of this mask design; for the same length (L) there are two different structures with different width (W) (a) and (b).

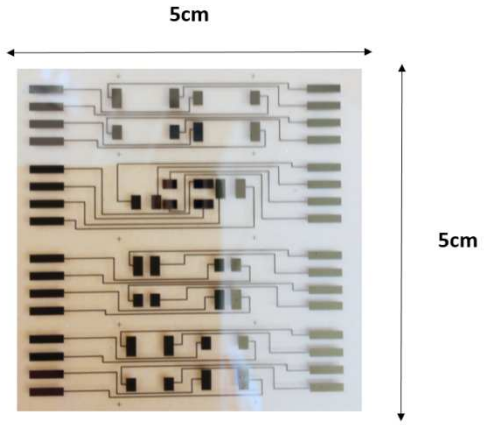

Figure 4.16 Mask resistance design

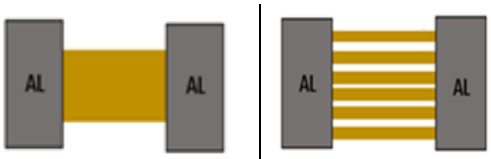

L(µm)	W(µm) (a)	W(µm) (b)
4000	1000	100
1000	1000	100
1500	1200	120
7000	1200	120

Table 4.2 Dimensions of the resistances of the mask of Figure 4.16

Figures 4.16(c), (d), (e), (f) belong to a mask available in the laboratory. The design of this mask is realized to be used with the characterization probes that use needles. To use them with dynamic deformations, it was necessary to stick wires using adhesive conductive epoxy to the 2 rectangular aluminium contacts.

Following, in Figure 4.16 is presented all of the shapes studied

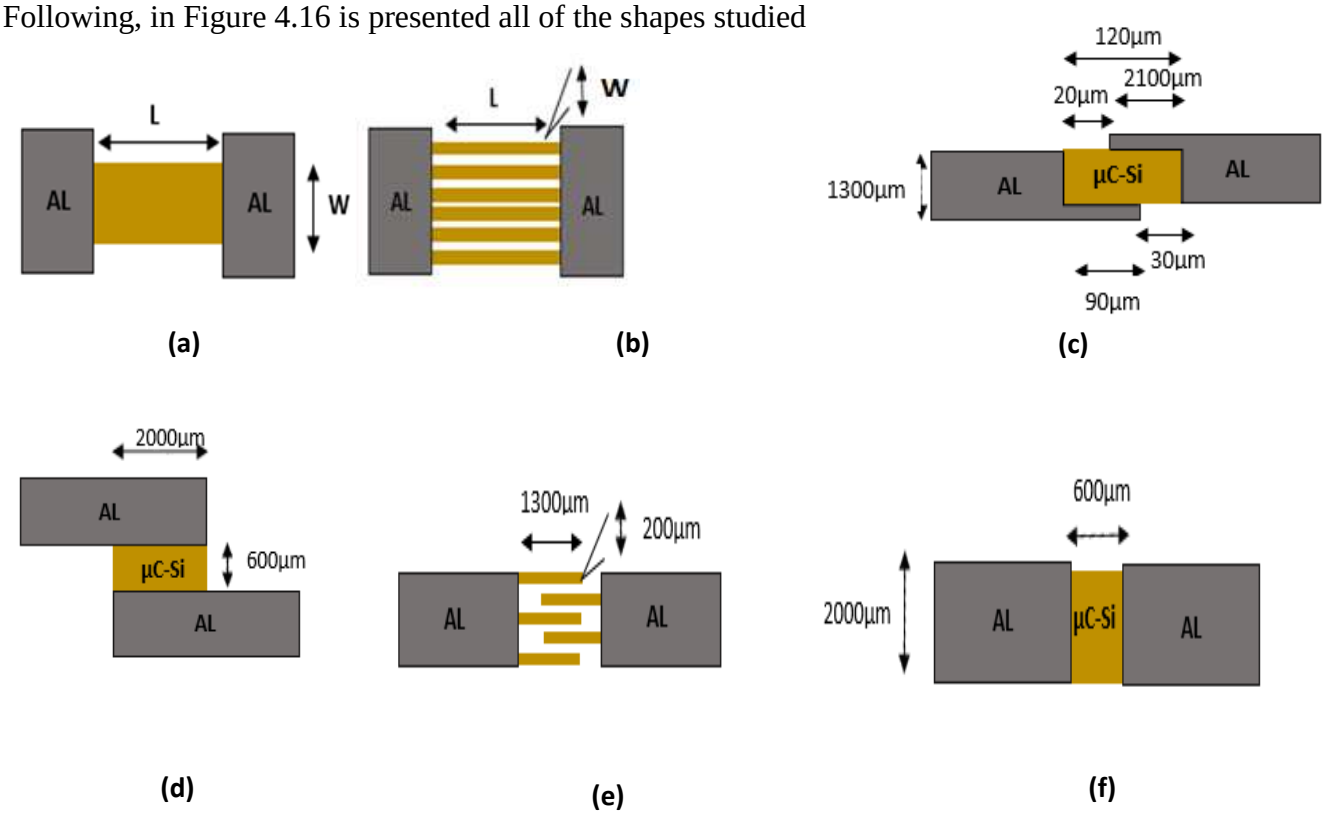

Figure 4.16 Shapes design of all the structures studied.

The sensors are attached on a vibration membrane connected to a flow controller that injects the specific signal shape with the desired pressure. The sensor should reproduce the same shape as the signal applied; Figure 4.17 shows the membrane and how the sensor is attached to it.

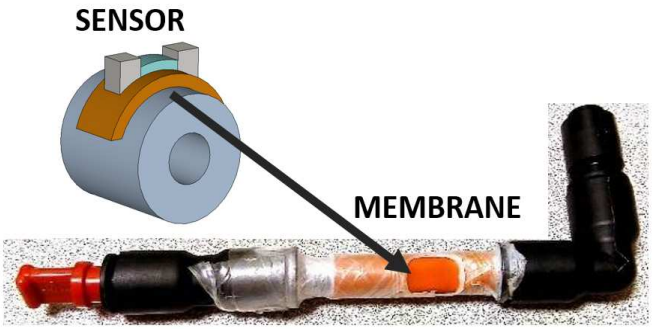

Figure 4.17 Membrane homemade design and sensor place during the deformation.

In order to evaluate the sensitivity of the different structures in front of weak deformation, we studied how their reaction to the same stimulus will determine which design and dimensions could be a good choice for our goal.

This was the first time that these structures were submitted to dynamic deformation, so it was necessary to select the stimulus applied to perform our study. To do that, sensors were submitted to different conditions such as maximum and minimum pressure, wave shape, frequency and duration of pulse until we determined with which conditions a reaction is observed for all the structures. Finally, the selected conditions are shown in Figure 4.18 which corresponds to a simple square pulse with a pressure variation of pressure of 200 mbar and the selected frequency of 0.1 Hz.

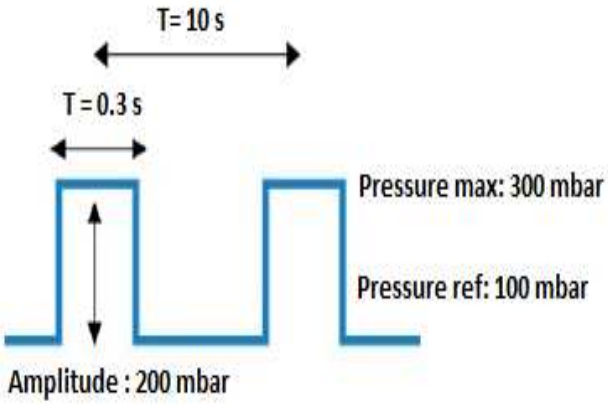

Figure 4.18 Wave conditions selected to do the study of sensitivity in our sensors.

6.1 Design electrodes configuration

To better understand the influence of the behaviour of the design under strain, the first step is to select which electrode configuration is more sensible to the deformations. The correlation between resistance and current flows perpendicular or parallel to the direction of strain was previously reported [8] [9] [10]. These studies demonstrated that when the strain is applied, the stress is concentrated on the electrodes and causes cracks that are perpendicular to the strain direction, Figure 4.19 [11].

Hence, the sense of the current flow in the function of the strain deformation has an important effect on sensor performance.

To illustrate this, the same dimensions of µc-Si were chosen and the electrodes design configuration was modified. The position of the electrodes determines the current flow sense

and corresponds to the length value (L). By this way, in Figure 4.20 (a), the length value corresponds to L= 600µm and for Figure 4.20 (b) it is L=2000µm.

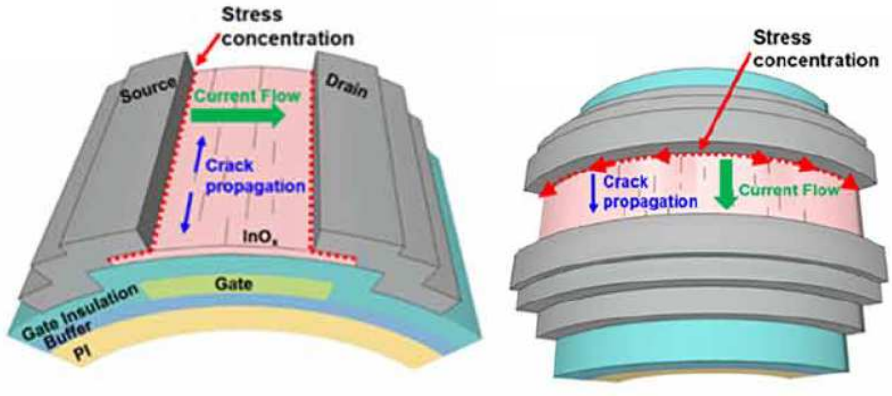

Figure 4.19 Effect electrodes configuration in the current flow and cracks propagation [12].

In our case, for the structure in Figure 4.20 (b) where the strain and current are parallel to each other , the propagation of cracks perpendicular to the current increases the current path length and, as result of this, the resistance increases. However, this is not the case in Figure 4.20 (a), due to the fact that the current path is parallel to the direction of the cracks.

Moreover, by observing Figure 4.21, there is a significant difference in the electrical characteristics when the applied strain and current flow are perpendicular or parallel to each other. In Figure 4.21 (a), the deformation is almost not appreciated due to the variation produced in the width (W) of the resistance. However, when the current-strains are parallel between them, the deformation is applied over the length (L). Figure 4.21 (b) shows that the values obtained are linear and the sensitivity is higher.

In this section, we don't want to analyse the amplitude of the peak, because our goal here is to compare the linearity and the uniformity of the peaks, on Figure 4.21 both graphics have been normalized.

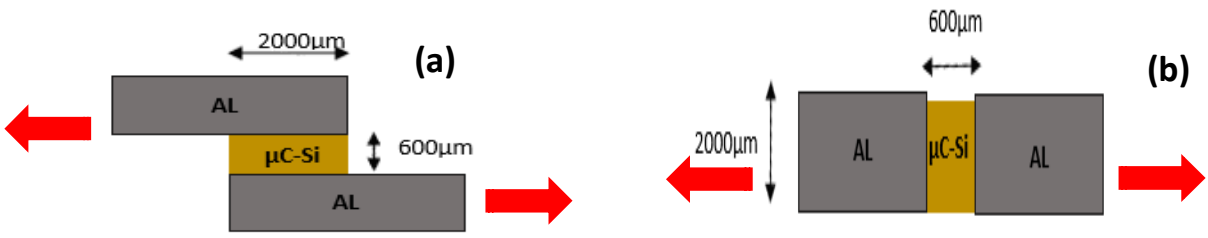

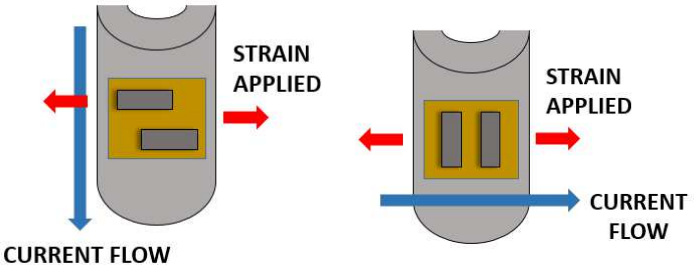

Figure 4.20 Electrodes configuration: (a) The strain applied is perpendicular to the current flow; (b) The strain applied is parallel to the current flow.

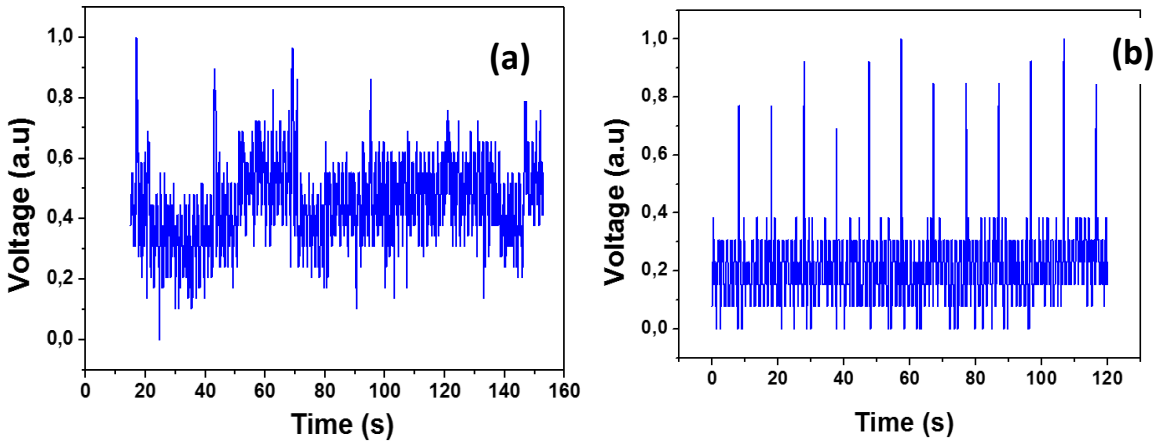

Figure 4.21 Normalized results obtained with electrodes configuration of Figure 4.20. (a) The strain applied is perpendicular to the current flow; (b) The strain applied is parallel to the current flow.

In addition, it was decided to analyze the structure of Figure 4.22 where the current flow has two different directions, first parallels to the strain and later perpendicular to it. However, using this structure, it is impossible to have a distinguishable signal. The length is defined as the distance between the electrodes, however observing this structure, this is difficult to determine it. Hence, between the three design electrodes configurations, the most appropriated corresponds to the design where the strain is parallel to the current flow, Figure 4.21(b).

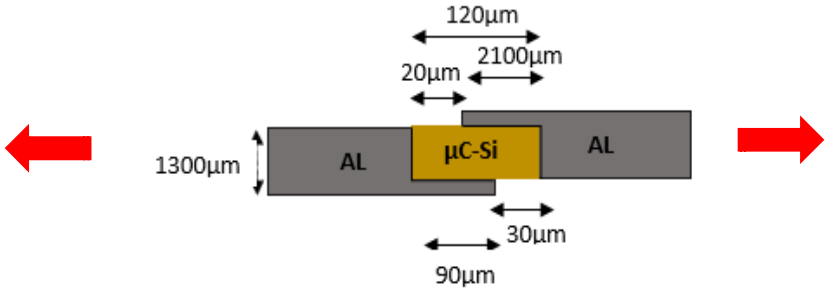

Figure 4.22 Structure design with electrodes configurations for current flow perpendicular and parallel to the strain.

6.2 Geometry selection and dimensions

One time that the design of the electrodes configuration is selected, three different geometries are studied, namely an inter-finger structure (Figure 4.23), a configuration of ten resistances in parallel (Figure 4.24) and a normal shape resistance (figure 4.25).

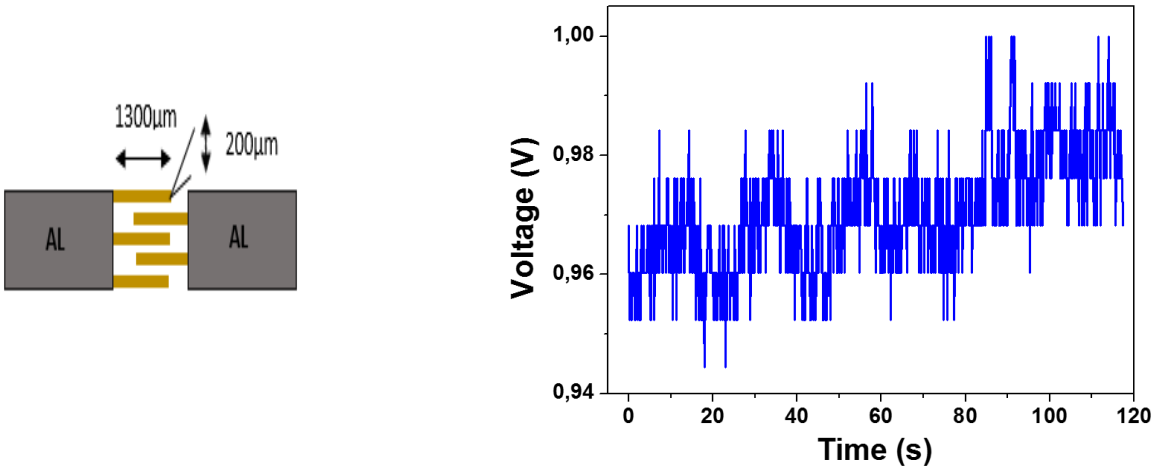

Figure 4.23 Inter-finger structure and the wave obtained after applied signal of Figure 4.18.

For inter-finger structure as shown in Figure 4.23, the deformation applied it is not appreciated. For this reason, this structure has been directly discarded.

The next structural study is Figure 4.24 formed by ten resistances in parallel. For this shape design, we have different dimensions as shown in Table 4.2. However, due to the large length (L) and short width (W) during the characterization, a lot of cracks appeared that completely destroyed the gauge sensor. The only structure that works is for the dimensions L= 1000 µm and W=100 µm, which corresponds to the smallest.

As shown in Figure 4.24, the voltage changes strongly during the characterization. This is due to the fact that the value of the resistance is formed by the equivalence of the ten resistances. The low value of the width (W) compared to the length (L) increases the resistance sensitivity but makes it too fragile during measurements. Moreover, as shown in Figure 4.15 for commercial gauge sensors, the length is concentrated on a small area to help the mechanical flexibility of the global structure in response to deformation.

As a consequence of the fragility of this structure, some of these resistances are broken in the middle of the measurement, so that the voltage variation changes abruptly. Moreover, its

response shows a drift that hinders the post-filtered signal treatment. This drift can be due to the drastic degradation of the structure, a consequence of the design.

Hence, due to the low percentage of resistances that work, the short life-time and the reliability, this structure is discarded for our goal.

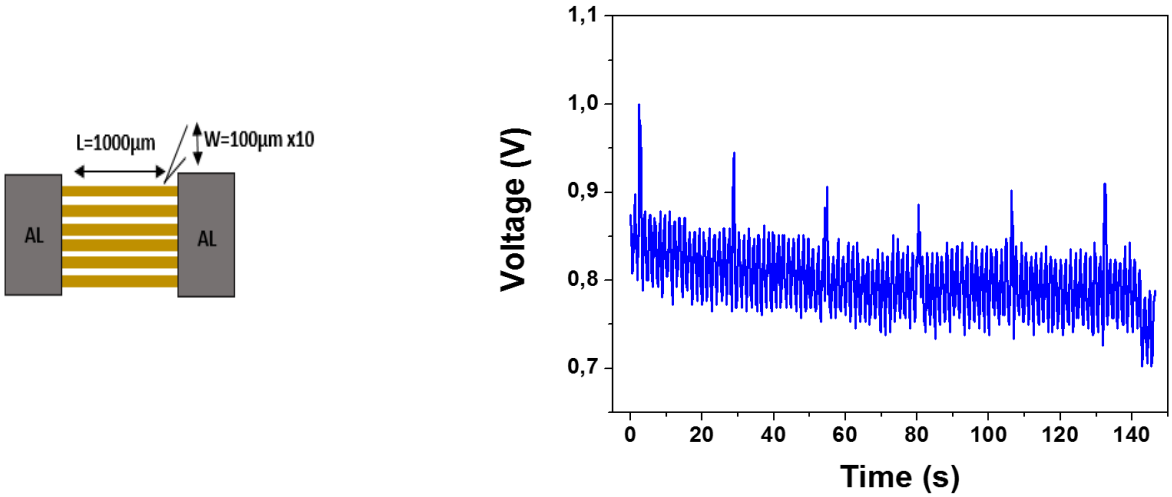

Figure 4.24 Structure of ten resistances in parallel and the wave obtained after applied signal of Figure 4.18.

The last structure study is presented below in figure 4.25 and is analysed according to different dimensions. For a strain gauge, the level of sensitivity is generally related to the grid geometry and in particular to its length/width ratio, as shown in Figure 4.15. In our case, it was decided to study three different cases:

a) Ratio L/W = 1; with L= 1000 µm and W=1000 µm

Figure 4.25 shows this structure next to the graphic obtained. The wave applied for its characterization is shown in Figure 4.18, so if it is compared with the graphic obtained, it can be observed that the structure is not able to react to all the stimulus applied. Moreover, the amplitude of the peaks for the voltage variation is not the same. The average of this value corresponds to $\Delta V = 0.15$ V.

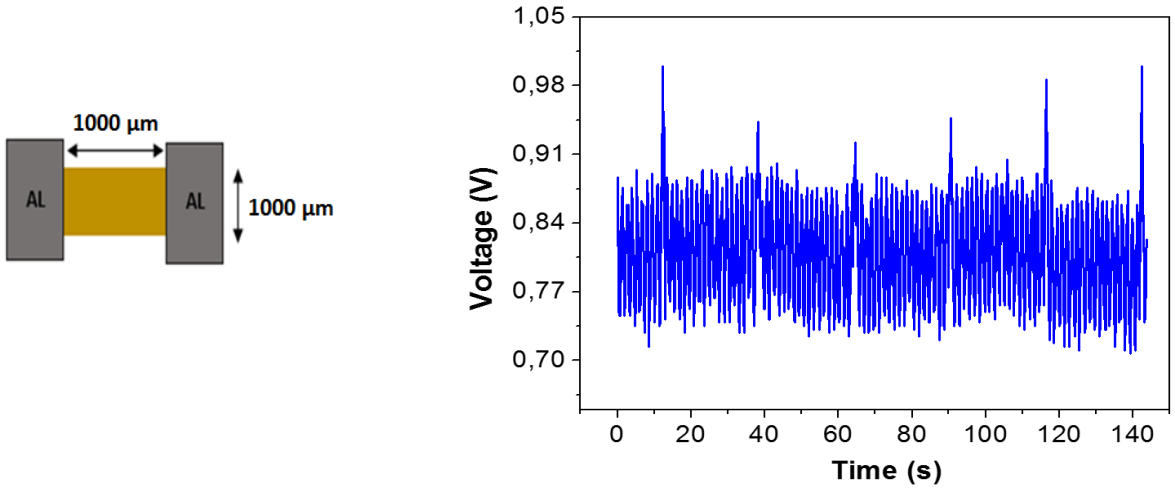

Figure 4.25. Study of rectangle shape when length (L) and width (W) have the same value and it is applied the signal of Figure 4.18.

a) Ratio L >>W : with L=1500 µm W=1200 µm

For this case where the length (L) is bigger than the width (W), the structures for L=4000 µm W=1000 µm and L=7000 µm W=1200 µm were also analysed. However, as it occurred with these length dimensions for the structure of Figure 4.24, almost all the structures were broken during the characterization, and automatically discarded. Figure 4.26, shows the results obtained for the structure with L=1500 µm W=1200 µm. However, the ratio between length and width is practically the same as for the previous structure where L/W=1.

Hence, for big values of length (L) with small values of width (W) due to our design, the fragility of the sensors has increased and it is complicated to obtain a lot of sensors that work.

However, by comparing the results obtained in the graph of Figure 4.25 with Figure 4.26, where both dimensions are similar, the voltage variation and therefore the sensitivity is lower for bigger length (L). The average of voltage variations around $\Delta V = 0.07$ V. For these dimensions, the structure also continues not to be able to react to all the stimulus applied.

As it was commented previous, this can be due to the fact that the global structure needs more time to react, for that reason, commercial sensor designs are with a large length (L) but in a small grid area, as shown in Figure 4.15.

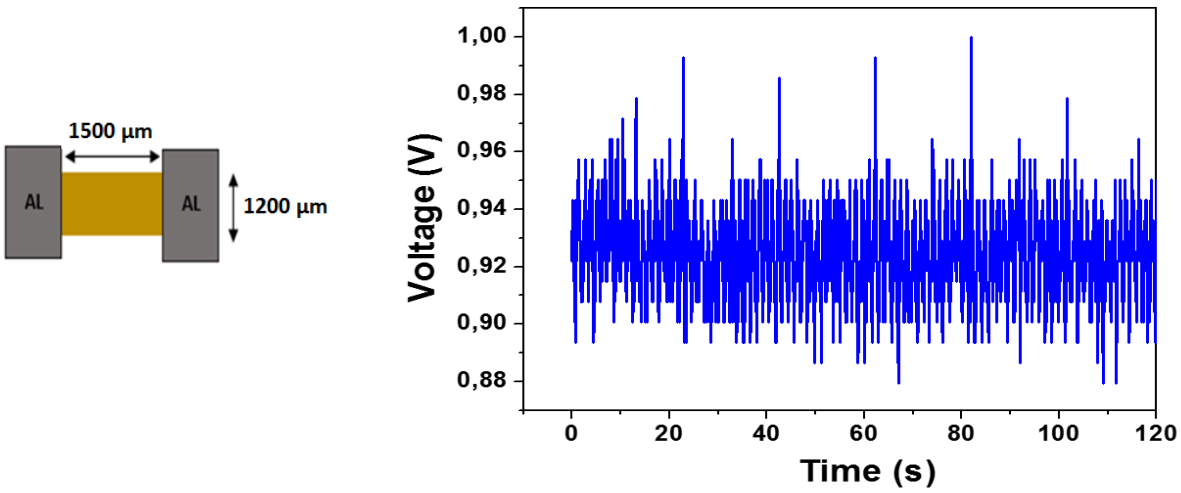

Figure 4.26. Study of rectangle shape when length (L) is bigger than the width (W) and it is applied the signal of Figure 4.18.

a) Ratio L << W with L=600 µm W=2000 µm

To finalize our study, it was decided to investigate the effect when the length (L) is smaller than the width (W), as shown in the graphic obtained in Figure 4.27. The sensor is able to react to all the applied stimuli, moreover all the peaks present similar amplitude values. This can be due to the fact that the low dimensions of the width help the intrinsic structure of the material to be able to come back easily to the initial state. Thus the structure reacted fast to all the applied stimuli even when the frequency had been increased.

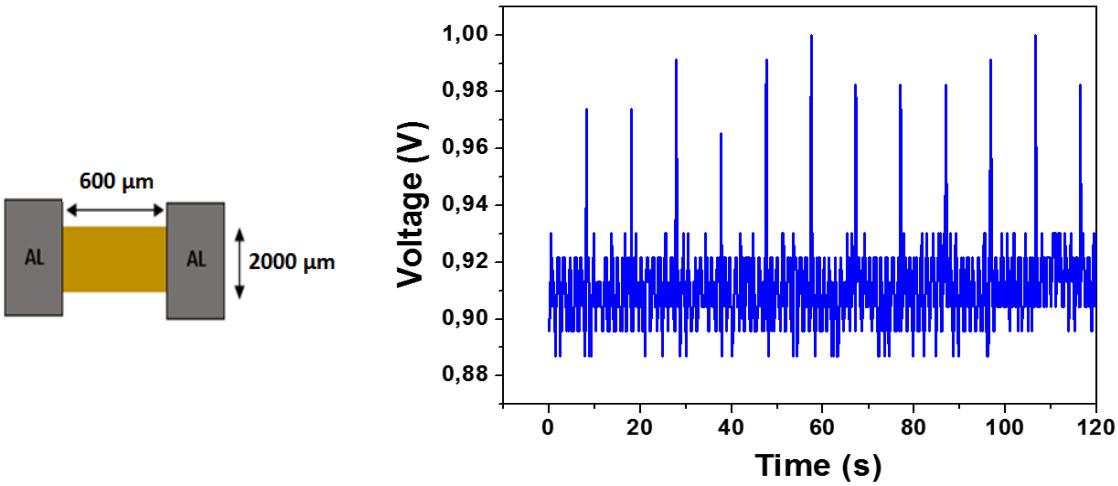

Figure 4.27: Study of rectangle shape when length (L) is lower than the width (W) and it is applied the signal of Figure 4.18

Due to the good sensitivity of this sensor and its ability to follow perfectly the shape of the signal of Figure 4.18, it was decided to verify if it also presents this ability to do it with more complex signals such as ECG signal in Figure 4.28. This wave presents a lot of small and tiny variations such as Q or S peaks. The frequency has been reduced to 0.025 Hz, Figure 4.29. , Due to the resolution of the acquisition system, 10 bits, moreover this frequency allows us to see in detail if the device is able to follow exactly the shape of the applied signal, even for the small peaks variations. Afterwards, the frequency was increased until 0.2 Hz to see how fast the structures are able to react, Figure 4.30.

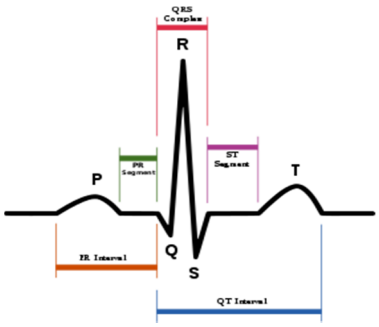

Figure 4.28: ECG waves.

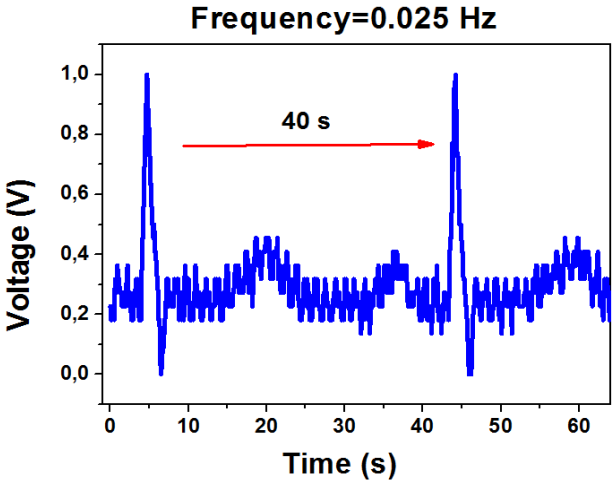

Figure 4.29: ECG waves obtained with structure of Figure 4.27with frequency = 0.025Hz.

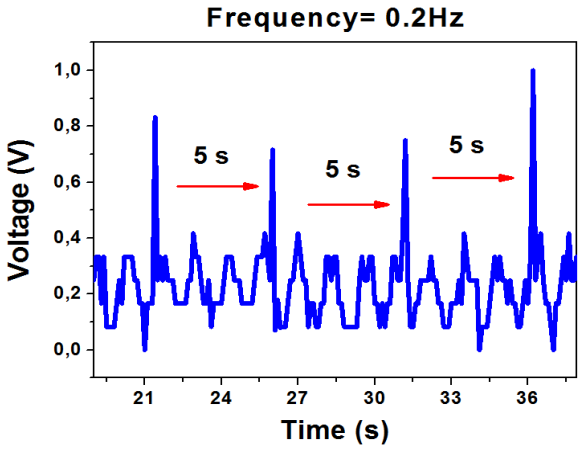

Figure 4.30: ECG waves obtained with structure of Figure 4.27 with frequency = 0.2Hz.

Hence, the structure of Figure 4.27 is able to react quickly, linearly and moreover also presents a good reliability, less drift and the data are more reproducible. For that reason, these dimensions can be a good option for the next mask design.

7. Design dedicated to detect weak dynamic signal

After studying the electrodes configuration, resistance shape, and dimensions that give good performance, it was decided to design a new mask more appropriated to detect weak, continuous and fast measurements. The design is shown on Figure 4.31. It is formed by a matrix of 5x5 resistances, 5 resistances in a straight line, moreover to investigate new resistance shapes such as rosette, serpentine or 5 resistances in parallel ??. This mask also presents a design of thin-film transistors (TFT) because this allows for better sensitivity due to the field effect.

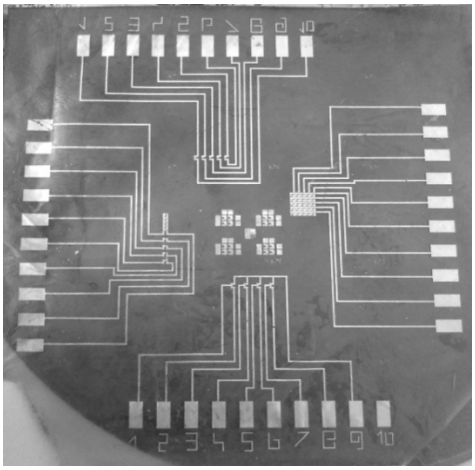

Figure 4.31: Last mask design with different structures and shapes.

With this mask, the study is focused on the behaviour of the sensors in front of different tests. The sensor composed of the straight line of 5 resistances is first submitted to different tests such as sensitivity during continuous loading - offloading cycles.

Due to the relative rigidity of microcrystalline silicon, it suffers from cyclic instability, during which buckling, cracking and even stripping often appear after numerous cycles. Also to verify cyclic stability, the sensor was submitted to periodic endurance loading-offloading cycles. To do that, three different tests have been performed.

The first one is shown in Figure 4.32 where it is performed a long-duration fatigue test with 2160-impulse cycles. On this graphic, it can be observed that the sensors only present a 10% degradation of the relative variation voltage after 3 hours of fatigue. This shift in the voltage value can be due to the cracks in the structure, next to the graphic appears the applied signal.

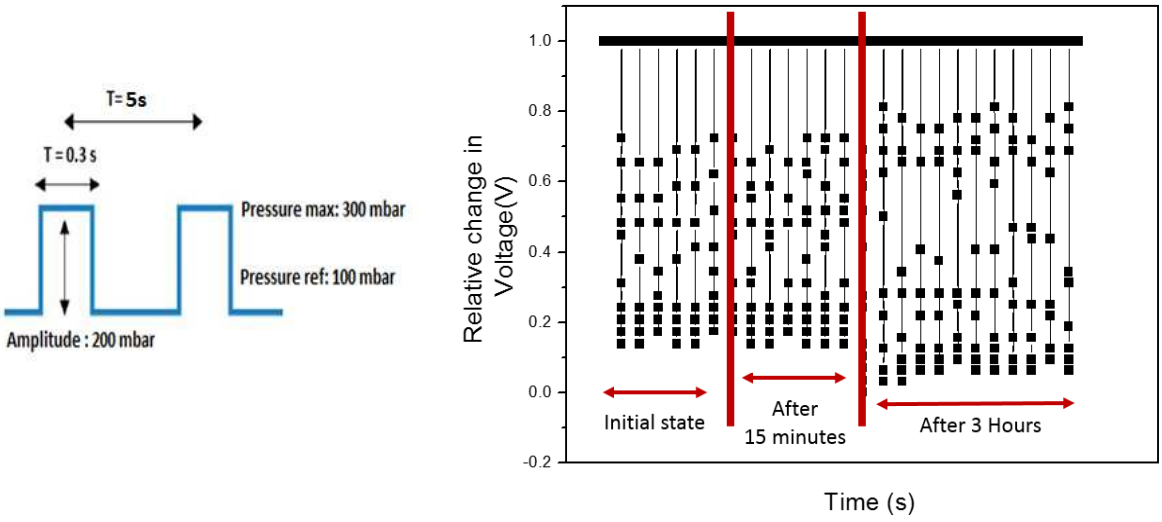

Figure 4.32. Pulse frequency of 0.2Hz and pressure inject of 200mbar. Graphic obtained during fatigue test after 2160 impulse cycle.

After that, the second test was realized on the same sensors that were used during 3 hours in the previous test. The sensors are submitted to a different fixed pressure for 10min. The goal of this test is to observe if, after submitting the structure to a fixed strain deformation during a long time, the structure presents a memory shape to this deformation, i.e. a shift on its value when it comes back to the initial value. Figure 4.33 shows this test, the initial pressure applied starts at 100 mbar and increases to 700mbar, after that the cycle is repeated. In this test the pressure was incremented from 100 mbar to 700 mbar with intervals of 200 mbar. For the first loading cycle, the relative variation of the voltage is more or less the same, around 0.15 V. However for the second cycle, this voltage variation does not follow a pattern. Moreover, when the pressure applied to the resistances changes from 700mbar to 100mbar, there is a shift in the voltage value that can be due to the cracks in the structure caused by the high pressure/deformation applied.

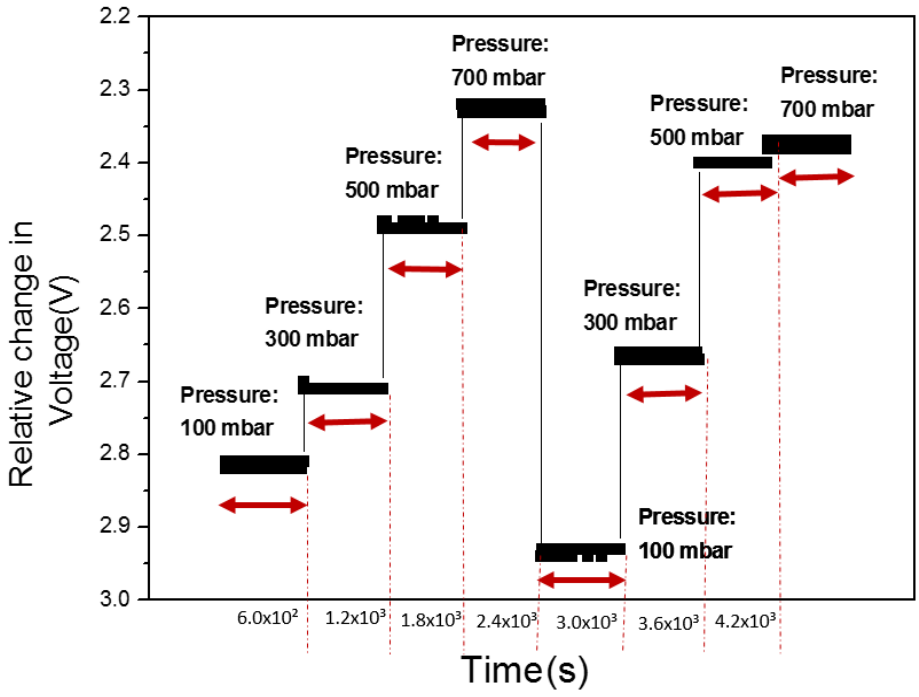

Figure 4.33. Behavior in front of different fix pressure applied during 10min

Finally, Figure 4.34 shows the same test as before, but here the pressure is injected with pulse waves of 0,2Hz during 120 cycles, for each pressure the signal applied in the same as in Figure 4.32. Here, the sensors react with approximately the same variation of voltage during the first and the second loading - offloading cycles. Therefore, µc-Si has better performance under continuous dynamic deformations with variable pressure than under a fixed pressure.

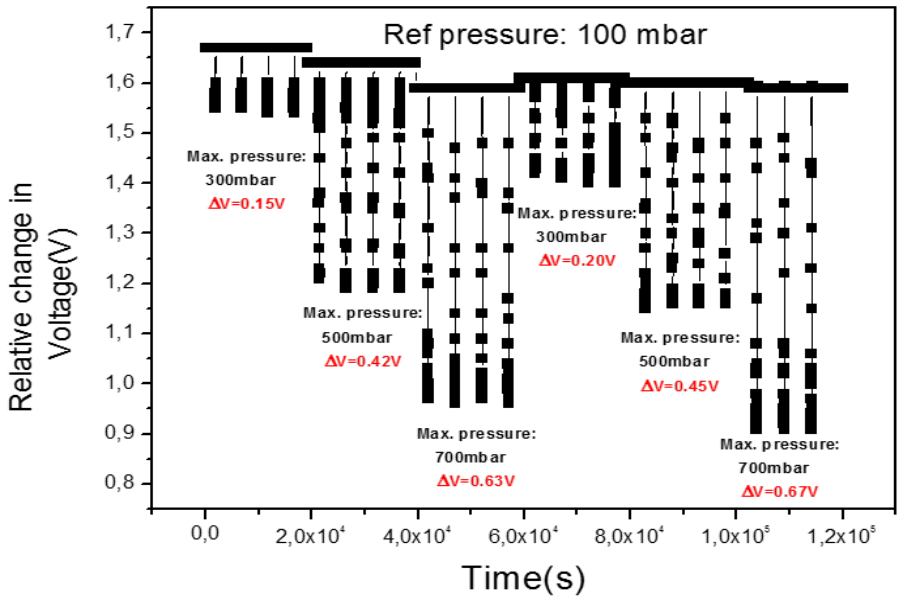

Figure 4.34. Fatigue test of pulse waves of 0,2Hz of frequency during 120 cycle for variable pressure.

8. Conclusion

Throughout this chapter, we describe the steps followed to create our own home-made acquisition system to perform dynamic measurements. Different structures and designs have been studied to try to find which one can be more appropriate to our objective.

During this study, it was concluded that not only the flexibility of the materials affects the accuracy and operation of the sensors; the use of an appropriate design can increase the sensitivity and linearity of them.

The electrodes position when the deformation is applied determines the direction of the current flow. During our study, it was observed that when the deformation is parallel to the current flow, the values obtained are more precise and there is no significant deviation.

In addition, different designs of structures with different dimensions were studied and it was concluded that between all of them, the rectangular design is the most robust. Moreover, for this structure, a comparison between different ratio dimensions of the length and the width was performed. It was concluded that a small width will help the global structure to return easily to its value initial. Based on all this, a new design was created with different structures that were subjected to different fatigue tests.

9. References

[1] Datasheet ‘OB1 - 4 channels microfluidic flow controller’, *Elveflow*.

[2] Architecture of Arduino development board. http://www.arduino.cc/

[3] ‘Know all about Analog to Digital ADC Converters’. [Online]. Available: https://www.elprocus.com/analog-to-digital-adc-converter/.

[4] ‘MyoWare™ | Harness the power of your muscle signals!’, *Kickstarter*. [Online]. Available: https://www.kickstarter.com/projects/312488939/myowaretm-harness-the-power-of-your-muscle-signals.

[5] Datasheet ADS126x32-Bit, Precision,38-kSPS, Analog-to-DigitalConverter (ADC) with Programmable Gain Amplifier (PGA) and Voltage Reference

[6] ‘Resistance and Resistivity | Physics’. Available: https://courses.lumenlearning.com/physics/chapter/20-3-resistance-and-resistivity/.

[7] K. Lloyd, ‘Strain Gauge Measurement using Signal Generator | Strain Gauge Sensitivity’, *MTI Instruments*.

[8] Y. Chan, M. Skreta, H. McPhee, S. Saha, R. Deus, and L. Soleymani, ‘Solution-processed wrinkled electrodes enable the development of stretchable electrochemical biosensors’, *Analyst*, vol. 144, no. 1, pp. 172–179, Dec. 2018.

[9] N. Liu, A. Chortos, T. Lei, L. Jin, T.R. Kim, W-G. Bae, C. Zhu, S. Wang, R. Pfattner, X. Chen, R. Sinclair, Z. Bao ‘Ultratransparent and stretchable graphene electrodes’, *Sci. Adv.*, vol. 3, no. 9, p. e1700159, Sep. 2017.

[10] J. Lee, S. Kim, J. Lee, D. Yang, B. C. Park, S. Ryu, I. Park, ‘A stretchable strain sensor based on a metal nanoparticle thin film for human motion detection’, *Nanoscale*, vol. 6, no. 20, pp. 11932–11939, Sep. 2014.

[11] Autors ??‘Review of recent advances in flexible oxide semiconductor thin-film transistors: Journal of Information Display: Vol 18, No 4’. [Online]. Available: https://www.tandfonline.com/doi/full/10.1080/15980316.2017.1385544. [Accessed: 30-Sep-2019]. pp? Year ??

[12] J. Sheng, J. Park, D-W. Choi, J. Lim, and J.-S. Park, ‘A Study on the Electrical Properties of Atomic Layer Deposition Grown InOx on Flexible Substrates with Respect to N_2O Plasma Treatment and the Associated Thin-Film Transistor Behavior under Repetitive Mechanical Stress’, *ACS Appl. Mater. Interfaces*, vol. 8, no. 45, pp. 31136–31143, Nov. 2016.

General conclusion and perspective

The objective of this thesis is to investigate the piezoresistivity properties of µc-Si to develop a sensor able to react to continuous and dynamic deformations with good linearity, fast and with reproducible results.

To do that, the sensors are fabricated on 25µm of Kapton substrate. This material is biocompatible and it can withstand chemical solutions. This makes it one of the most frequently used substrates for standard micro-manufacturing process. Although it can support high-temperature conditions, until 400 °C, the maximum temperature chosen during this fabrication process was an annealing at 180 °C, making the process compatible with other kinds of plastic substrates.

As semiconductor material, µc-Si, deposited by two different techniques PECVD and ICP-CVD, is selected. The motivation to use this material is its compatibility to flexible substrate, and even if it has been widely investigated at the IETR as pressure sensor, it has never been used for dynamic measurements.

The thesis is mainly divided in two parts, the first one where we investigate the piezoresistive properties of µc-Si through its characterization by static deformations using TLM structure and the second part where we study the reaction of this material in front of dynamic deformations.

µc-Si deposited by PECVD has previously been investigated during K. Kandoussi's thesis and the deposition parameters have been optimized. For this reason, , the study focuses more on the mechanical behaviour of the structure in front of static deformations and the piezoresistive performance of this material.

The goal is to obtain sensors thinner as possible, to have better flexibility and good mechanical behaviour in dynamic deformations. However, the decrease in the thickness of the substrate causes a lot of stress problems. To solve that, three different structures were investigated with a thickness of the compound structure that was gradually reduced. It was observed that when the global structure is reduced, the resistivity uniformity of µc-Si gets worse and the standard deviation higher. The values obtained for the GF (gauge factor) when they are submitted to static deformations are the same for the three proposed structures. The thickness reduction will improve the flexibility of the structure film/substrate when it will be subjected to dynamic measurement.

On the other hand, due to the arrived of the ICP-CVD machine to IETR laboratory, it has been interesting to determine the optimal parameters for the deposition of µc-Si by using this method.

As in the previous study for the samples deposited by PECVD, the piezoresistive properties of µc-Si were not affected by the structure thickness. All the devices, developed with ICP-CVD, where therefore fabricated using the lower thickness structure.

For the study of µc-Si using this method, different deposition conditions were proposed to see if some variations in the piezoresistive properties occur when some parameters are changed, such as the pulses addition to the plasma, the quantity of doping gas in the plasma or the type of doping gas used, AsH_3 or PH_3. The study of the different conditions concluded that:

- The application of pulses in the plasma decreases the specific contact resistance value and increases the crystalline fraction of the material.
- When AsH_3 is used as doping gas, the increase of the sensitivity (GF) is observed in the cases where pulses are applied to the plasma. By adding pulses, the energy plasma increases, helping the diffusion of the molecules.
- However for PH_3 as doping gas, as it presents a low diffusion coefficient, its diffusion is really fast and it is not necessary to add the pulses in the plasma. In this case, the increment the sensitivity (GF) is observed when the quantity of the doping gas flow is varied from 20 to 10 sccm. Hence, to see some increments in GF using only this doping agent, it is necessary to reduce the amount of flow rate injected during the deposition process.

To study piezoresistive properties, structures with different dimensions were first studied. This allowed us to conclude that square resistances are the most robust because they can be submitted to longer fatigue tests. Once the design was chosen, dimensions where studied to extract the most appropriate one for the sensors. In our case, the resistance dimensions with smaller length than width present more linearity, accuracy, and precision. For that reason, this was taken into account when designing the second mask. The devices obtained with this mask, have been submitted to different loading-unloading fatigue tests and some physiological measurements have been simulated to see if our sensors can be used in the human body.

As a perspective for future work on the topic of this thesis, can be several points such as:

- In the second mask, some thin-film transistors (TFT) structures wer designed, however during the fabrication process, their leakage current was very high, making impossible to characterize them. Due to the field-effect, it could present a higher sensitivity than the resistance, for that reason it will be interesting to test them under dynamic measurement.
- Moreover, another point that should be important to improve is the matrix characterization. Because of the limitations of our acquisition system, we could not submit this structure to more rigorous characterization tests.